OPEn HPC theRmomechanical tools
for the development of eAtf fuels

OperaHPC: D4.2 - Review and selection of state-of-the-art models for advanced fuel performance analysis

Version 1 – 28/02/2025

Funded by the European Union

Disclaimer

Document type	Deliverable
Document number	D4.2 version 1
Document title	Review and selection of state-of-the-art models for advanced fuel performance analysis
Authors	Giovanni Zullo, Davide Pizzocri, Lelio Luzzi (POLIMI), Alessandro Scolaro (EPFL), Lokesh Verma, Ivor Clifford (PSI)
Release date	28/02/2025
Contributing partners	POLIMI, EPFL, PSI
Dissemination level	Public

Version	Short description	Main author	PMO	WP leader	Coordinator
1	First release	G. Zullo (POLIMI) Date 07-01-2025	S. DeGrandis Date 04-02-2025	A. Scolaro (EPFL) Date 03-02-2025	B. Michel (CEA) Date 28-02-2025

Abstract

The deliverable D4.2 encompasses a thorough review and of behavioural models for accurate fuel performance calculations. The activities of the task contributors (POLIMI, EPFL. PSI) are outlined here below:

- **POLIMI** is responsible for review and select fission gas behavioural models in SCIANTIX, an open-source code for fission gas behaviour, which is coupled with OFFBEAT. The focus is on advancing high-burnup structure models, the modelling of chromia-doped fuels and athermal fission gas release.
- **EPFL** reviewed and selected models relevant to the OperaHPC project objectives, addressing key gaps in OFFBEAT's capabilities. In particular, EPFL focused on RIA, implementing anisotropic viscoplasticity and a failure criterion for hydrided cladding; LOCA, introducing large-strain and high-temperature models; and contact modelling, developing an implicit algorithm for pellet-to-pellet and pellet-to-cladding interactions during PCMI. Plans have also been made to develop a 3D gap heat transfer model to assess the impact of traditional 1D heat conductance models in wide-gap conditions such as during cladding ballooning.
- **PSI** undertakes the development of models for cladding oxidation, hydrogen transport, and geometric imperfections. Additionally, PSI conducted a comprehensive review of multidimensional macroscopic fuel behaviour models in international codes such as ALCYONE (CEA), BISON (INL), DIONISIO (CNEA), and Falcon (EPRI). This review identified key models for implementation in OFFBEAT to enhance its predictive capabilities for fuel performance analysis.

Table of Contents

List of Acronyms

EPMA: electron probe micro-analysis

FNN: feed-forward neural network

FPC: fuel performance code

FG: fission gas

FGB: fission gas behaviour

FGR: fission gas release

FP: fission product

HBS: high-burnup structures

HBWR: Halden Boiling Water Reactor

IFA: instrumented fuel assembly

LWR: light water reactor

ML: machine learning

PCI: pellet-cladding interaction

PDE: partial differential equation

PWR: pressurised water reactor

SDA: spectral diffusion algorithm

SMR: small modular reactor

TKD: tetrakaidecahedron

List of Figures

List of Tables

1. Introduction

Accurate fuel performance modelling is essential for ensuring the safety, reliability, and efficiency of nuclear fuel rods under various operating and transient conditions. The need for enhanced predictive capabilities in fuel performance codes (FPCs) led to the continuous development and refinement of behavioural models. This deliverable addresses this necessity by providing a comprehensive review and selection of models relevant to fission gas behavior (FGB), high-burnup structure (HBS) evolution, cladding oxidation, and hydrogen transport.

The work presented in this deliverable includes contributions from POLIMI, EPFL, and PSI. POLIMI focused on refining and implementing (FGB) models in SCIANTIX, an open-source meso-scale code coupled with OFFBEAT, with a particular emphasis on HBS formation, chromia-doped fuel modelling, and athermal fission gas release (FGR). EPFL reviewed and selected models aligning with OperaHPC objectives, addressing limitations in OFFBEAT current capabilities. The research emphasized RIA (Reactivity-Initiated Accident) scenarios, introducing anisotropic viscoplasticity and failure criteria for hydrided cladding, as well as LOCA (Loss-of-Coolant Accident) conditions, incorporating high-temperature and large-strain models. Additionally, EPFL advanced 3D methodologies for gap heat transfer modelling. PSI contributed by developing models for cladding oxidation, hydrogen behaviour, and geometric imperfections, as well as conducting a review of multidimensional macroscopic fuel behavior models in international codes such as ALCYONE, BISON, DIONISIO, and Falcon.

This document is structured as follows:

- **Section 2** details the selection and implementation of advanced models in SCIANTIX, focusing on high-burnup structure evolution, chromia-doped fuel modelling, and athermal fission gas release.
- **Section 3** presents the review of physical models for OFFBEAT, including those for LOCA, RIA, contact modelling, and 3D gap conductance methodologies.
- **Section 4** outlines the models developed for cladding oxidation, hydrogen transport, and hydride behavior in OFFBEAT.
- **Section 5** provides concluding remarks summarizing the advancements achieved in this deliverable.
- **Appendix A** offers a review of state-of-the-art multidimensional fuel behaviour modelling, discussing the capabilities and possible extensions of international codes such as BISON, ALCYONE, DIONISIO, Falcon, and OFFBEAT.

2. Selection and development of advanced models in SCIANTIX

Within Task 4.2, POLIMI reviewed behavioural models to be developed and implemented in SCIANTIX. The focus was on models for fission gas behaviour in high-burnup structures (HBS), chromia-doped UO_2 fuel, and the effect of the open porosity of fuel pellets on athermal fission gas release.

2.1 Modelling HBS formation, transition and xenon depletion

Properly modelling the formation and evolution of the HBS is critical for a reliable modelling of the fuel rod fuel performance. HBS affects material properties (e.g., thermal conductivity, elastic modulus) and fission gas behaviour (FGB). In addition, HBS represents a potential concern for the safe operation of nuclear fuel to extended burnups. For instance, microstructure evolution and fission gases accumulation at burnup values above 60 MWd/kgU can increase the risk of fine fuel fragmentation phenomenon, which has to meet safety criteria during design-basis accidents, such as reactivity-initiated accidents and loss-of-coolant accidents [1], [2], [3], [4], [5], [6], [7], [8], [9].

POLIMI, in collaboration with EPFL and CEA, targeted a novel modelling approach for the fission gas (FG) depletion problem, this being the fundamental starting point to provide a solid representation of the distribution of fission gas that accumulates inside inter-granular cavities and HBS porosity, and the smooth phase transition from the non-restructured UO_2 matrix to the restructured one. Both semi-empirical [10], [11], [12] and mechanistic models [7] are available in the literature, representing the fission gas depletion of HBS in UO_2. A mechanistic approach was provided in the work of [7], in which the authors started from the description of the restructured volume fraction and then solved two intra-granular problems, one for each phase, considering two different integration domains, characterised by their grain size (e.g., micrometric in the as-fabricated region and sub-micrometric in the restructured region). The two intra-granular problems were solved simultaneously with an HBS sweeping condition, given by the conservation of the total concentration of gas in the considered control volume.

As a model improvement, it is here proposed a more natural description of the intra-granular gas evolution in uranium dioxide during the restructuring process. Firstly, we derived a sweeping term that is responsible of the mass exchange from the non-restructured to the restructured HBS matrix. The sweeping term can be included in the intra-granular gas diffusion equations, avoiding additional constraints. Secondly, by leveraging the spectral diffusion algorithm for the intra-granular fission gas problem, we avoid dealing with two different integration domains (a micrometric one and a sub-micrometric one) and solve a single spatial dimensionless problem (i.e., considering the same eigenfunctions), this being more effective from a numerical point of view. The model developed is implemented in SCIANTIX, a 0D meso-scale code for physics-based modelling of fission gases in nuclear oxide fuel and the calculations are compared with both experimental data [13] and semi-empirical models.

2.1.1 Model

The model derivation starts from the definition of the restructured volume fraction α that describes the HBS formation rate in uranium dioxide. Hence, a unidirectional phase change from a non-restructured phase (N) to a restructured one (R) is considered, with the corresponding evolution of the two fission gas concentrations C_N and C_R. The full derivation is described in the relative publication, disseminated in the OperaHPC project [14]. Here, only the main results are reported.

From the definition of the restructured volume fraction as the ratio of the restructured fuel volume (i.e., developed HBS) over the considered fuel volume ($\alpha = V_R/V$), the total concentration of fission gas atoms C_T (both in restructured and non-restructured regions) is given by the weighted sum:

$$C_T = \alpha C_R + (1-\alpha)C_N \tag{1}$$

It is more convenient to introduce the following quantities:

- $C_1 = (1-\alpha)C_N$, concentration of gas atoms in the non-restructured region over the total volume V.
- $C_2 = \alpha C_R$, concentration of gas atoms in the restructured region, over the total volume V.

Because both concentrations are referred to the same volume. From the mass conservation principle, it is possible to write two partial differential equations (PDEs) describing the behaviour of the fission gas concentrations C_1 and C_2:

$$\frac{\partial C_1}{\partial t} = D_N \nabla^2 C_1 - \frac{1}{1-\alpha}\frac{\partial \alpha}{\partial t} C_1 + (1-\alpha)S \tag{2}$$

$$\frac{\partial C_2}{\partial t} = D_R \nabla^2 C_2 + \frac{1}{1-\alpha}\frac{\partial \alpha}{\partial t} C_1 + \alpha S \tag{3}$$

Where $S = yF$ is the source term of fission gases is the fuel grain, y being the cumulative fission yield and F the fission rate density. In particular, Eq. (2) describes the production and diffusion mechanisms (with a diffusivity D_N) of gas atoms in the non-restructured (i.e., as-fabricated) fuel grains. Eq. (3) describes the production and diffusion mechanisms (with a diffusivity D_R) of gas atoms within the restructured (i.e., sub-micrometric, HBS) fuel grains. The additional term $\pm\frac{1}{1-\alpha}\frac{\partial \alpha}{\partial t}C_1$ has been analytically derived in and represents the transfer of gas atoms from the non-restructured fuel grains to the restructured one during the restructuring process, determined by the increase of the restructured volume fraction α.

2.1.2 Implementation and assessment in SCIANTIX

Eqs. (2) and (3) have been used in the SCIANTIX code [15] to obtain a complete description of the transition from the as-fabricated fuel to the HBS fuel region. In line with the state-of-the-art representation of fission gas behaviour (FGB) [6] [7] [16] the working hypotheses are the followings:

- The fuel grains are modelled as spherical domains.
- In line with the new SCIANTIX (version 2.0) code structure, two phases of the UO_2 fuel are considered: the non-restructured (UO_2) and restructured UO_2 (i.e., UO2-HBS). Each phase features its physical properties, e.g., different grain sizes.
- Each UO_2 phase forms a dedicated system (e.g., Xe-in-UO_2 and Xe-in-UO_2-HBS), each one with its specific properties (e.g., the diffusivity of xenon in the fuel matrix).

Conventional symmetric boundary conditions at the centre of the spherical domain and perfect sink boundary conditions at the border of the spherical domain are applied. On top of the standard fission gas behaviour description operated by SCIANTIX (e.g., the evolution of the intra-granular bubble population), we consider the following diffusion problem:

$$\frac{\partial C_1}{\partial t} = \frac{D_1}{a_1^2}\nabla^2 C_1 - gC_1 + bm_1 - \frac{1}{1-\alpha}\frac{\partial \alpha}{\partial t}C_1 + (1-\alpha)S \tag{4}$$

$$\frac{\partial m_1}{\partial t} = gC_1 - bm_1 - \frac{1}{1-\alpha}\frac{\partial \alpha}{\partial t}m_1 \tag{5}$$

$$\frac{\partial C_2}{\partial t} = \frac{D_2}{a_2^2}\nabla^2 C_2 + \frac{1}{1-\alpha}\frac{\partial \alpha}{\partial t}(C_1 + m_1) + \alpha S \tag{6}$$

With $a_1 = 5\ \mu\mathrm{m}$ and $a_2 = 150\ \mathrm{nm}$ representative values of the radii of the fuel grains in non-restructured UO_2 and in restructured UO_2, respectively. The diffusivity D_1 of the fission gas in non-restructured UO_2 comes from the classical Turnbull formulation [17], also employed as default option in SCIANTIX [15]. The diffusivity D_2 of the fission gas in restructured UO_2 is set as $D_2(\mathrm{m^2 s^{-1}}) = 4.5 \times 10^{-42} F(\mathrm{fiss\ m^{-3} s^{-1}})$, according to the works of Pizzocri et al. [12] and Barani et al. [7]. The intra-granular trapping rate g and irradiation-induced re-solution rate b are given by the standard formulations from Ham [18] and Olander et al. [19], respectively.

The system of equations (4)-(5)-(6) represent the extended intra-granular problem that is solved in SCIANTIX, tailored to represent a smooth transition from UO_2 to UO_2-HBS phase. In particular,

- C_1 represents the concentration of fission gas in dynamic solution within the non-restructured matrix.
- m_1 represents the concentration of fission gas trapped in intra-granular bubbles within the non-restructured matrix.
- C_2 represents the concentration of fission gas in dynamic solution within the restructured matrix.

Since the intra-granular diffusion problems in SCIANTIX are discretised with the spectral diffusion algorithm (SDA), we avoid solving the first two differential equations (Eq. 4-5) on the non-restructured micron-sized fuel grain and the third one (Eq. 6) on the restructured nanometric fuel grain by non-dimensionalising the Laplace operator. In other words, we solve the diffusion problem on the unit-radius sphere without changing the system eigenvalues. The restructured volume fraction proposed by Barani and co-workers (Barani et al., 2020, Barani et al., 2022) is:

$$\alpha = 1 - \exp\left(-2.77 \times 10^{-7} \beta_{eff}^{3.54}\right) \tag{7}$$

The restructured volume fraction α is proportional to the local effective burnup β_{eff} (MWd/kgU), used as a virtual threshold to define the HBS formation at temperature lower than the healing temperature threshold (T_{th}= 1273.15 K):

$$\beta_{eff} = \int H(T_{th}) d\beta \tag{8}$$

where β (MWd/kgU) is the fuel local burnup and H is the Heaviside function. To evaluate the calculations of the model, we applied the previous modelling approach to simulate the behaviour of a representative light water reactor (LWR) fuel pellet rim portion with SCIANTIX. Namely, we considered a steady-state irradiation history up to 200 MWd/kgU at low temperature (723 K) and high fission rate (2 10^{19} fiss/m^3s) Figure 1 and Figure 2 show the results obtained from solving Eqs 4-5-6. To evaluate the impact of the sweeping term, Figure **1** is obtained by neglecting such term while it is considered in Figure 2.

Moreover, Figure **1** and Figure 2 include separate contributions for xenon concentrations retained in UO_2 matrix:

- The contribution from the xenon retained in non-restructured UO_2 grains ($C_1 + m_1$).
- The contribution from the xenon retained in restructured UO_2-HBS grains (C_2) and their sum.

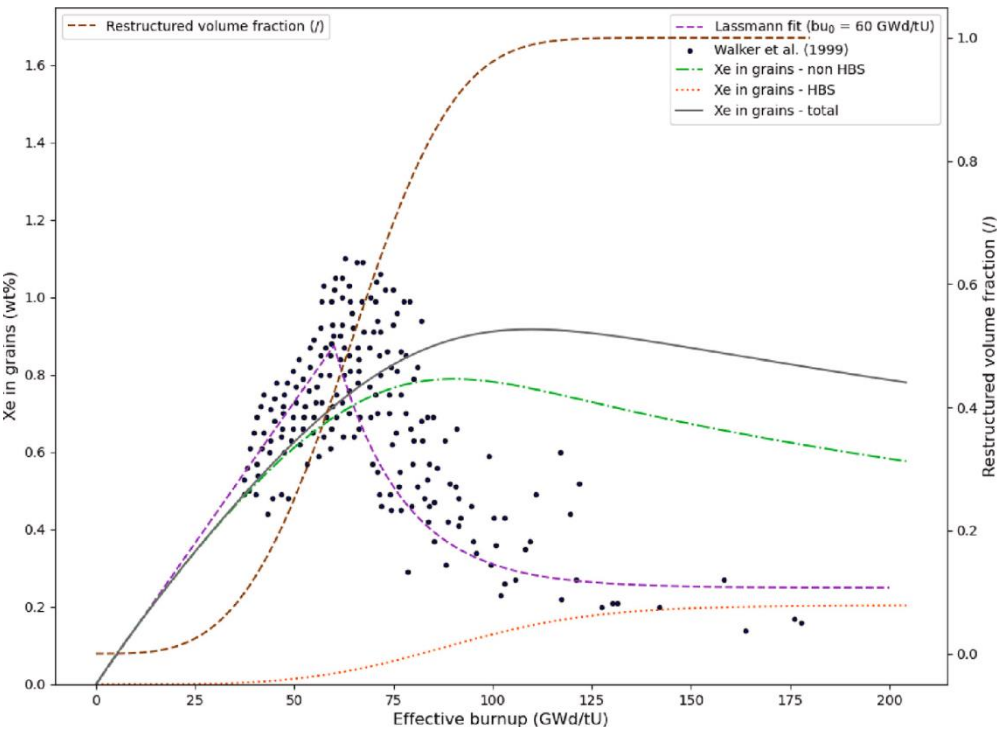

Figure 1: Intra-granular xenon concentration calculated with the present model, without the sweeping term, as a function of local effective burnup. The comparison with the model from **[10]**, is reported (purple dotted line), together with experimental data measured by EPMA on several samples (black dots, from **[13]**.

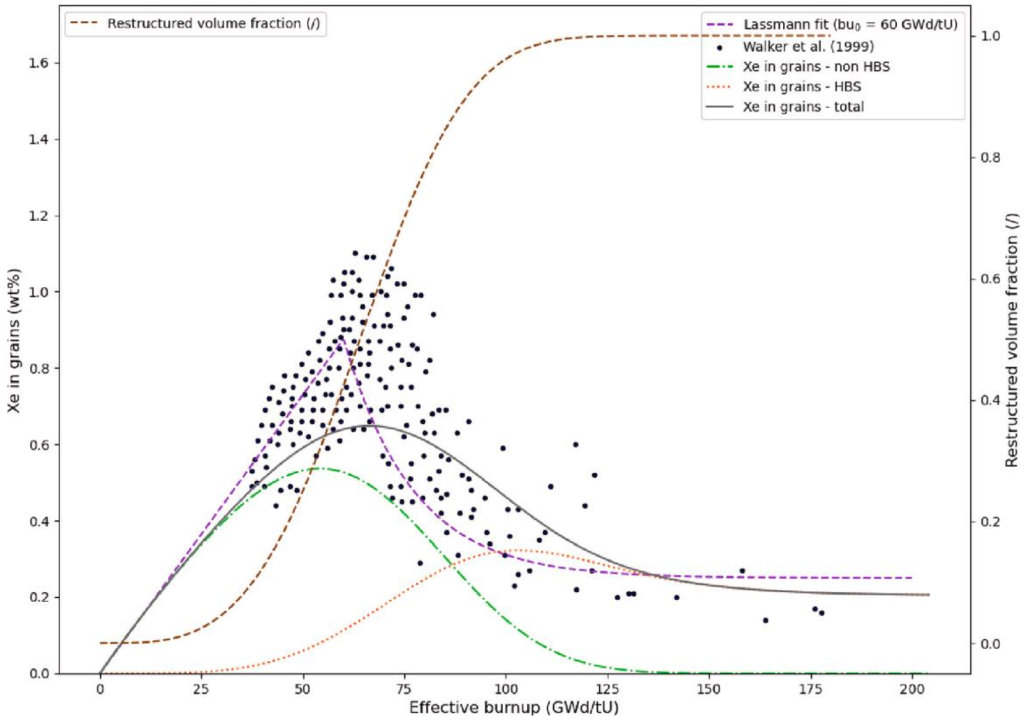

Figure 2: Intra-granular xenon concentration calculated with the present model, including the sweeping term, as a function of local effective burnup. The comparison with the model from Lassmann et al. (1995b), is reported (purple dotted line), together with experimental data measured by EPMA on several samples (black dots, from Walker, 1999).

The purpose of Figure 1 is to clarify the impact of the sweeping term which ensures a more realistic representation of the xenon depletion process together with advantages of numerical and implementation-wise nature. In particular, moving from Figure 1 to Figure 2, it can be noted that the mass transfer between the two matrix phases is responsible for the smooth decrease of the retained gas in reasonable agreement with available measured data. Moreover, the tail of the calculated intra-granular xenon concentration depends on the grain size of the UO2-HBS matrix (i.e., asymptotic gas concentration). We use a value of 150 nm (Table 1), that is in line with experimental observations [9] and previous modelling approaches [8] [10], and that agrees with the experimental data considered in Figure 2. On the other hand, such grain size has its degree of intrinsic uncertainty [7] [8]. The experimental data in Figure **1** and Figure 2 come from different irradiation conditions and initial fuel characteristics. Considering the scattering of the considered data, the agreement can be regarded as acceptable. Some degree of uncertainty must be also taken into consideration, for instance, in the single-atom diffusivities of the xenon in the fuel matrices (reported in Table 1), regarding the experimental characterisation, which in principle could allow us to consider different (but reasonable) initial fuel grain sizes. Most importantly, some uncertainty must be ascribed to the 0-dimensional simulation we are performing with the SCIANTIX code, considering that a constant temperature and constant fission rate are not fully representative of the local temperature and burnup gradients. For instance, uncertainty is brought to the predicted position of the peak of the retained xenon ($\sim$60 MWd/kgU in the considered simulation), which depends on the restructured volume fraction α, and on the local burnup itself. Further refinement of this feature is to be considered in a more detailed representation of the restructured volume fraction, possibly including other quantities like the dislocation density as it was done in other works [4] [20]. Issues of this kind have been addressed and detailed in previous, and a similar examination and comparison are valid for the present work.

In conclusion, this section outlines a modelling approach to describe the intra-granular fission gas behaviour in UO_2, considering the evolution of the non-restructured and restructured fuel matrices. The model leverages the definition of the restructured volume fraction, which currently depends on the local effective burnup. The primary outcome of the model is a simple yet effective description of two intra-granular gas diffusion problems interconnected by an exchange term, sweeping gas atoms from one phase to the other. In addition, by leveraging the spectral diffusion algorithm for the intra-granular fission gas problem, we avoided dealing with two different integration domains (micrometric and sub-micrometric grains) and solved a single spatial dimensionless problem. The model developed has been implemented in SCIANTIX, a 0D meso-scale code for physics-based modelling of fission gases in nuclear oxide fuel and compared with experimental data and semi-empirical models. The model results are consistent with the experimental data and past semi-empirical models, with the sweeping term providing a smooth representation of the xenon depletion in forming HBS.

2.2 Model for chromium solubility and fission gas diffusivity

Accumulation of fission products (FPs), particularly FGs, is among the primary causes limiting the performance of the UO_2 fuels due to deteriorating safety and operational margins at high burnup. A possible solution for controlling the fission gas release (FGR) with burnup consists in modifying the initial fuel microstructure during the manufacturing process by using some additives that promote the crystalline growth of the fuel grains during sintering. Such alteration of the initial fuel microstructure modifies the diffusion phenomena inside the fuel pellets, leading to an increased effective retention of the fission gas. Among the numerous additives considered, chromium oxide appears as one of the most promising, since most of the thermal-mechanical properties of the unirradiated Cr_2O_3-doped fuel are fundamentally the same as the UO_2 fuels, such as thermal diffusivity and melting temperature. Besides the enhanced fission gas retention, the increased average grain size, which was detected up to 7 times greater than the undoped fuel one, i.e. up to 50 µm of grain radius, experimental data confirmed that Cr_2O_3-doped fuel exhibits enhanced pellet-cladding interaction (PCI) resistance, which was attributed to an increased viscoplasticity and the development of favorable crack patterns [21] [22]. During fabrication, chromium oxide is typically added, as a powder, to UO_2 powder in quantities of around ~1000 wt. ppm, which is then sintered at high temperature

(1600–1800°C) under a controlled atmosphere. It is convenient to limit dopant content to the solubility limit to minimize the potential impact on other materials and neutronic fuel properties while maintaining the benefits of large grains. In fact, Chromium is a neutronic absorber, hence it could be combined with Aluminium, during the sintering process, to reduce this effect. In this way, in the final product, chromium can be found mostly in a soluble fraction in the solid solution in UO_2 and, minimally, in an insoluble fraction as separate Cr oxide precipitates.

At POLIMI, we review the chromium solubility model proposed by Riglet-Martial et al. [23], optimizing it to better reproduce available EPMA data [24], together with simple modelling of chromium phase evolution during irradiation based on the work by Curti and Kulik [25]. Then, a new description of the fission gas diffusion coefficient is derived, based on defect concentration induced by doping, consistent with the recent work by Murphy et al. [26]. All models are implemented in SCIANTIX. A separate-effect comparison against experimental data is performed, for all models proposed. An integral assessment is discussed, considering results obtained with the Fuel Performance Code (FPC) TRANSURANUS coupled with SCIANTIX [15].

2.2.1 Solubility and phase evolution models

A solubility model for Chromium in UO_2 was proposed by Riglet-Martial. Due to the lack of experimental information in the literature in some key areas of the Cr-O phase diagram, additional measurements were collected by authors to obtain a full description of the system in the whole range of temperature and oxygen partial pressure P_{O2} relevant to nuclear fuels. Four phases are highlighted in the phase diagram:

- $Cr_2O_3(s)$
- $Cr_3O_4(s)$
- CrO(l)
- Cr(s)

The phase $Cr_3O_4(s)$ is neglected since it is characterized by a small area in the phase diagram. In addition, authors also report that the CrO(l) phase (oxidation state +2) is still hardly evidenced, due to its narrow stability area only at high temperature. Moreover, experimental synthesis of pure CrO(l) phase encounters difficulties when trying to accurately adjust and maintain the sintering parameters during the whole process [15]. For these reasons, and since the stability region of CrO(l) is defined by conditions of oxygen potentials and temperature far from typical reactor operating conditions, this phase was neglected in the implementation of the solubility model in the SCIANTIX code.

As a result, a simplified solubility thermodynamic model has been developed combining all the relevant experimental data. The solubility law was obtained by thermodynamics considerations, leading to the following formula:

$$\log_{10}(y_{cr}) = q\ \log_{10}(P_{O2}) + V + \frac{U}{T} \tag{9}$$

where e y_{Cr} is the chromium solubility, P_{O2} is the oxygen partial pressure, T is the temperature, V and U are coefficients coming from the linearization of the Gibbs' free energy and q is a function of the stoichiometry of the soluble species. Coefficients were determined by fitting the experimental data, leading to solubility laws for oxide and metal phases shown in Figure **3**. The oxygen potential has a primary role in determining the stable chromium phase at a certain temperature. Few studies have been carried out to model from a thermo-chemical perspective and accounting for the FP evolution in the LWR fuel conditions to determine oxygen potentials and its variation during irradiation. Curti and coauthors focused on the thermodynamic description of chromium-doped fuel systems. The final model calculates complete thermodynamic equilibrium in a conventional or Cr-doped UO_2 fuel rod irradiated in a PWR, using detailed model inventories with a defined average burnup. It includes, besides stoichiometric solids and ideal gas, a complex UO_2 solution with U^{5+}, $Cr^{3+,}$ Pu, minor actinides and lanthanides as minor solutes, a quinary (Mo, Pd, Rh, Ru, Tc) solid solution representing ϵ-particles, a binary (Ba, Sr)ZrO_3 solid solution representing a very simplified "grey phase". The main results of this work are thermodynamic equilibrium calculations for PWR Cr-doped UO_2 fuel at 60 GWd/tHM burnup. Curti and coauthors found that, between 400°C and 1400°C, the speciation of chromium is dominated by a separate pure Cr_2O_3(cr) phase. At higher temperatures, a phase transition between the oxide phase and the metal one is observed. The phase exchange between Cr - Cr_2O_3 was modelled with the following function:

$$f(T) = 1 - \exp\left(A_1(T - A_2)\right) \tag{10}$$

where A_1 and A_2 are appropriate coefficients, and $f(T)$ describes the molar fraction of Cr; then the molar fraction of Cr_2O_3 is obtained by subtracting $f(T)$ from 1. The effect of the burnup is taken into account considering that:

- A higher burnup and, thus, a higher production of FPs, would make the phase transition faster.
- At the beginning of the irradiation life, the function should be a horizontal straight line since no phase transition is in place.

In this way, it is possible to consider how the presence of FPs can remove oxygen from chromium oxide molecules. This is done by weighting the endpoint of the function, represented by C_2, by the burnup [27].

The chromium content in the UO_2 lattice depends on both phase distribution and solubility laws. To increase the fidelity of the above-proposed models an optimization process was performed against experimental data by [24]. Only the solubility law of Cr(s) was optimized, together with the phase-change function, since this law was obtained by less experimental data concentrated in a small temperature region. On the other hand, the solubility law for the oxide phase was considered reliable, given the greater availability of experimental data. This optimization process aimed to properly describe the amount of chromium in the lattice for different temperatures and burnup conditions. In addition, acting only on the U, and V parameters is possible to account for different fabrications that influence the oxygen partial pressure. From these results some conclusions can be drawn:

- In the low-temperature range of the pellet, between the periphery and the radial position that reached approximately a temperature value of 1400°C, the soluble fraction of chromium in the UO_2 matrix is measured around a constant value of 0.1 wt% Cr, independent of temperature. The chromium fraction in excess is found as precipitate in UO_2 as an oxide secondary phase. The chromium speciation (both soluble and insoluble forms) in the cold section of the rod is comparable to the one recorded on a pre-irradiated rod of the same type under nominal operating conditions (with temperatures between 500°C and 1000°C).
- In the intermediate-temperature range of the pellet, between the radial position that reached 1500°C and the one that reached 1620°C-1790°C, the soluble fraction of chromium in UO_2 decreases significantly down to the range of 0.04 wt.% - 0.06 wt.% and, thus, abundant precipitation of metallic chromium is found as a secondary phase.
- In the high-temperature range of the pellet, between the radial position that reached 1620°C-1790°C and the centre of the pellet, the soluble fraction increases up to values in the range of 0.06 wt.% - 0.09 wt.%. Abundant precipitates are still observed.

It should be emphasized that the data are highly dispersed, and the considerations made about the average trend must take this uncertainty into account. This uncertainty is probably related to the experimental technique used for the experiment (EPMA), considering that the dopant concentration is quite low.

To reproduce the sudden decrease in the chromium content above ~1450°C, optimization was carried out only on the Cr phase, as this is the one for which less experimental data are available and about which there is therefore more uncertainty. Results are shown in Figure **3**. The results obtained downstream of the optimization process suggest a faster transition between Cr_2O_3(s) and Cr(s) and lower solubility of the Cr(s) phase. Parameters of the optimized models are shown in Table 1.

Table 1. Parameters value obtained from the optimization process compared with nominal ones. The U and V coefficients refer to the solubility law for the Cr metal phase

Quantity	**Nominal values**	**Optimized values**
U (J/mol)	28160	22989.0
V (J/K mol)	-6.0760	-5.9483
C1 (-)	0.0050	0.0017
C2 (-)	1800	1502

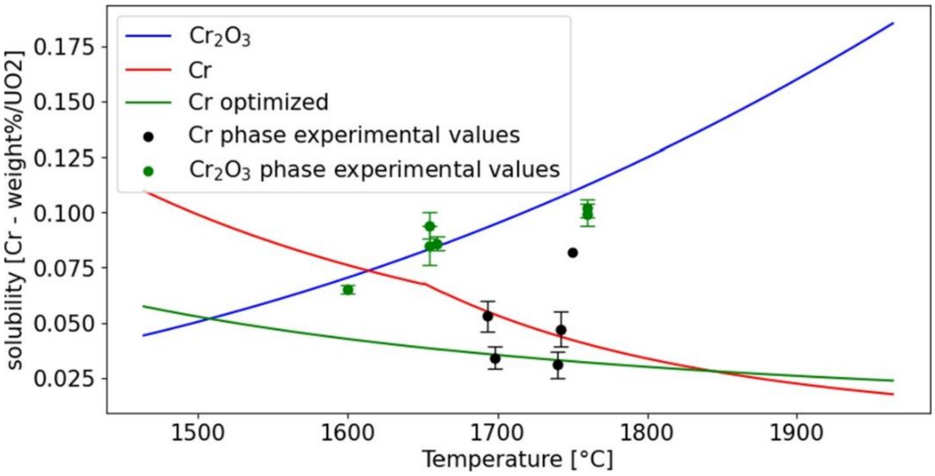

Figure 3: Comparison between the solubility model from literature [23] and the optimized one [27] against experimental data [24].

2.2.2 Fission gas diffusivity model

FGR is a complex multi-step process:

1. FG is produced by fissions in the bulk UO_2 lattice.
2. Trapping of the insoluble gas in intragranular bubbles and its resolution back into the lattice by irradiation occurs and can be assumed to rapidly reach equilibrium under most conditions of practical interest.
3. The resultant concentration of gas in the bulk diffuses to the grain boundaries (with the diffusion rate during equilibrium trapping and resolution captured by an effective diffusion coefficient) and forms inter-granular bubbles.
4. Growth of the inter-granular bubbles leads to fuel swelling, bubble interconnection, and gas release upon the formation of percolating pathways to a free surface.

Due to considerations about chromium precipitates at the grain boundary and considering that the probable chromium concentrations of commercial interest are rather low (~1000 - 1200 ppm), the effect of precipitates on intragranular diffusion was neglected. It may be relevant only in the case of doping with large concentrations consequently, the only effect related to grain boundaries is their reduction, since the doped fuel has larger grains.

Here, the focus is on the intra-granular gas behaviour, which is controlled, among other factors, by the grain size and the gas diffusivity. The fission gas diffusivity for undoped UO_2 is given by the Turnbull model [32]:

$$D = D_{01} + D_{02} + D_{03} \tag{11}$$

$$D_{01} = 7.6\ 10^{-10}\ \exp\left(-4.86\ \frac{10^{-19}}{k_B T}\right) \tag{12}$$

$$D_{02} = 5.64\ 10^{-25}\ \sqrt{\dot{F}}\ \exp\left(-1.91\ \frac{10^{-19}}{k_B T}\right) \tag{13}$$

$$D_{03} = 8\ 10^{-40} \dot{F} \tag{14}$$

where D_1, D_2, and D_3 represent the intrinsic, irradiation-enhanced, and athermal contributions to fission gas diffusivity, respectively. According to the fact that the equilibrium between Cr_2O_3 and Cr occurs at an oxygen potential that is commensurate to a hyper-stoichiometric fuel, as found in the work by Cooper [28], this formula was modified by adding a term accounting for uranium vacancy excess, retrieving a formulation discussed in [29], by adding the term $D_4 = h^2 j_v V_U$ where h is the interatomic jump distance (m), j_v the vacancy jump rate (-), and V_U the vacancy induced by doping. The uranium vacancy concentration is expressed by

$$V_U = \left(\frac{3}{2}\right)^2 \left(\frac{K_2}{K_1}\right) [Cr^{3+}]^2 \tag{15}$$

In which it is assumed that all the oxygen introduced as chromium-oxide in the fuel is retained in interstitial positions, leading to the formation of an equal number of oxygen vacancies. Another possibility, according to the recent work by Murphy et al. [26], is to consider one single oxygen vacancy per chromium atom in the lattice, leading to the following expression

$$V_U = \left(\frac{K_2}{K_1}\right) [Cr^{3+}]^2 \tag{16}$$

The results of calculations are shown in Figure 4. It must be stated that the uncertainty associated with the intra-granular (lattice) gas atom diffusion coefficient plays an important role in limiting the accuracy of FGB predictions. White and Tucker [30] postulated that the main cause of the observed discrepancies between the model and experiment in terms of FGR lay in the uncertainties in the lattice diffusion coefficients. Matzke [31] demonstrated a scatter of about two orders of magnitude, depending on the considered temperature, between different experimental data sets. In fact, a factor of 100 was considered also by Pastore and coauthors [32] to make a sensitivity analysis on FGR. Therefore, the comparison presented must be considered qualitatively, noting that the correction is considerable at intermediate temperatures and that it is associated with a physical process of creating uranium vacancies.

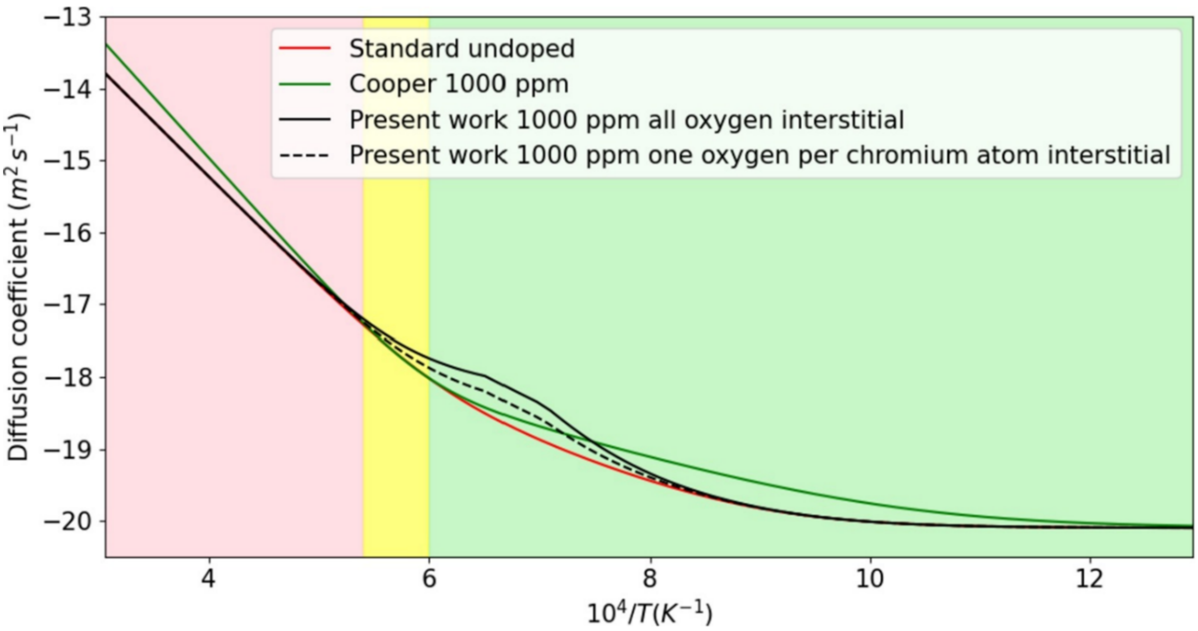

Figure 4: Value of diffusion coefficient (logscale) compared to the standard undoped one and the one derived by Cooper and coauthors [28]. It is highlighted the amount of chromium oxide, in wt ppm, used to dope the UO_2 fuel.

2.2.3 Separate-effect assessment

Here, model results are compared with separate-effect experiments available in literature. The comparison between results obtained with the Cr-solubility model implemented in SCIANTIX and experimental data by Riglet-Martial et al. is presented in Figure 5. The added value of the optimized model compared to the standard one is the capability of reproducing the rapid decrease in chromium content. In contrast, the calculated results have a different trend in the high-temperature region (purple colour in Figure **5**); this can be attributed to the fact that the optimized laws have a monotonic trend in temperature. The data which are used to optimize the Cr-solubility and phase evolution models, can be well reproduced by the new SCIANTIX model. However, this approach is limited and does not allow a proper understanding and description of the behaviour of chromium in the UO2 lattice during irradiation. To address these limitations, the implementation of a surrogate model for describing the Cr-U-O phase diagram, obtained through CALPHAD calculations, is a future development of potential interest for the SCIANTIX code.

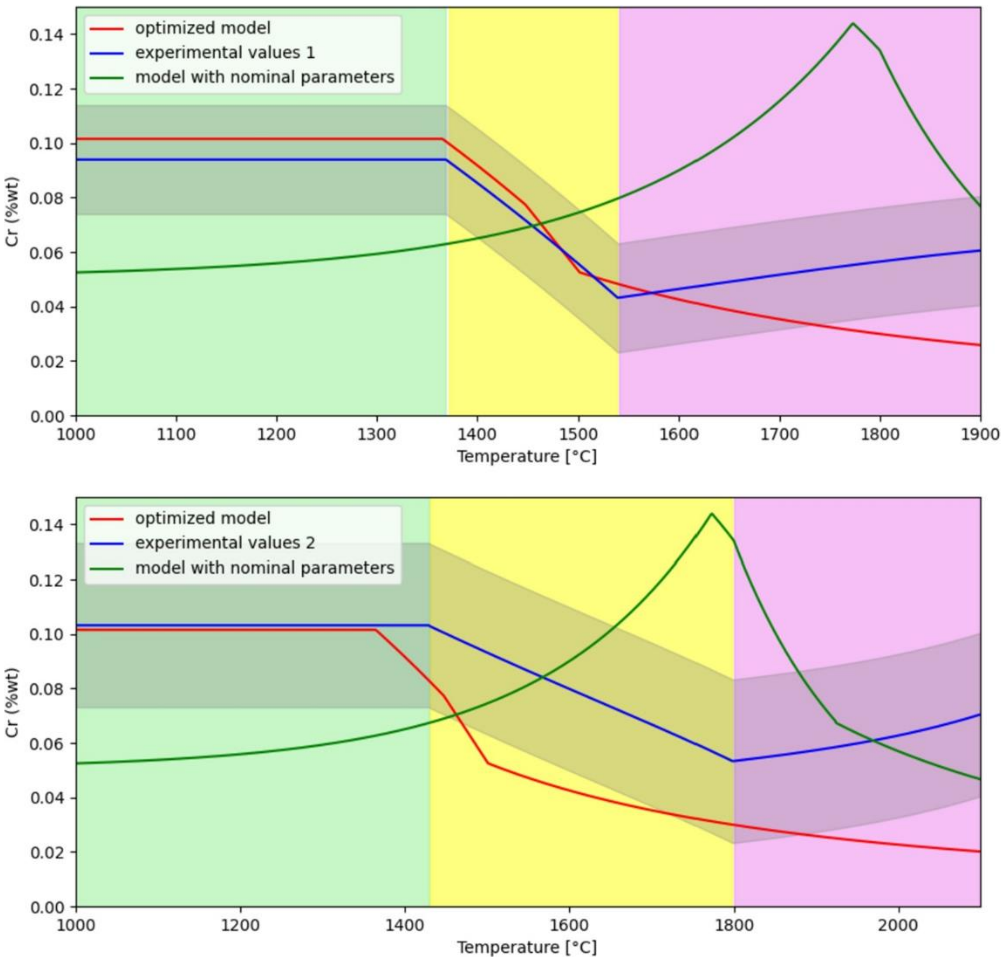

Figure 5: Plot of the experimental data from the work by Riglet-Martial and coauthors [24], in blue (experimental values 1 and 2), results obtained with the optimized model, in red and results obtained from the model with nominal parameters, in green. Three regions are highlighted: the green one, representing the area in which chromium solubility is independent of the temperature, the yellow one, in which a sudden decrease of the chromium in the lattice is observed, and the violet one, where an increase in the chromium content is observed. The dark area around the blue lines represents the uncertainty related to the dispersed experimental data. Note that data related to experiment 1 stops at a lower temperature, due to different experimental conditions.

In addition, results obtained with the new model for the diffusion coefficient implemented in SCIANTIX have been compared with FGR experimental data by Killeen [33]. The author considered six small cylindrical samples, 2.1 mm diameter by 10 mm long, prepared with 2% enriched UO_2 pellets by cutting and centreless grinding. Three of the samples were undoped and the other three were prepared from material that had been sintered using 0.5 wt.% (5000 ppm) of Cr_2O_3 as a dopant. Both sets of samples were prepared from the same original batch of UO_2 powder, the dopant being added only to one portion of this material. The grain size obtained at the end of the process was 6 µm for the undoped sample while for the doped one is in the interval 50 - 55 µm. Samples were electrically heated at a nominal temperature of 1460°C and irradiated in a neutron flux of $3.3\ 10^{17}$ n m^{-2} s^{-1}. The samples were irradiated in pairs, with a reference sample and one doped sample in each pair, to three differing burnups, 0.14% FIMA, 0.30% FIMA, and 0.45% FIMA. After irradiation, the quantity of ^{85}Kr released into the capsules from each specimen was measured.

The comparison between the results obtained with the new diffusion coefficient and the experimental data is shown in Figure 6, with a reasonable good agreement with the experimental results and the corresponding empirical model. It should be understood in a purely qualitative sense because of the limited experimental data and the high uncertainty of the diffusion coefficient. Regarding the experimental results obtained by Killeen [31], since the sample considered in this experiment was doped with a large amount of chromium (5000 ppm), well above the solubility limit, there might be an effect of reduced intergranular diffusion, due to chromium precipitations at grain boundaries. This could explain why the model predictions are slightly higher than the experimental data. The key aspect that one is able to capture, going from a simulation with standard-size fuel grains (5 µm) to one with bigger-size grains (~ 50 µm), is that the FGR begins later and continues more gently during the irradiation time. This is explained by the lower surface-to-volume ratio: the saturation at grain boundaries occurs earlier, due to the presence of fewer grain boundaries, as a direct result of larger grains. Thus, grain boundaries are less able to store FGs in fuel with bigger grains. At the same time, this is counterbalanced by the greater distance to travel for each gas atom, which causes the release to proceed at a slower rate, ultimately leading to greater retention of FGs, resulting in reduced pressure in the fissure/plenum but greater gaseous swelling.

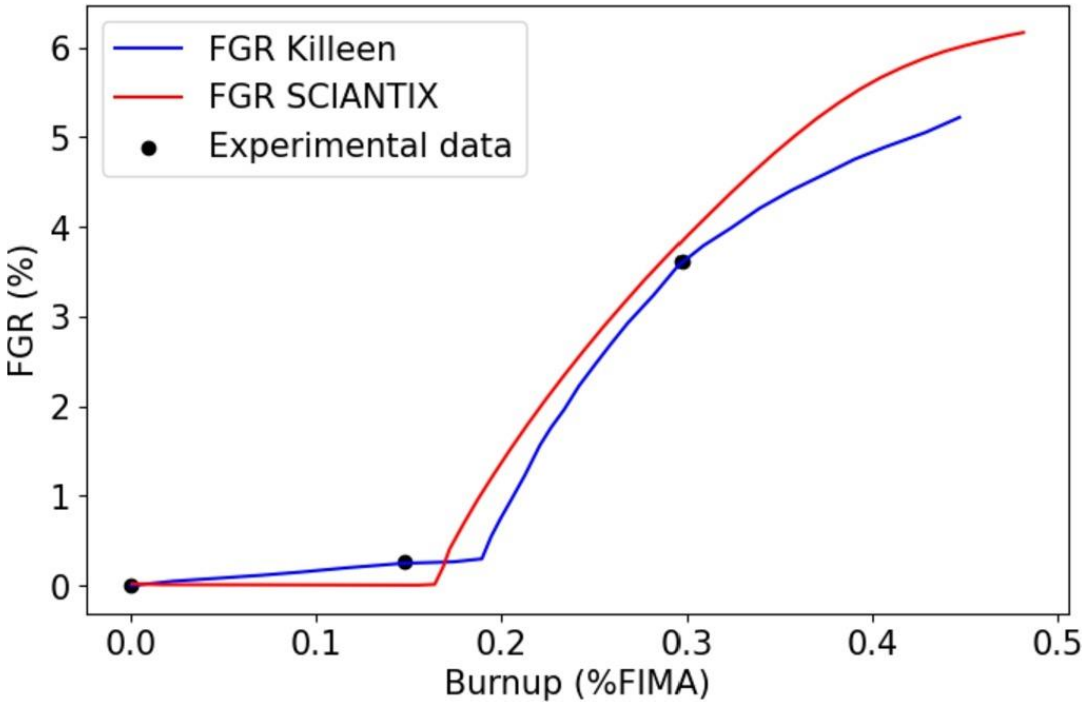

Figure 6: Comparison of FGR values obtained with the diffusion coefficient derived in this work, in red, experimental values, represented with black dots, and their interpolation, in blue.

2.2.4 Integral-scale assessment

Here it is presented the description of Rod 1 from the Instrumented Fuel Assembly (IFA)-677 that was irradiated in the OECD Halden Boiling Water Reactor (HBWR). The High Initial Rating Test IFA-677.1 was performed with the aim of investigating the performance of modern fuels subjected to high initial rating with respect to thermal behaviour, dimensional changes (densification and swelling), FGR, and PCMI. All rods were instrumented with pressure transducers and fuel centreline thermocouples on both ends. The test was loaded in the HBWR in December 2004 and completed six cycles of irradiation under HBWR conditions in September 2007, achieving a rig average burnup of ~26.3 MWd/kgUO^2. IFA-677.1 Rod 1 contained UO_2 doped with 900 ppm of Cr_2O_3 and 200 ppm of Al_0O_3. Fabrication characteristics of the rod considered in this work are illustrated in Table 2.

Table 2 Fabrication characteristics of IFA-677.1 Rod 1.

Fabrication Characteristics	**IFA-677.1 Rod 1**
Cladding material	Zircaloy-4
Fuel material	UO2 with additives
Fill gas	He
Total rod length (mm)	456.0
Total active fuel stack length (mm)	398.6
Drilled active section length, top (mm)	109.2
Drilled active section length, bottom (mm)	109.7
Pellet inner diameter, drilled sections (mm)	1.8
Pellet outer diameter (mm)	9.13
Diametral gap (µ)	170
Cladding thickness (mm)	0.725
Cladding outer diameter (mm)	10.75
Free volume (cm^3)	5.34
Fill gas pressure (MPa)	1.35
Fuel Cr_2O_3 content (ppm)	900
Fuel Al_2O_3 content (ppm)	200
Fuel U-235 enrichment (%)	4.94
Initial fuel density (kg/m^3)	10690
Fuel grain radius (µm)	28

The new model for the gas diffusion coefficient has been fully implemented in SCIANTIX. SCIANTIX receives input temperature history, fission rate, fuel hydrostatic stress, and fabrication data, then performs a 0D simulation of the fuel behaviour. The comparison of the predicted gas releases with the experimental results is crucial to assess the accuracy of the model. Results obtained with TRANSURANUS stand-alone and TRANSURANUS coupled with SCIANTIX are also shown, highlighting the added value of SCIANTIX models. The calculated FGR as a function of rod irradiation time is shown in Figure 7 along with the measured data (which are inferred from the inner rod pressure on-line measurement) and with BISON prediction, that are present as a comparison.

One can clearly see the contribution of SCIANTIX models, which allow for a more physical description of FGB, with sudden increases in conjunction with power ramps. This is possible through different models for intra-granular gas diffusion, with different trapping, resolution rates and intra-granular bubble evolution and grain boundary microcracking. Thus, results obtained with TRANSURANUS coupled with SCIANTIX are considered as references and are described in the following. FGR is well predicted during the first 300 days, which corresponds to a burnup of ~17 MWd/kgU. After that, FGR is underpredicted, with the calculated value at the end of life being 10.3% and the experimental value being 22%. As a comparison, BISON underpredicts less during irradiation but reaches a similar value after the last cycle. Two main spikes in the experimental FGR are identified in correspondence of two power increases, the first occurring at 280 days and the second at 450 days. In the simulations they are qualitatively present but there is a discrepancy of a factor 2 in the final FGR. Overall, the deviation can be considered acceptable, given the inherent modelling uncertainties for FGR [32].

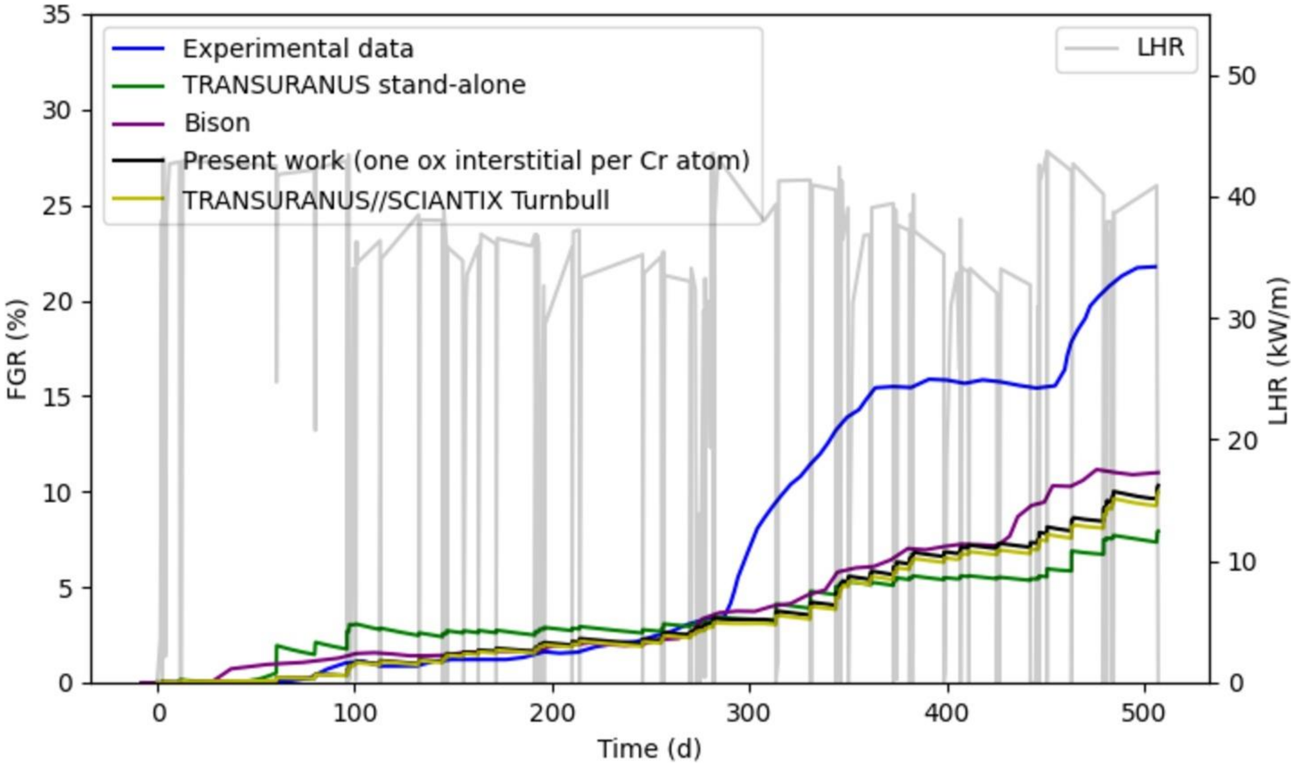

Figure 7. Comparison between FGR as a function of rod irradiation time for IFA-677.1 Rod 1: in blue the experimental data, in black results obtained in this work with TRANSURANUS coupled with SCIANTIX considering the new diffusion coefficient for gas diffusion, in yellow results obtained with TRANSURANUS coupled with SCIANTIX using the diffusion coefficient by Turnbull [33], in green results obtained with TRANSURANUS stand-alone, and in purple results obtained with BISON from the work by Cooper and coauthors [27]. The Linear Heat Rate values are also reported, in light grey, in the background.

For what concerns the integral assessment, the impact of the new model is limited on the global fuel performance analysis, but it paves the way for a more refined analysis of the diffusivity variation (e.g., by using defect balance equation or through an evaluation of the microstructure of the doped fuel from the complete phase diagram analysis). In addition, downstream of a performed sensitivity analysis, the discrepancy in the FGR results cannot be explained by uncertainty on input data. As an example, a typical factor of uncertainty of 5% in the input linear heat rate was considered in additional TRANSURANUS simulations [27], with a negligible increase of 2% on the calculated FGR. Likely, the explanation for the discrepancy between the experimental FGR and (both BISON and) TRANSURANUS calculations is to be found in the physical models describing the intragranular fission gas diffusivity in the fuel, and in the possible decreased capability of grain boundaries to store fission gas due to the presence of chromium precipitates at grain boundaries.

2.3 Model for athermal gas release

Several mechanisms of FGR exist, that are relevant in different temperature ranges. At high temperatures the thermal diffusion of fission gas dominates. At moderate temperatures, the irradiation-enhanced defect concentrations drive the fission gas diffusion, whereas at low temperatures, the athermal contribution is most relevant. The athermal fission gas release holds prime importance in reactors that operate at low temperatures, e.g., some designs of small modular reactors (SMRs), and, also, for fast reactors using fuels with high thermal conductivity, such as nitride fuels. Athermal fission gas release may occur via recoil or knockout mechanisms or be induced by the presence of open channels in the fuel matrix, i.e., the open porosity. Within the OperaHPC project, POLIMI focused on the latter.

Numerous endeavours have been undertaken to characterise athermal FGR, encompassing diverse methodologies from purely empirical approaches to the exploration of percolation phenomenon along grain boundaries. A mechanistic model considering the open porosity as a mean-field quantity was developed by Caisse and Van Uffelen [34], but it is expected to over-predict FGR since the athermal venting factor was described as a purely geometrical quantity and the fuel grain was treated as a spherical domain, therefore, neglecting the effects of the grain shape of the gas concentration gradient along the grain edge (Figure 8). Here, we describe a development of this model for the athermal FGR. The athermal FGR, defined as the fraction of gas vented from the fuel through its open porosity, is evaluated from the solution of the diffusion problem within tetrakaidecahedron (TKD)-shaped fuel grain [35], evaluating the fraction of the concentration gradient in the proximity of grain edges. The results were implemented in the SCIANTIX code thanks to a dedicated neural network, aimed at encapsulating the complex dependencies affecting the athermal release, whilst ensuring a computational time in line with FPC applications. Additionally, in the context of this analysis, semi-empirical models for solid FP swelling and fuel densification were incorporated as well, both relevant phenomena in low-temperature conditions. The consistency of the model is tested with data available in the literature.

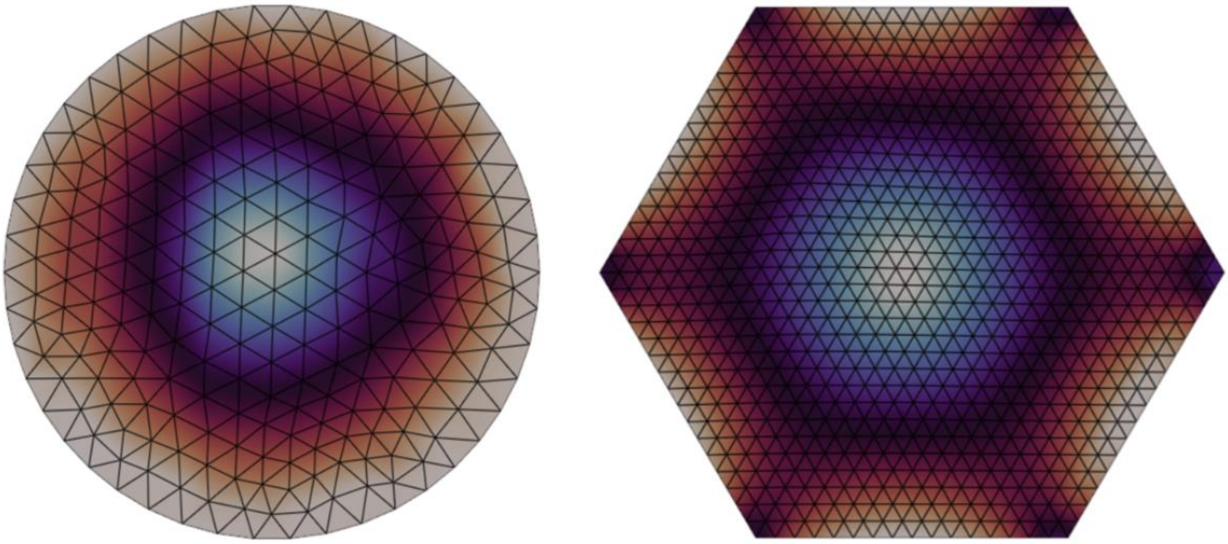

Figure 8: Comparison between the gas concentration in a section of a sphere (left) and in a section of a tetrakaidecahedron (right), from the solution of the gas diffusion problem. In the latter case, the gas concentration along the edge is non uniform.

2.3.1 Athermal venting factor

This section introduces the model for athermal fission gas release, built on the mechanistic framework developed by Claisse and Van Uffelen. To account for the complex dependencies influencing this process while maintaining computational efficiency suitable for fuel performance applications, artificial intelligence techniques are employed. Specifically, a synthetic dataset is generated using a high-fidelity finite element method code that solves the diffusion equation. This dataset is then used to train a feed-forward neural network. We considered the following equation for the accumulation rate of FG at grain boundaries:

$$\frac{dq}{dt} = (1 - f_{ath}\lambda_{ath})\left(D\frac{3}{a}\frac{\partial c}{\partial r}_{r=a}\right) - R \tag{17}$$

where D is the intra-granular FG diffusivity, a is the grain radius, c is the intragranular FG concentration, R is the release rate due to grain-boundary bubbles interconnection. Considering a fuel grain represented as a TKD, the athermal venting factor was defined in [34] as:

$$f_{ath} = \frac{S_{op}}{S_{TKD}} = 1.54\sqrt{P_{op}} \tag{18}$$

where S_{op} is the surface of the open-porosity and $S_{TKD}$is the surface of the TKD. In order to account for the concentration gradient along the edges, we introduced the corrective factor λ_{ath}, defined as the ratio of the average integral flux exiting from the grain within the radius of the open-porosity tunnel ϕ_{op} over the total average integral exiting flux ϕ_{tot}:

$$\lambda_{ath} = \frac{\phi_{op}}{\phi_{tot}} \tag{19}$$

To compute the corrective factor λ_{ath}, a high-fidelity code, written in MATLAB, was employed to solve the 2D gas diffusion equation in a section of a TKD (Figure 8, right) for several values of the grain-inclination angle, the fabrication porosity, the grain edge length, the burn-up, the temperature, the fission rate density and the initial gas concentration. Details and range of these parameters are illustrated in Table 3.

Given the involved non-linearities in the solution of the 2D gas diffusion equation (e.g., the dependence of the diffusivity from the temperature and the fission rate), a surrogate model for λ_{ath} was developed to encapsulate all the dependencies. A feed-forward neural network (FNN) was chosen for its simplicity and interpretability. The FNN architecture features ten neurons and was trained on a synthetic dataset generated by high-fidelity simulations. The dataset contains 10,348 observations with a seven-dimensional feature space representing the dependencies. The data was randomly split into training (70%), validation (15%), and test (15%) subsets. The network training was optimized using the Levenberg–Marquardt algorithm, and its performance was evaluated using the mean square error (always lower than 0.0043). The surrogate model for λ_{ath} has been implemented and SCIANTIX and used for the solution of (Eq. 17) in the grain-boundary

Table 3. Definitions, ranges and units of the parameters used in the solution of the 2D gas diffusion equation.

Quantity	**Definition**	**Range**	**Unit of Measurement**
θ	Grain-edge inclination angle	90 - 135	°
P_{fab}	As-fabricated porosity	2 - 9	%
l	Grain-edge length	3.67 - 11	µm
β	Burnup	0 - 50	MWd/kgUO2
T	Temperature	300 - 1600	K
S	Gas generation rate		at/m3-s
	- Irradiation	10^{18}-10^{20}	
	- Annealing	0	
C_0	Initial gas concentration		at/m3-s
	- Irradiation	0	
	- Annealing	10^{19}-10^{24}	

2.3.2 Connected phenomena

To achieve a more physical interpretation of the relationship between the open porosity P_{op} and the fabrication porosity P_{fab}, the linear interpolation inferred in [34] was replaced by the following new semi-empirical fit (Figure 9):

$$P_{op} = \alpha P_{fab} + \frac{a}{1 + \exp\left(-c\left(P_{fab} - b\right)\right)} \tag{20}$$

With a= 2.8 %, b= 5.5 %, and α = 0.05. We can highlight the relation between the open porosity and the fabrication porosity as the co-occurrence of two effects. The first one is isotropic in nature and characterized by the linear term, the second one is anisotropic and ascribable to the percolation mechanism that occurs at a threshold value of P_{fab}.

In addition, we included the effect of the solid FPs on the fuel density (ρ), through the following equation:

$$\rho = \frac{TD}{(1 - P)\left(1 + \left(\frac{\Delta V}{V}\right)_{FP}\right)} \tag{21}$$

Where the swelling due to solid FPs is evaluated according to the legacy Olander model [35], TD is the fuel theoretical density, and P is the total porosity.

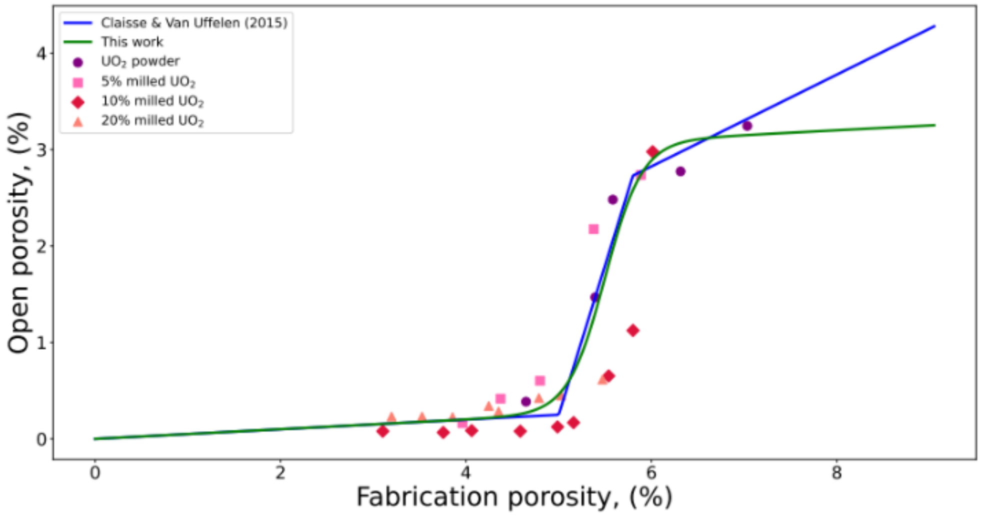

Figure 9: Comparison between this work's fit with the one inferred by Claisse and Van Uffelen, and experimental data [35]

Lastly, we introduced a burnup dependence for the densification process given by:

$$\frac{df_d}{d\beta} = k_\beta f_d + k_{T1}(\exp k_{T2}T) \tag{22}$$

Where f_d is the densification factor, $k_\beta = 2$, $k_{T1} = 0.006$, $k_{T2} = 0.002$ are determined from the experimental data in Figure 10. The densification factor is then employed to reduce the fabrication porosity up to a constant residual porosity taken as 75% of the initial fabrication porosity.

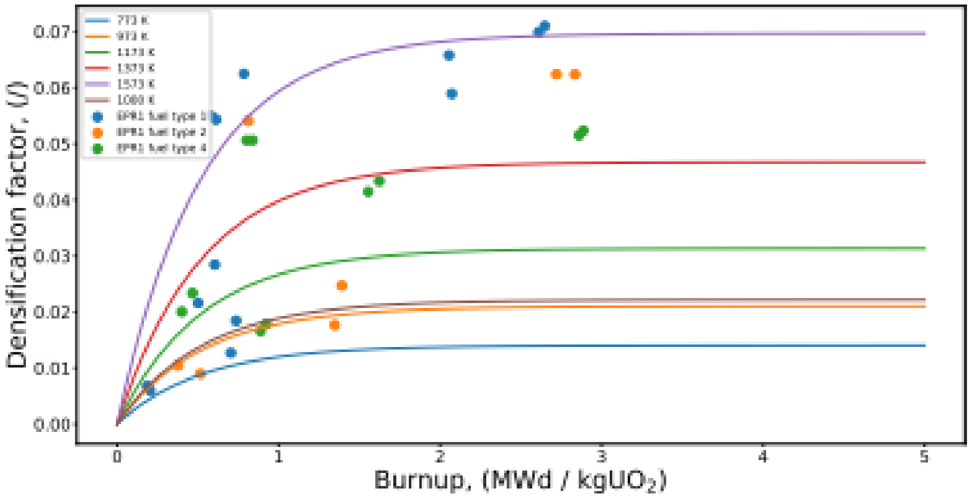

Figure 10: Densification factor as a function of the burnup according to Eq. (20) evaluated at different temperature levels, compared to experimental data [36].

These three additional phenomena (dependence of the open porosity from the fabrication porosity, solid fuel swelling and densification) have been implemented in SCIANTIX, on top of the correction of the athermal venting factor by λ_{ath}, to have a meso-scale, yet comprehensive, description of the athermal FGR.

2.3.3 Separate-effect assessment

The predictive capabilities of the presented model are tested using data available in the open literature. Specifically, a set of separate effect tests was conducted to first assess the performance of SCIANTIX in standalone conditions, against the Kashibe and Baker separate-effect experimental cases. Additionally, to further explore the behavior of the athermal FGR model across a broader range of temperatures and burnup values, a synthetic dataset was generated. This dataset was build considering the same fuel composition of the Baker tests and spanning a temperature range from 373 to 2073 K and irradiating until a final burnup level equal to 50 MWd/kgUO2. The test cases are mapped in Figure 11. A summarising result of the three models presented in the previous section is depicted in Figure 12, while an illustrative athermal FGR prediction is shown in Figure 13.

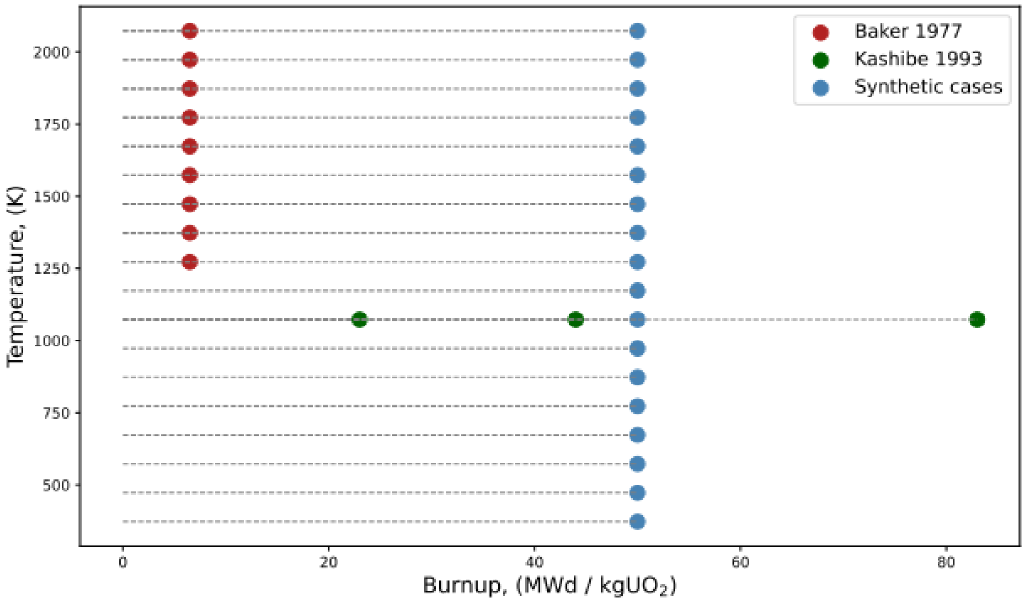

Figure 11: Experimental and synthetic cases employed in the separate effect tests of the athermal FGR model.

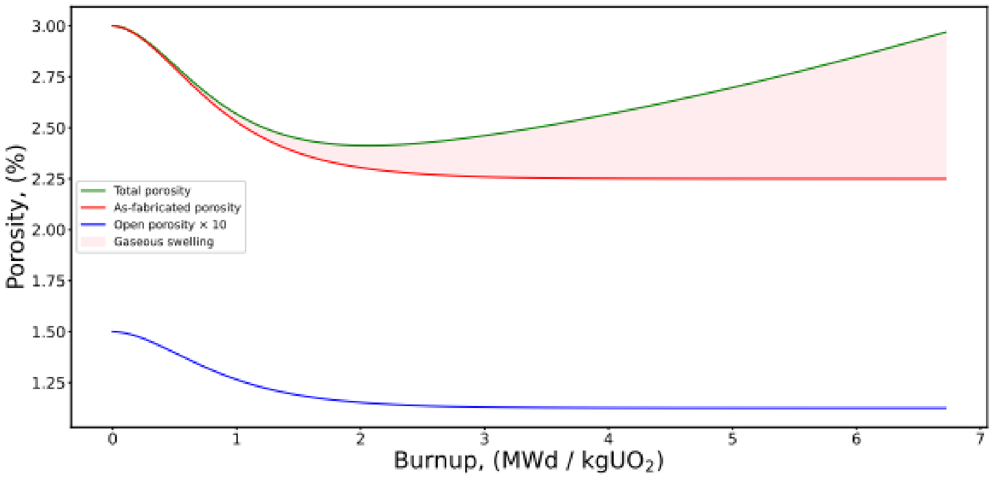

Figure 12: Evolution of the open porosity, alongside the fabrication and total porosity in the Baker test case at 1273 K. For the sake of readability, the values of the open porosity have been enlarged by a factor of 10. With irradiation, the fabrication porosity undergoes densification according to our model until a residual porosity value is reached. After, the total porosity increases due to FG/FP swelling contributions.

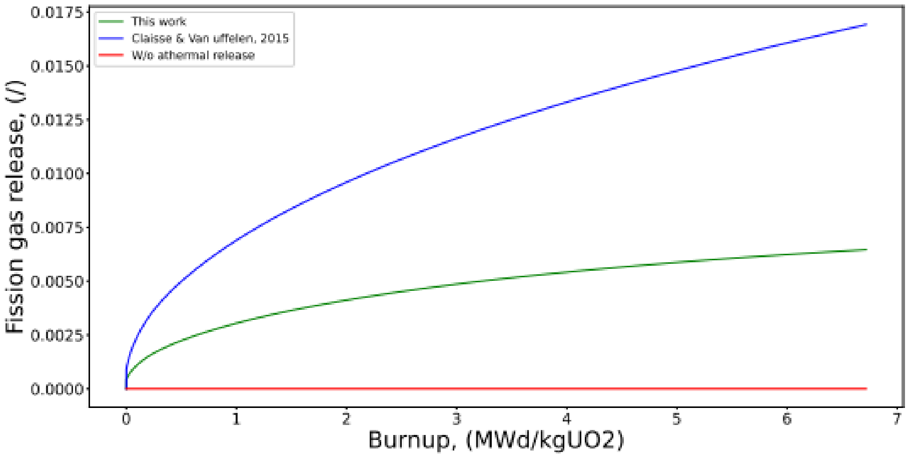

Figure 13: Athermal FGR, model comparison for the Baker test case at 1273 K. The FGR predicted by our model is lower than the Claisse and Van Uffelen model, as expected from the application of the corrective factor λ_{ath}.

We used the developed athermal FGR model to map a temperature-burnup space based on the coordinates at which FGR exceeds 1% for the different studied cases, compared to the legacy Halden threshold. As depicted in Figure 14, the Halden threshold slightly surpasses the athermal boundary outlined in our mapping, consistently serving as an upper limit for the region of athermal release as defined by our model. This trend persists throughout the entire domain where the Halden threshold remains valid, with exceptions found in sections of the graph influenced by the highest temperatures encountered in the Baker cases. This observation aligns with the fact that the Halden threshold is formulated based on the fuel centerline temperature, whereas our analysis considers local temperature values, which are more representative of the separate-effect tests in the SCIANTIX database. Consequently, the thermal gradient in the fuel pellet would lead to a vertical shift of the red (Halden) curve on the y-axis. Once more, all the experimental cases under consideration (base irradiations of AN3. CONTACT1, REGATE, HATAC-C2, with low FGR) occupy a portion of the temperature-burnup space governed by athermal FGR. Therefore, this map can serve as a tool for evaluating the predicted region of FGR, whether influenced primarily by athermal behavior or thermal diffusion.

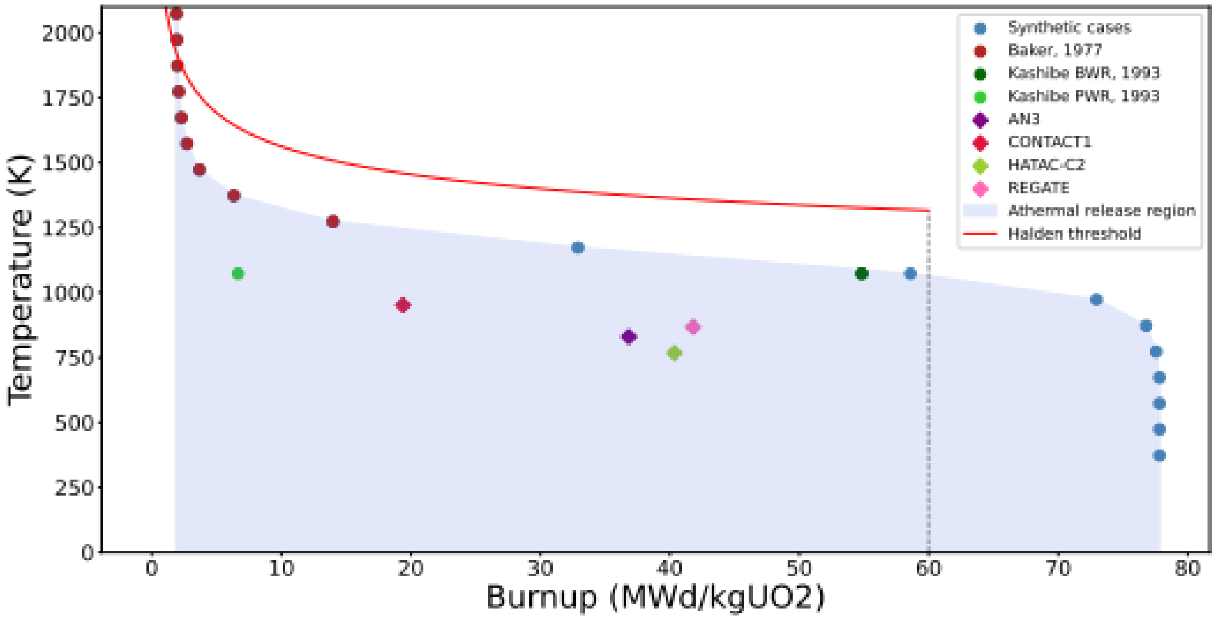

Figure 14. Mapping of the local temperature-burnup space based on the coordinates at which fission gas release exceeds 1% for the different studied cases, compared to the Halden threshold. For comparison, average temperature-burnup points from the base-irradiations of AN3, CONTACT1, HATAC-C2 and REGATE have been included.

2.4 Conclusive remarks

The selection and implementation of advanced behavioural models for FGB at POLIMI, in the context of Task 4.2, have enabled a more accurate description of:

1. **HBS evolution**: A novel modelling approach has been developed to simulate the transition to and depletion of fission gases in HBS. The assessment against experimental data and previous semi-empirical models confirm its reliability.
2. **Chromia-doped UO_2 fuels**: The chromium solubility and phase evolution models have been refined and extended to better align with experimental data, including EPMA datasets. A new fission gas diffusion coefficient, consistent with doping-induced defect concentrations, has been implemented, providing an improved representation of fission gas retention in doped duel. The coupling of SCIANTIX with the TRANSURANUS fuel performance code has demonstrated the integral applicability of these advancements.
3. **Athermal FGR**: A mechanistic model incorporating grain geometry effects for athermal FGR was developed. This model, supported by a neural network for computational efficiency, and meso-scale semi-empirical models for solid FP swelling and fuel densification has been assessed against literature data, demonstrating its relevance for base irradiation conditions of LWR and low-temperature reactor designs.

The incorporation of these advanced models into SCIANTIX improves its meso-scale modelling capabilities and pave the way for integral-scale applications by applying the coupled suite SCIANTIX-OFFBEAT developed and assessed in the frame of the current OperaHPC project.

3. Review of physical models for OFFBEAT and 3D methodology for gap conductance

In the context of Task 4.2, EPFL reviewed and selected a set of models to be implemented in OFFBEAT specifically within Task 4.4 and, more generally, throughout the project. The focus was mainly on Loss of Coolant Accidents (LOCAs), Reactivity Initiated Accidents (RIAs), contact modelling and fuel-to-cladding gap heat transfer.

3.1 Selection of models for LOCA scenarios

In LOCA scenarios large cladding deformation and *ballooning* might occur, making the traditional small-strain approximation insufficient. Therefore, two different large-strain solvers were implemented in OFFBEAT: a *Total-Lagrangian* and an *Updated-Lagrangian* solver. The two differ for the approach used to account for the domain geometric non-linearity, that is the deformation of the computational domain as transient progresses. In the Total-Lagrangian method, the momentum conservation equation is solved on the undeformed geometry with initial volume Ω_0 and boundary Γ_0 as shown in (23).

$$\begin{aligned}\int_{\Omega_0} \frac{\partial}{\partial t}\left(\rho_0 \frac{\partial \vec{D}}{\partial t}\right) d\Omega_0 &= \oint_{\Gamma} \vec{n} \cdot \boldsymbol{\sigma} \; d\Gamma \\ &= \oint_{\Gamma_0} (J\, \boldsymbol{F}^{-T} \cdot \vec{n_0}) \cdot \boldsymbol{\sigma} \, d\Gamma_0\end{aligned} \tag{23}$$

In the equation above, Nanson's relation (i.e. $\vec{n} d\Gamma = J\boldsymbol{F}^{-T}\vec{n_0}\, d\Gamma_0$) are used to relate the initial area vector $\vec{n_0}\, d\Gamma_0$ with the deformed area vector $\vec{n} d\Gamma$, with J representing the Jacobian determinant of the deformation gradient (i.e. $J = \det(\boldsymbol{F})$). In the Updated-Lagrangian method the computational domain is updated at every time-step (using OpenFOAM's native mesh-update capabilities) and the momentum balance equations are solved on the so-called "updated" configuration as shown in Eq. (24):

$$\int_{\Omega_u} \frac{\partial}{\partial t}\left(\rho_u \frac{\partial \vec{D}}{\partial t}\right) d\Omega_u = \oint_{\Gamma_u} (j\, \boldsymbol{f}^{-T} \cdot \vec{n_u}) \cdot \boldsymbol{\sigma} \, d\Gamma_u \tag{24}$$

Here the Nanson's relationship ($\vec{n} d\Gamma = j\boldsymbol{f}^{-T} \cdot \vec{n_u} d\Gamma_u$) use the relative deformation gradient $\boldsymbol{f}$ and its Jacobian determinant j. Further details on the dynamic mesh feature can be found in (Brunetto et al., 2021). Despite being equivalent from the mathematical point of view, the Total- and Updated-Lagrangian approaches can differ in terms of numerical performances. As documented in (Cardiff et al., 2017), their numerical implementation in a Finite Volume framework with a segregated solution algorithm like the one of OFFBEAT can produce some differences in robustness and convergence. For most cases relevant to LOCA analysis, the Updated-Lagrangian approach used in OFFBEAT was found to provide more stable results (Cardiff et al., 2017).

Besides addressing the geometric non-linearity, large-strain analysis requires a coherent formulation of the strain tensor. Hence, apposite large-strain tensor definitions were implemented in OFFBEAT. The main ones are the Green-Lagrange and the Euler-Almansi definitions of strain (see Eq. (25) and Eq. (26) respectively).

The Green-Lagrange strain tensor $\boldsymbol{E}$:

$$\boldsymbol{E} = \frac{1}{2}(\boldsymbol{F}^T\boldsymbol{F} - \boldsymbol{I}) = \frac{1}{2}\left[\nabla\vec{\mathrm{D}} + \left(\nabla\vec{\mathrm{D}}\right)^T + \left(\nabla\vec{\mathrm{D}}\right)^T \cdot \nabla\vec{\mathrm{D}}\right] \tag{25}$$

is easily recognizable as the direct generalization of the strain tensor in the small-strain approximation, the only difference being the presence of the non-linear term $\left(\nabla\vec{\mathrm{D}}\right)^T \cdot \nabla\vec{\mathrm{D}}$. Analogously to the small-strain tensor, $\boldsymbol{E}$ is a measure of the deformation of the body with respect to its initial configuration.

The Euler-Almansi strain tensor $\boldsymbol{e}$:

$$\boldsymbol{e} = \frac{1}{2}(\boldsymbol{I} - \boldsymbol{F}^{-T}\boldsymbol{F}^{-1}) = \frac{1}{2}\left[\nabla\vec{\mathrm{D}} + \left(\nabla\vec{\mathrm{D}}\right)^T - \left(\nabla\vec{\mathrm{D}}\right)^T \cdot \nabla\vec{\mathrm{D}}\right] \tag{26}$$

Is instead a metric for the deformation of the body with respect to its current configuration. The Green-Lagrangian and the Euler-Almansi formulations are therefore two different metrics for strain because of the different reference configuration considered (initial and deformed respectively), but they both reduce to the small-strain definition in case of infinitesimal deformations.

To summarize, OFFBEAT now includes four different mechanical solvers, listed in Table 4. These can be categorized as either total or incremental solvers, depending on whether their primary unknown is the total displacement field $\vec{D}$, or the incremental displacement $\overrightarrow{DD}_{\Delta t}$ occurring during the current time step Δt. The Small Strain Updated solver was implemented in OFFBEAT as an incremental version of the traditional small-strain approach. Similar to the Large Strain Updated-Lagrangian approach, this solver solves the momentum continuity equation for the incremental displacement field and updates the computational domain at each time step. However, it retains the main assumptions of small-strain theory, meaning it does not incorporate Nanson's formula and employs a linear strain tensor. The Small Strain Updated solver enables the consideration of geometric non-linearities in large deformation scenarios to a certain degree of approximation. However, its accuracy remains limited due to the linear definition of the strain tensor and the simplified formulation of the momentum continuity equation.

Table 4: Summary table of the mechanical solvers available in OFFBEAT

Mechanical Solver	Solver Type	Mesh Update	Strain Tensor Definition
Small Strain	Total	×	Linear
Small Strain Updated	Incremental	✓	Linear
Large Strain Total-Lagrangian	Total	×	Euler-Almansi, Green-Lagrange, Hencky or Linear
Large Strain Updated-Lagrangian	Incremental	✓	Euler-Almansi, Green-Lagrange, Hencky or Linear

3.1.1 High-temperature creep model

For standard operating conditions, OFFBEAT applies the creep model developed by Limbäck and Andersson (Limbäck & Andersson, 1996) for Zircaloy cladding. This model provides the creep rate as a combination of primary and secondary creep rate, where the secondary creep rate is in turn obtained by summing a thermal-induced and an irradiation-induced component. The validity of this model is limited to temperatures below 700 K.

The OFFBEAT Zircaloy creep model is extended to high temperature conditions by following the work of Pastore et al. (Pastore et al., 2021). The model defines three different temperature regimes:

- A normal operation regime for temperatures below 700 K;

- A high temperature regime for temperatures above 900 K;
- A transitional regime for temperature between 700 and 900 K.

Different creep rate correlations are used for the low- and high-temperature regimes, while a linear interpolation is used to evaluate the creep rate in the transitional regime. Below 700 K, the standard Limbäck model is used, while the high temperature creep strain rate correlation has the form of a Norton power equation, as shown in Eq. (27):

$$\dot{\varepsilon}_{creep} = A \exp\left(-\frac{Q}{RT}\right) \sigma_{eff}^{n} \qquad (27)$$

where $\dot{\varepsilon}_{creep}$ is the effective creep strain rate, A is a strength coefficient expressed in $MPa^{-n}s^{-1}$, Q is the activation energy expressed in $\frac{J}{mol}$, T is the temperature, σ_{eff} is the effective Von Mises stress in MPa, and n is a dimensionless correlation parameter. The value of $A, Q$and n depend upon the volumetric fraction of β-phase present in Zircaloy, for which a specific model is introduced, and are summarized in Table 5. These model parameters are sourced from (Erbacher et al., 1982a) and (Markiewicz & Erbacher, 1988).

Table 5: Table of A, Q and n parameters dependence on the volumetric fraction of Zircaloy phases.

Zircaloy Phase		$A\ (MPa^{-n}s^{-1})$	$Q\ (J/mol)$	$n\ (-)$
α		8737.00	3.21e5+24.69(T-923.15)	5.89
α, β (50%-50%)	if $\dot{\varepsilon}_{creep} \leq 3\mathrm{e}-3$	0.24	102366.00	2.33
	if $\dot{\varepsilon}_{creep} > 3\mathrm{e}-3$	Lin. Interp. of ln(A)	Lin. Interp.	Lin. Interp.
β		7.90	141919.00	3.78

3.1.2 Phase transition model for Zircaloy

Beyond an onset temperature of around 1080 K, the hexagonal crystal structure (i.e. α-phase) of Zircaloy progressively transitions towards a more stable cubic crystal structure (i.e. β-phase). The dynamics of this transition depends mainly on the heating or cooling rate of the cladding. One of the main effects of the crystallographic transition from α- to β-phase is the enhancement of the thermal creep rate during a LOCA.

For this reason, OFFBEAT has been provided both with a static and a dynamic model for the β-phase transition of Zircaloy. The static model, derived from Forgeron (Forgeron et al., 2000), is valid when the kinetics of the transition can be neglected (i.e. during slow temperature transients) and consists of a simple correlation that relates the local cladding temperature T to a specific β-phase volumetric fraction y_{eq}. The Forgeron's equation is expressed by means of Eq. (28):

$$y_{eq} = 1 - e^{-[C\cdot(T-T_0)]^n} \qquad (29)$$

where $C = 8.4 \times 10^{-3}\ 1/°C$, $T_0 = 749\ °C$ and $n = 2.9$ (Forgeron et al., 2000).

For the study of LOCA transients, where temperature ramps in the cladding are generally rapid, a better estimation of the volumetric fraction of β-phase is typically obtained through a dynamic phase transition model. According to the model by Massih (Massih, 2009) implemented in BISON (Pastore et al., 2021), the evolution of the volumetric fraction of β-phase in Zircaloy is governed by the differential equation shown in Eq. (30):

$$\frac{dy}{dt} = k(T)[y_s(T) - y] \qquad (31)$$

where y is the volumetric fraction of β-phase, k is a rate parameter expressed in s^{-1} :

$$k(T) = k_0 \exp\left(-\frac{E}{k_b T(t)}\right) + k_m \qquad (32)$$

with $k_0 = 60457 + 18129 \left|\frac{dT}{dt}\right|$, $\frac{E}{k_b} = 16650\ K$, and $k_m = 0$ (if the transition is from α to β), or $k_m = 0.2$ (if the transition goes in the opposite direction). y_s, the equilibrium value of y, is computed as:

$$y_s = \frac{1}{2}\left[1 + \tanh\left(\frac{T - T_c}{T_s}\right)\right] \qquad (33)$$

where $T_c = 1159 - 0.096w$ and $T_s = 44 + 0.026w$, with w being the hydrogen concentration in ppm. Both k and y_s depend on the temperature rate of change, thus allowing the dynamic model to more accurately reproduce the kinetics of the production of β-phase. The difference between the static and dynamic approaches can be visualized in Figure 15, that shows the verification of the model implemented in OFFBEAT against the reference model by Massih (Massih, 2009).

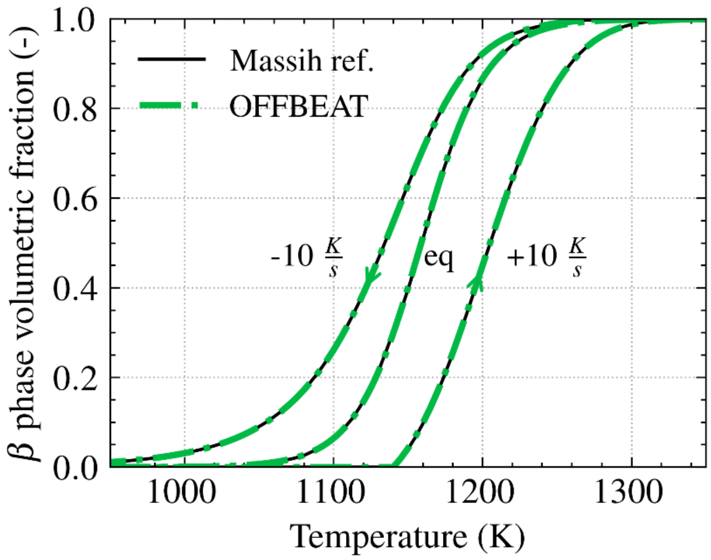

Figure 15 : Verification of the OFFBEAT model for β-phase transition of Zirconium compared to the model from Massih. The curve shown in the plot are obtained for a hydrogen concentration of 0 ppm.

3.1.3 Cladding burst failure model

The accurate prediction of the moment of cladding failure during a LOCA transient is of primary importance for fuel performance analysis. The assessment of cladding burst occurrence is typically performed by means of simplified burst criteria rather than with fracture dynamics, which would require an accurate modeling of fractures propagation and therefore a significant computational overhead to fuel performance computations.

As part of Task 4.2, OFFBEAT was thus provided with different failure criteria derived from BISON (Idaho National Laboratory, n.d.) for the Zircaloy material: an overstrain criterion, an overstress criterion and a plastic instability criterion.

- **Overstrain**. According to this failure criterion, the cladding is considered to fail as soon as the radially-averaged creep hoop strain (expressed as engineering strain) overcomes the limit of 40%.
- **Plastic instability**. The criterion considers the material to fail when the radially-averaged effective plastic strain rate reaches a limiting value of $2.78 \cdot 10^{-2}\ s^{-1}$.
- **Overstress**. The material is considered failed as soon as the local hoop stress overcomes a burst value computed as a function of temperature and oxygen concentration in the cladding (Erbacher et al., 1982b).

3.2 Selection of models for RIA: cladding visco-plasticity and failure criteria

To extend OFFBEAT's capabilities for Reactivity Initiated Accident (RIA) scenarios, which are essential for WP5 validation tasks, EPFL identified the most important gaps in the code modelling capabilities for this type of scenarios. To address these limitations, models were implemented to capture the anisotropic viscoplasticity of Zircaloy-4 cladding under high temperatures and strain rates, as well as PCMI-induced failure during RIA conditions. This work was partly conducted in the framework of a collaboration with CEA Cadarache, motivated by the common participation in the HERA benchmark (Reymond et al., 2024).

3.2.1 Cladding visco-plastic model for hydrided and unirradiated Zircaloy-4 cladding

During a RIA scenario, cladding experiences high temperatures, stresses, and strain rates. To account for this, the anisotropic viscoplastic model by M. Le Saux et al. (Le Saux et al., 2015) was implemented in OFFBEAT. This model describes the anisotropic mechanical behavior of unirradiated and hydrided Zy-4 (up to 1200 wt.ppm hydrogen) across relevant temperature (25–1100°C) and strain rate (3×10^{-4} to 5 s^{-1}) ranges. It employs a unified viscoplastic formulation, eliminating a stress threshold between elastic and viscoplastic regimes. The plastic anisotropy induced by the crystallographic texture of stress-relieved Zy-4 is captured using Hill's quadratic criterion:

$$\sigma_{eq}^{H} = \sqrt{\underline{\sigma} : \underline{\underline{H}} : \underline{\sigma}} \tag{34}$$

where σ_{eq}^{H} is the equivalent stress linked to the stress tensor $\underline{\sigma}$ via Hill's tensor $\underline{\underline{H}}$. In a cylindrical coordinate system (r, θ,z), we can express the equivalent stress as given in Eq. (35), where H_{rr}, $H_{\theta\theta}$, H_{zz}, $H_{r\theta}$, H_{rz} and $H_{\theta z}$ are Hill's parameters.

$$\sigma_{eq}^{H} = \sqrt{H_{rr}(\sigma_{\theta\theta} - \sigma_{zz})^2 + H_{\theta\theta}(\sigma_{zz} - \sigma_{rr})^2 + H_{zz}(\sigma_{rr} - \sigma_{\theta\theta})^2 + 2H_{r\theta}\sigma_{r\theta}^2 + 2H_{rz}\sigma_{rz}^2 + 2H_{\theta z}\sigma_{\theta z}^2} \tag{35}$$

The model further defines the viscoplastic strain rate $\dot{p}$ as a function of the equivalent stress, cladding temperature, hydrogen concentration and the cumulated equivalent viscoplastic strain p as follows:

$$\dot{p} = \left(\frac{\sigma_{eq}^{H}(\underline{\sigma}, T)}{K(T, C_{ss}, C_{pp}) \times L(p, T, C_{pp})}\right)^{1/m(T)} \qquad (36)$$

where T is the temperature in Kelvin, σ_{eq}^{H} is the equivalent stress in MPa, m is the strain sensitivity exponent (unitless), K is the strength coefficient in MPa and L is the strain hardening coefficient (unitless). The strength coefficients K depends on the hydrogen concentration (wt.ppm) in solid solution C_{ss} and in solid precipitates C_{pp} while the strain hardening coefficient L is only a function of C_{pp}. The parameters of the model are described in details in Table 6.

Simulations of the hydrogen distribution (dissolved or precipitated) during a NSRR pulse, by considering an instantaneous dissolution mechanism or by using the kinetics term measured by (Lacroix et al., 2018), have shown negligible differences. Therefore, in this viscoplasticity model, hydride nucleation, growth, and dissolution are assumed instantaneous, with hydrogen solubility following Kearns' correlation:

$$TSS = 99000 \exp(-34523/RT) \; [wt.ppm] \qquad (37)$$

where R is the gas constant in J/mol/K and T the temperature in Kelvin. Hydrogen in the cladding is assumed to be constant during simulations, with no diffusion considered. For each computational cell, the split between solid solution and solid precipitates, for a given hydrogen concentration C_{tot}, is given using the following correlations (function of the temperature T in Kelvin):

$$C_{ss}(T) = \min(C_{tot}, TSS(T)) \; [wt.ppm] \qquad (38)$$

$$C_{pp}(T) = \mathrm{C}_{\mathrm{tot}} - C_{ss}(T)[wt.ppm] \qquad (39)$$

Table 6: Cladding mechanical model parameters, from (Le Saux et al., 2015). T is the temperature in Kelvin, Css and Cpp are the hydrogen concentrations in solid solution and in solid precipitates, in wt.ppm.

Strain rate sensitivity exponent m:

$$\boldsymbol{m} = (77.68M_T + 4.11(1 - M_T))^{-1}$$

where $M_T = \left(1 + exp\left(10.2\left(\frac{T}{692} - 1\right)\right)\right)^{-1}$

Strain hardening coefficient L:

$$L = (p + 1 \times 10^{-4})^{n_0} exp(-\alpha_n p\,) + (1 - \exp(\alpha_n p))$$

with $\mathbf{n_0} = (1 + 1.45 \times 10^{-4} C_{pp})[4.86 \times 10^{-2} N_{0T} + 2.35 \times 10^{-2}(1_{N_{0T}})]$

where $\mathbf{N_{0T}} = \frac{1}{1+exp\left(12\left(\frac{T}{810-9.19\times10^{-2}C_{pp}}-1\right)\right)}$

and $\boldsymbol{\alpha}_\mathbf{n} = (53.16 + 1.27 \times 10^{-2} C_{pp})\left(1 + exp\left(11.1\left(\frac{T}{738} - 1\right)\right)\right)$

Strength coefficient K:

$$\mathrm{K} = [1 - 1.175 \times 10^{-4} C_{ss} + (6.15 \times 10^{-5} - 4.38 \times 10^{-8} T) C_{pp}][(1.409 \times 10^9 - 8.952 \times 10^5 T) K_T + 4.05 \times 10^7 (1 - K_T)]$$

where $\mathbf{K_T} = \frac{1}{1+exp\left(1.77\left(\frac{T}{1007}-1\right)\right)}$

Plastic anisotropy coefficients:

$$H_{rr} = \frac{0.485 + 9.5 \times 10^{-2}}{1 + \exp\left(12\left(\frac{T}{740} - 1\right)\right)}$$

$$H_{\theta\theta} = 1 - H_{rr}$$

$$H_{zz} = \frac{0.52 + (-0.23 + 4 \times 10^{-4} T)}{1 + \exp\left(12\left(\frac{T}{550} - 1\right)\right)}$$

$$H_{r\theta} = H_{rz} = H_{\theta z} = 1.5$$

3.2.2 Failure criterion for RIA

To assess clad failure during a RIA, the strain criterion proposed in (Jernkvist et al., 2004) is implemented in OFFBEAT. The model defines a hoop plastic strain threshold for failure, accounting for temperature, strain rate, hydrogen embrittlement, irradiation damage, and zirconia spalling:

$$\varepsilon_{\theta\theta}^{f} = \frac{3S_{spalling}\varepsilon_{\theta\theta}^{0} f_1 f_2 f_3}{f_1 f_2 + f_1 f_3 + f_2 f_3} \qquad (40)$$

where $\varepsilon_{\theta\theta}^{0}$ is the hoop plastic strain at failure of as-fabricated cladding, and f_1, f_2, f_3 are correction factors for strain rate, hydrogen content, and irradiation damage, respectively. The expressions $\varepsilon_{\theta\theta}^{0}$, f_1 and f_2 are given in Table 7. The additional parameters $S_{spalling}$ is a ductility reduction factor for cladding tubes with spalled zirconia.

This failure criterion is relevant for geometries and loading conditions typical of RIA scenarios (i.e., biaxial loading $\sigma_{zz}/\sigma_{\theta\theta} = 1$). Therefore, for the interpretation of out-of-pile experiments such as burst tests, the hoop plastic strain at failure of as-fabricated cladding must be corrected to account for the stress-biaxiality ratio of these experiments that differs from the one of typical of RIA conditions. For normal burst tests where $\sigma_{zz}/\sigma_{\theta\theta} = 0.5$, the hoop plastic strain at failure $\varepsilon_{\theta\theta}^{0}$ must be divided by the following factor

$$C_{R1} = \frac{\underline{\varepsilon_{te}}\left(\frac{\sigma_{zz}}{\sigma_{\theta\theta}} = 1\right)}{\underline{\varepsilon_{te}}\left(\frac{\sigma_{zz}}{\sigma_{\theta\theta}} = 0.5\right)} = 0.456 \qquad (41)$$

with $\underline{\varepsilon_{te}}$ the average hoop total elongation evaluated from the experimental data presented by (Andersson & Wilson, 1979; MAKI & OOYAMA, 1975).

Table 7: Parameters of the failure criterion proposed by (Jernkvist et al., 2004)

Hoop plastic strain at failure for as fabricated cladding tubes (equi-biaxial conditions) :

$$\boldsymbol{\varepsilon_{\theta\theta}^{0}(T) = 2.82 + 1.22 \times 10^{-2}T}\ [\%]$$

f_1 ductility reduction factor (effect of strain rate):

$$\boldsymbol{f_1(\dot{\varepsilon}\,) = \begin{cases} 0.046 - 0.31 \times \log_{10}\dot{\varepsilon}\ \ if\ \dot{\varepsilon} \le 1s^{-1} \\ 0.046\ \ if\ \dot{\varepsilon} > 1s^{-1} \end{cases}}$$

f_2 ductility reduction factor (effect of hydrogen content):

$$\boldsymbol{f_2(C_{pp}, T, \dot{\varepsilon}) = 0.01 + 0.99 \times \exp(-\gamma(T, \dot{\varepsilon})C_{pp})}$$

with $\boldsymbol{C_{pp}}$ the hydrogen concentration in wt.ppm, $\boldsymbol{T}$ the temperature in K and **$\dot{\varepsilon}$ the strain rate in s^{-1}**.

The hydride concentration is given by:

$$\boldsymbol{C_{pp} = \max\left(0, \left(C_{tot} - TSS(T)\right)\right)}$$

with $\boldsymbol{T}$ the temperature in K, $\boldsymbol{C_{tot}}$ the total hydrogen content in wt.ppm and $\boldsymbol{TSS}$ the terminal solubility limit in wt.ppm:

$$\boldsymbol{TSS = 99000\ exp(-34523/RT)}$$

with $\boldsymbol{T}$ the temperature in K, $\boldsymbol{R}$ the gas constant in J/K/mol.

The $\boldsymbol{\gamma}$ function is given by:

$$\boldsymbol{\gamma(T, \dot{\varepsilon}) = 6.52 \cdot 10^{-4} + 2.21 \cdot 10^{-3}(6 + \log_{10}\dot{\varepsilon})\left(1 - tanh\left(\frac{T - T_{transition}}{wf}\right)\right)}$$

with $\boldsymbol{T_{transition}}$ equals to 298 K and $\boldsymbol{wf}$ equals to 8.5.

3.2.3 Hydride rim effect on cladding failure

The failure criterion described above was derived for samples with a uniform hydride distribution and did not account for hydrogen concentration gradients or the presence of a hydride rim. Based on (NAGASE & FUKETA, 2005), it was extended in OFFBEAT to incorporate the effect of rim thickness on cladding strain at failure. In (NAGASE & FUKETA, 2005) burst tests were conducted on hydrogen-charged low-tin Zircaloy-4 cladding tubes. The samples were hydrogenated at 620 K in a hydrogen-argon mixture, producing hydride rims between 100 and 170 µm. Tests were performed at 293 K and 623 K under pressurization rates of 0.002, 0.2, and 2 GPa/s, corresponding to strain rates of 5×10^{-4}, 5×10^{-2} and 0.5 s^{-1}. The study found that:

- At room temperature, increasing hydrogen concentration and pressurization rate reduced the residual hoop strain.
- At 300 wt.ppm hydrogen, the presence of a hydride rim slightly decreased residual strain from 1.33% (without a rim) to 0.5%.
- At 623 K, the impact of the hydride rim was more pronounced: for 600 wt.ppm hydrogen, residual hoop strain dropped from 12% (without a rim) to 0.5% (with a rim structure).

These results show that total hydrogen content, temperature, and strain rate influence mechanical properties, while a dense hydride rim significantly reduces ductility in certain conditions. At low temperatures, the original Jernkvist et al. criterion reasonably matches experimental results, but at 623 K, it fails for hydrogen concentrations above 500 wt.ppm (Figure 16, left).

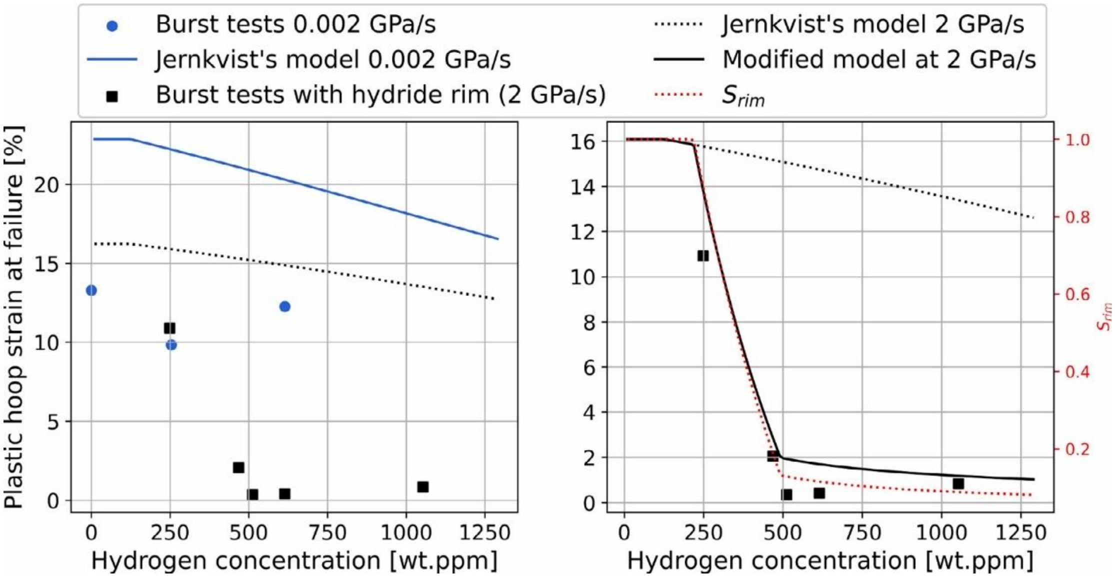

Figure 16: Left: Plastic hoop strain at failure reported by (NAGASE & FUKETA, 2005) for the burst tests conducted at 623 K. The lines plots correspond to the predicted failure strain according to the failure criterion proposed by (Jernkvist et al., 2004). Right: Failure strains from the modified failure criterion for the burst tests that presented a hydride rim. The red dotted line shows a plot of the S_{rim}reduction factor computed with Eqs. (43)(44)(45).

To correct for this effect, a rim reduction factor S_{rim} is introduced in OFFBEAT:

$$S_{rim} = S_0(t_{rim}) \times S_{recovery}(T_{rim}, C_{ss,rim}) \qquad (42)$$

where:

- $S_0(t_{rim})$ accounts for rim embrittlement, decreasing from 1 to 0.05 as hydrogen increases (200–500 wt.ppm).
- $S_{recovery}$ models ductility recovery at high temperatures as a function of rim temperature T_{rim} and hydrogen content $C_{ss,rim}$ in solution.

The S_0 and $S_{recovery}$ functions are reported here:

$$S_0(t_{rim}) = \min\left(\max\left(0.05, \frac{(1-0.05)}{70} \times (t_{rim} - 50)\right), 1\right) \tag{43}$$

$$S_{recovery}(T_{rim}) = S_0 + \frac{C_{ss,rim}}{C_{tot,rim}} \times (1 - S_0) \tag{44}$$

Finally, a correlation is needed to relate the rim thickness to average hydrogen content. In the context of the HERA benchmark, the following empirical correlation was adopted (NAGASE & FUKETA, 2005):

$$t_{rim} = 86.40 \cdot \ln\left(C_{tot,avg}\right) - 415.63\ [\mu m] \tag{45}$$

This equation is specific to the hydrogenation protocol in (NAGASE & FUKETA, 2005), which is similar to that used for HERA samples, and may require adjustments for different experiments. Figure 17 compares the predicted rim thicknesses with Nagase and Fuketa's data and the HERA test matrix.

Failure predictions using this corrected model match experimental burst test data from (NAGASE & FUKETA, 2005), especially for high-hydrogen rimmed samples.

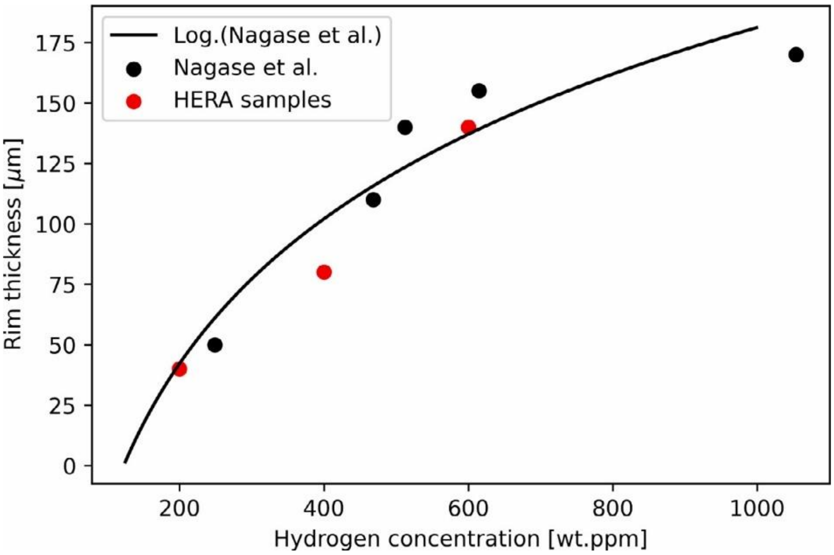

Figure 17: Estimated hydride rim thickness as a function of the mean hydrogen content obtained with Eq. (45), compared with the rim thicknesses of the samples of (NAGASE & FUKETA, 2005) and of the HERA test matrix (Finally, a correlation is needed to relate the rim thickness to average hydrogen content. In the context of the HERA benchmark, the following empirical correlation was adopted (NAGASE & FUKETA, 2005):

$$t_{rim} = 86.40 \cdot \ln\left(C_{tot,avg}\right) - 415.63\ [\mu m] \tag{45}$$

This equation is specific to the hydrogenation protocol in (NAGASE & FUKETA, 2005), which is similar to that used for HERA samples, and may require adjustments for different experiments. Figure 17 compares the predicted rim thicknesses with Nagase and Fuketa’s data and the HERA test matrix.

Failure predictions using this corrected model match experimental burst test data from (NAGASE & FUKETA, 2005), especially for high-hydrogen rimmed samples.

).

3.3 Ongoing developments in implicit contact modeling

The high-fidelity simulation of pellet-cladding mechanical interaction (PCMI) requires robust methodologies to model contact, both between the fuel pellets in the stack and between the fuel and cladding. Various approaches have been developed to enforce contact constraints in computational solid mechanics. The most common formulations used in the Finite Element Method (FEM) community include:

- **Penalty Method**: A straightforward approach in which a force proportional to penetration depth is applied to enforce contact. This method is computationally cheaper than exact constraint enforcement but depends on a penalty parameter. Choosing an excessively high penalty can lead to ill-conditioning of the system matrix, while a low penalty may result in noticeable interpenetration.

- **Lagrange Multiplier Method**: Enforces contact constraints exactly by introducing additional unknowns for each constraint, increasing accuracy compared to the penalty method. However, this approach increases computational cost and can cause convergence issues due to abrupt transitions between contact and separation states. Improper constraint application may also lead to ill-conditioning or singular system matrices.
- **Augmented Lagrange Method**: A combination of the penalty and Lagrange multiplier methods, where the contact force is adjusted iteratively to improve accuracy. This method balances constraint enforcement and numerical stability but requires iterative updates, increasing computational effort.
- **Mortar Method**: A more advanced approach that accurately enforces contact between non-matching meshes using a variational formulation. It improves accuracy for complex contact problems and large deformations. However, it requires more computational effort and is more complex to implement.

3.3.1 Contact handling in OFFBEAT: current status

Since OFFBEAT is based on the FVM rather than the FEM, the boundary conditions for enforcing contact differ somewhat from those used in FEM codes. The original version of OFFBEAT implemented a penalty-based contact method as part of its custom boundary conditions, closely resembling the penalty approach in FEM. While this model performs well for base irradiation simulations, it inherently allows small interpenetrations, which can be problematic for high-fidelity PCMI simulations where minimal penetrations are crucial for accurately predicting cladding expansion and ridge height.

Furthermore, the penalty method is an explicit approach, meaning the contact force depends on the previous iteration's solution and is applied as a source term in the system of equations resulting from the discretization of the governing mechanics equations. This approach makes it difficult to handle multi-body contact scenarios, such as fuel pellet stacks, as the solver struggles to maintain stability without excessive under-relaxation.

To overcome these limitations, an initial version of an implicit contact model was developed, and it is described in (Scolaro et al., 2022). In this formulation, the contact traction discretization is handled semi-implicitly when bodies are in contact, introducing diagonal and off-diagonal coefficients into the system matrix, instead of resulting solely in a source term. This improves stability, particularly in cases involving multiple bodies in contact, and naturally allows for friction modelling while enabling negligible penetration.

3.3.2 Brief overview of the OFFBEAT implicit contact treatment

In OFFBEAT, the traction $\boldsymbol{t_b}$ at the boundary b can be expressed as:

$$\begin{aligned}\boldsymbol{t_b} &= (2\mu_b + \lambda_b)\boldsymbol{n} \cdot \boldsymbol{\nabla u_b} + \boldsymbol{n} \cdot \left(\boldsymbol{\sigma_{exp}}\right)_b \\ &= (2\mu_b + \lambda_b)\frac{\boldsymbol{u_b} - \boldsymbol{u_P}}{\delta_P^n} + \boldsymbol{n} \cdot \left(\boldsymbol{\sigma_{exp}}\right)_b\end{aligned} \tag{46}$$

where μ_b and λ_b are Lame' constants, $\boldsymbol{u}$ is the displacement, δ_P^n is the distance between the cell-center P and the face center b, and $\boldsymbol{\sigma_{exp}}$ is the explicit component of the stress. In the penalty method, the traction $\boldsymbol{t_b}$ is calculated based on interpenetration between two opposing faces (if any) at the previous iteration. Then Eq. (46) is then used to update the normal gradient and face displacement based on the calculated traction for the next iteration of the mechanics solver.

The implicit contact takes a different approach. It moves from the fact that when two faces belonging to separate bodies with cell centers P and N come into contact, the traction $\boldsymbol{t_b}$ must be identical on both faces. Thus, by assuming continuity of traction and enforcing identical incremental displacements (since the faces are in contact), the following discretization is obtained (the detailed derivation is not shown):

$$\boldsymbol{t_b} = \overline{(2\mu_b + \lambda_b)} \cdot \frac{\boldsymbol{u_N} - \boldsymbol{u_P}}{\delta^n} + \overline{(2\mu_b + \lambda_b)}\, \boldsymbol{n} \cdot \overline{\boldsymbol{\sigma^b_{exp}}} \tag{47}$$

where $\delta = \delta_P + \delta_N$ is the sum of the two cell-center to face center vectors, $\overline{\left(2\mu_b + \lambda_b\right)}$ is the *harmonically* interpolated stiffness coefficient at the contact face, and $\overline{\boldsymbol{\sigma^b_{exp}}}$ is the *reverse linear* interpolated explicit component at the face. A correction for the initial gap between two faces is included in the explicit term to account for the fact that cells do not initially coincide.

In summary, this approach leads to a formulation of the contact stress that is a function of the displacement solution on the two contacting cells. Indeed, besides the use of specific interpolation algorithms for the stiffness and explicit components, Eq. 55 closely resembles the traction at any internal face within the domain. The new discretization no longer results in a single explicit source term but is split into an implicit component, adding diagonal and off-diagonal coefficients to the system matrix, and an explicit source component.

It should be noted that Eq. 55 is written for the total traction; however, in the code, the traction is split into normal and tangential components, as the amount of transmitted tangential component depends on the friction coefficient, which is typically a user-defined parameter.

3.3.3 Planned extensions for implicit contact algorithm

The original implementation in (Scolaro et al., 2022) relied on a blending coefficient function to transition between open and closed gap states but setting appropriate contact parameters proved challenging. Also, the method proved robust only for bodies starting already in contact (like in a punch test, or the pellets in a fuel column) while the alternation between open and closed gap states (as for the fuel and the cladding) often led to numerical difficulties.

To address this, EPFL plans to refine the original implicit contact algorithm in Task 4.2, eliminating the need for a blending coefficient. Instead, the full contact discretization of Eq. 55 will be directly applied gradually growing the contact stiffness $\overline{\left(2\mu_b + \lambda_b\right)}$ until a certain user defined penetration threshold is reached. A relaxation factor will be used for this purpose, ensuring a smooth transition from the open gap condition to contact. This simplification reduces the number of parameters to be set, requiring only a relaxation factor and a threshold penetration value. The use of a low penetration threshold will enable penetration levels that are nearly zero or, in any case, negligible compared to the mesh size. Minimizing pellet-to-cladding penetration through these improvements will significantly enhance OFFBEAT's predictive capabilities for ridging and PCMI simulations.

Furthermore, in the previous implementation described in (Scolaro et al., 2022), the friction component of the force was handled fully explicitly. In the planned extensions, it will be implicitly incorporated alongside the normal component, enhancing both stability and accuracy. This improvement will enable a more accurate representation of the frictional stress components in the hoop direction arising in PCMI, as well as the cladding's axial elongation.

3.4 3D gap conductance modelling

A limitation of modern high-fidelity fuel performance codes is that they still often rely on simplified correlations or models that were originally developed for traditional 1.5D codes. This is true for the gap conductance model for instance, where the heat is assumed to pass radially (1D) from the fuel to the clad through three parallel thermal resistances, one for conduction through the gas, one for radiative heat transfer, one for contact conduction when the gap is closed. This assumption remains reasonable during base irradiation, as the fuel-to-cladding gap is much smaller than the characteristic radial dimension of the fuel rod, and the temperature gradient is predominantly radial. However, it becomes questionable in LOCA scenarios, particularly when the cladding ballons significantly and the temperature of the rod increases considerably, increasing the relative importance of the radiative heat transfer component. In such cases, a purely 1D conductance model may no longer accurately represent the thermal response, and understanding the magnitude of the error introduced by this assumption might be of interest for advanced codes.

Additionally, an open challenge exists regarding heat conservation as the gap widens. Traditional gap conductance models assume direct heat flux transfer between fuel and cladding axial slices, but when the surfaces move apart significantly, the spatial mapping of heat transfer may become problematic. In OFFBEAT, for instance, the standard Arbitrary Mesh Interface (AMI) method in OpenFOAM - designed for cases where surfaces remain relatively close and overlapping - may introduce errors in heat flux conservation when applied to surfaces separated by a large gap.

To address these concerns, EPFL has investigated in Task 4.2 the feasibility of developing a 3D gap conductance model in which the gap is explicitly meshed, allowing for a more physically representative heat transfer simulation. This will include:

- Modeling gas conduction and/or convection through the gap using a finite-volume discretization.
- Simulating radiative heat transfer using view factors, which are already available within OpenFOAM's thermal radiation framework.

3.4.1 Radiation modeling and view factors in OpenFOAM

OpenFOAM provides several radiation modeling capabilities, including the P1 model, the Finite Volume Discrete Ordinates Method (fvDOM), and other approaches designed for participating media. However, for wide-gap heat transfer scenarios, the view factor model is likely the most suitable choice, as absorption, emission, and scattering of radiation in the gas itself can most probably be neglected.

In OpenFOAM, the view factor model computes radiative heat exchange by generating rays between surface faces using the *viewFactorsGen* utility. Energy transfer is then determined by summing contributions along these rays, ensuring that only directly visible surfaces interact thermally. This method is particularly effective for complex geometries where some surfaces may be shielded from radiation.

The identified plan is to implement view factor-based radiation combined with conduction in the meshed gap. This approach will provide a more physically representative heat transfer model and allow an assessment of whether additional refinements are necessary.

3.4.2 Potential challenges

While a 3D gap conductance model could provide a more accurate representation of heat transfer in LOCA scenarios, several technical challenges must be addressed. One key question is how to handle the additional mesh - whether to introduce a separate thermal-only region (i.e. without mechanical solution in this region) or to explore OpenFOAM's dynamic meshing capabilities for automatic gap detection and refinement of the gap mesh. Initially, the simplest approach would be to model the gap as an additional thermal region between a smeared fuel column and the cladding, applying the radiative heat transfer model to the two opposing surfaces.

The applicability of this 3D approach to normal irradiation conditions is uncertain as during steady-state the gap remains thin, and 1D heat conductance models are usually sufficient. However, a 3D modeling of the gap heat transfer may be beneficial in asymmetry cases such as missing pellet surface (MPS) defects or eccentric pellets, where the gap size on one side of the pellet might be non-negligible. Nevertheless, even if this method proves impractical for routine fuel performance calculations, it will provide valuable insights into the limitations of 1D gap models under extreme conditions.

3.5 References

Andersson, T., & Wilson, A. (1979). Ductility of Zircaloy Canning Tubes in Relation to Stress Ratio in Biaxial Testing. In *Zirconium in the Nuclear Industry* (pp. 60–71). ASTM International100 Barr Harbor Drive, PO Box C700, West Conshohocken, PA 19428-2959. https://doi.org/10.1520/STP36672S

Brunetto, E. L., Scolaro, A., Fiorina, C., & Pautz, A. (2021). First Steps towards Large Strain Analysis in OFFBEAT. *ANS Winter Meeting 2021*. https://doi.org/doi.org/10.13182/T125-36858

Cardiff, P., Tuković, Jaeger, P. De, Clancy, M., & Ivanković, A. (2017). A Lagrangian cell-centred finite volume method for metal forming simulation. *International Journal for Numerical Methods in Engineering*, *109*(13), 1777–1803. https://doi.org/10.1002/NME.5345

Erbacher, F. J., Neitzel, H. J., Rosinger, H., Schmidt, H., & Wiehr, K. (1982a). Burst criterion of Zircaloy fuel claddings in a loss-of-coolant accident. *Zirconium in the Nuclear Industry, Fifth Conference, ASTM STP 754, D.G. Franklin Ed.*, 271–283.

Erbacher, F. J., Neitzel, H. J., Rosinger, H., Schmidt, H., & Wiehr, K. (1982b). Burst criterion of Zircaloy fuel claddings in a loss-of-coolant accident. *Zirconium in the Nuclear Industry, Fifth Conference*.

Forgeron, T., Brachet, J. C., Barcelo, F., Castaing, A., Hivroz, J., Mardon, J. P., & Bernaudat, C. (2000). Experiment and modeling of advanced fuel rod cladding behavior under LOCA conditions: Alpha-beta phase transformation kinetics and EDGAR methodology. *ASTM Special Technical Publication*, *1354*. https://doi.org/10.1520/stp14303s

Idaho National Laboratory. (n.d.). *Source Documentation | BISON*. Retrieved July 27, 2022, from https://mooseframework.inl.gov/bison/source/

Jernkvist, L. O., Massih, A. R., & Rudling, P. (2004). A Strain-based Clad Failure Criterion for Reactivity Initiated Accidents in Light Water Reactors. *Swedish Nuclear Power Inspectorate, Stockholm (Sweden)*.

Lacroix, E., Motta, A. T., & Almer, J. D. (2018). Experimental determination of zirconium hydride precipitation and dissolution in zirconium alloy. *Journal of Nuclear Materials*, *509*, 162–167. https://doi.org/10.1016/j.jnucmat.2018.06.038

Le Saux, M., Besson, J., & Carassou, S. (2015). A model to describe the mechanical behavior and the ductile failure of hydrided Zircaloy-4 fuel claddings between 25 °C and 480 °C. *Journal of Nuclear Materials*, *466*, 43–55. https://doi.org/10.1016/j.jnucmat.2015.07.026

Limbäck, M., & Andersson, T. (1996). A model for analysis of the effect of final annealing on the in- and out-of-reactor creep behavior of zircaloy cladding. *ASTM Special Technical Publication*, *1295*, 448–468. https://doi.org/10.1520/stp16185s

MAKI, H., & OOYAMA, M. (1975). Plastic Deformation and Fracture Behavior of Zircaloy-2 Fuel Cladding Tubes under Biaxial Stress. *Journal of Nuclear Science and Technology*, *12*(7), 423–435. https://doi.org/10.1080/18811248.1975.9733131

Markiewicz, M. E., & Erbacher, F. J. (1988). *Experiments on ballooning in pressurized and transiently heated Zircaloy-4 tubes* (Issue KfK 4343).

Massih, A. R. (2009). Transformation kinetics of zirconium alloys under non-isothermal conditions. *Journal of Nuclear Materials*, *384*(3), 330–335. https://doi.org/10.1016/J.JNUCMAT.2008.11.033

NAGASE, F., & FUKETA, T. (2005). Investigation of Hydride Rim Effect on Failure of Zircaloy-4 Cladding with Tube Burst Test. *Journal of Nuclear Science and Technology*, *42*(1), 58–65. https://doi.org/10.1080/18811248.2005.9726364

Pastore, G., Williamson, R. L., Gardner, R. J., Novascone, S. R., Tompkins, J. B., Gamble, K. A., & Hales, J. D. (2021). Analysis of fuel rod behavior during loss-of-coolant accidents using the BISON code: Cladding modeling developments and simulation of separate-effects experiments. *Journal of Nuclear Materials*, *543*. https://doi.org/10.1016/J.JNUCMAT.2020.152537

Reymond, M., Sercombe, J., & Scolaro, A. (2024). Investigation of the PCMI failure of pre-hydrided Zy-4 cladding during Reactivity Initiated Accidents with ALCYONE and OFFBEAT fuel performance codes. *Nuclear Engineering and Design*, *427*, 113430. https://doi.org/10.1016/j.nucengdes.2024.113430

Scolaro, A., Fiorina, C., Clifford, I., & Pautz, A. (2022). Development of a semi-implicit contact methodology for finite volume stress solvers. *International Journal for Numerical Methods in Engineering*, *123*(2), 309–338. https://doi.org/10.1002/nme.6857

4. Review and selection of models for cladding oxidation and hydrogen transport in OFFBEAT

At PSI, a thorough state-of-the art review of the models for multi-dimensional macroscopic fuel behaviour analysis was carried out (see Appendix A). The review focused on the models implemented in various multi-dimensional codes around the world, with the aim of identifying the models that can be implemented in OFFBEAT for a comprehensive fuel performance analysis. The codes that were reviewed included ALCYONE from CEA, BISON from INL, DIONISIO from CNEA, and Falcon from EPRI (reference fuel behaviour analysis code used at PSI). The review of the models associated with the fuel, gap and cladding related phenomena was done. A non-exhaustive list of the models available/used in BISON, ALCYONE, and Falcon, based on the review, are presented in Tables 1, 2 and 3, respectively.

Table 8: Models used/available in BISON.

	Physical property	**Models used/available**
Fuel related models	Thermal conductivity	MATPRO; NFIR
	Solid swelling	MATPRO
	Fuel Densification	ESCORE
	Fuel Cracking & Relocation	Smeared cracking; ESCORE
	UO_2 Creep	MATPRO (FCREEP)
	Radial power profile	Soba et al. (DIONISIO)
Gap related models	Gap heat transfer	Ross and Stoute, MATPRO
	Gap contact	Heinstein and Laursen
	Fission gas release	Forsberg–Massih; Pastore
Cladding related	Irradiation Growth	ESCORE; Franklin
	Zr Creep	Limbäck and Andersson
	Oxidation (Normal operating temperature)	EPRI/KWU/CE PFCC EPRI/SLI
	Oxidation (High temperature)	Leistikow; Cathcart Schanz; Prater-Courtright

Table 9: Models used/available in ALCYONE.

	Physical property	**Models used/available**
Fuel properties	Thermal conductivity	Modified Lucuta's formulation
	Thermal expansion	Martin
	Fuel Densification, Solid swelling	MATPRO
	Fuel Cracking & Relocation	Smeared cracking
	UO_2 Creep	Monerie & Gatt
	Radial power profile	PRODHEL
Gap properties	Gap heat transfer	URGAP
	Gap contact	Coulomb's friction law
	Fission gas release	MARGARET, CARACAS
Cladding properties	Thermal conductivity	MATPRO
	Zr Creep	Hill's criterion

Table 10: Models used/available in Falcon.

	Physical property	**Models used/available**
Fuel related	Thermal conductivity	MATPRO v11; NFIR
	Specific heat capacity	MATPRO
	Solid swelling	Literature
	Thermal expansion	MATPRO
	Fuel Densification	MATPRO v11; ESCORE
	Fuel Cracking & Relocation	Isotropic cracking ESCORE; HEDL
	UO_2 Creep	MATPRO
	Radial power profile	RADAR-G; TUBRNP
Gap related	Gap heat transfer	Ross & Stoute (Open) Modified Mikic & Todreas (Closed)
	Fission gas release	ANS-5.4; Forsberg-Massih; ESCORE; EPRI/CE
Cladding related	Thermal conductivity	MATPRO v11
	Specific heat capacity	MATPRO
	Thermal expansion	MATPRO
	Zr Creep (Low temperature)	MATPRO v11; ESCORE; MATPRO; Limbäck and Andersson
	Zr Creep (High temperature)	MATPRO v11
	Zr Irradiation Growth	MATPRO v11; ESCORE; Franklin
	Zr Plasticity	MATPRO v11
	Oxidation (Low temperature)	MATPRO v11 (CORROS); PFCC EPRI/SLI
	Oxidation (High temperature),	MATPRO v11 (COXIDE); Literature
	Zr phase transformation	MATPRO v11

A more detailed review along with the references can be found in Appendix A. The available models in OFFBEAT at the time of the review are presented in Table 4. Since OFFBEAT is currently being developed, newer models are incorporated from time to time and thus, this list is non-exhaustive.

Table 11: Models used/available in OFFBEAT.

	Physical property	**Models used/available**
Fuel related	Thermal conductivity	MATPRO (FTHCON); NFIR
	Specific heat capacity	MATPRO v11
	Solid swelling	MATPRO (FSWELL)
	Thermal expansion	MATPRO v11
	Fuel Densification	MATPRO (FUDENS)
	Fuel Cracking & Relocation	Isotropic cracking FRAPCON4.0
	UO_2 Creep	MATPRO (FCREEP)
	Radial power profile	TUBRNP
Gap related	Gap heat transfer	FRAPCON4.0
	Gap contact	Cardiff; Scolaro
	Fission gas release	Forsberg-Massih; SCIANTIX
Cladding related	Thermal conductivity	MATPRO (CTHCON)
	Specific heat capacity	IAEA-TECDOC-1496
	Thermal expansion	MATPRO (CTHEXP)
	Zr Creep	Limbäck and Andersson
	Zr Irradiation Growth	ESCORE, MATPRO v11
	Zr Plasticity	Von Mises
	Oxidation (Normal operating temperature)	EPRI/KWU/CE
	Oxidation (High temperature)	Leistikow; Schanz; Prater-Courtright

Based on the review, some phenomena have been identified to be incorporated into OFFBEAT. These include models for cladding oxidation, hydrogen transport and uptake, hydride precipitation, dissolution and reorientation, and models for liner claddings. The models for these phenomena are presented in brief here:

4.1 Cladding oxidation

The zirconium cladding oxidation models in OFFBEAT are categorized into two temperature regimes: normal operation between 523 K and 673 K, and a higher temperature regime up to 1900 K.

Currently, the EPRI/KWU/C-E oxidation model [37] [38] is used for normal operating temperatures below 673 K. BISON and Falcon fuel behaviour codes have the EPRI SLI Model [39] as another model for normal operating temperatures. It uses enhanced model parameters by considering factors that are a function of coolant lithium content, alloy tin and iron content, hydrogen content, and fast flux. The EPRI SLI Model can be added as an option to choose for normal operating temperature regime oxidation in OFFBEAT.

For the high temperature range, similar to as in BISON, the Leistikow correlation [40] is used for temperatures from 673 K up to 1800 K. For temperatures between 1800 K and 1900 K, a linear interpolation between two correlations is made using the procedure from Schanz [41]. For temperatures above 1900 K, the Prater-Courtright correlation [42] is used. The Cathcart-Pawel correlation [43] is also available in BISON and Falcon fuel behaviour codes and can be added as an option to choose from for the high temperature cladding oxidation in OFFBEAT. Moreover, currently OFFBEAT does not make a distinction between Zr-2 and Zr-4 cladding types and the correlations are different for different cladding types. The option to select different types of cladding can be added to OFFBEAT and the corresponding oxidation correlations can then be used.

4.2 Hydrogen transport and uptake

Currently, hydrogen transport behaviour in the claddings is not modelled in OFFBEAT. The hydrogen that enters the cladding due to waterside corrosion can respond relatively quickly to established driving forces which can drive a hydrogen flux to regions of the solid. The hydrogen flux is due to the combined effects of Fick's law of diffusion, the Soret effect and stress gradients [44] as:

$$J = D_H \left(\nabla C_{ss} + \frac{C_{ss} Q^*}{RT^2} \nabla T - \frac{C_{ss} V_H}{RT} \nabla \sigma_H \right) \tag{48}$$

where J is the hydrogen flux in mol/m^2/s, D_H is the diffusion coefficient in m^2/s, C_{ss} is the hydrogen concentration in solid solution in wppm, Q* is the heat of transport in J/mol, R is the gas constant in J/K/mol, T is the temperature in K, V_H is the partial molar volume of hydrogen in zircaloy in m^3/mol and σ_H is the hydrostatic stress in Pa.

Most existing codes that model hydrogen transport, often neglect the stress-driven diffusion term. However, the impact of stress-driven diffusion becomes important, especially during dry storage of spent nuclear fuel. The hydrogen transport in the cladding will be modelled in OFFBEAT using the hydrogen flux. Furthermore, the models for hydrogen pickup are different for the different types of claddings. For now, as OFFBEAT has only Zr-4 cladding material properties, the hydrogen uptake will be considered as a user-specified fixed instantaneous hydrogen pickup fraction, so that the average total concentration of hydrogen including dissolved hydrogen and hydrogen as Zr-hydride in the cladding, which is roughly proportional to the thickness of the oxide layer, can be determined. In the next steps, as material properties for other claddings like Zr-2, would be implemented in OFFBEAT, the hydrogen pickup models for BWRs using either the concentration of hydrogen calculated as a function of local axial burnup, or the hydrogen flux based on the linear heat rate or linear power will be used.

4.3 Hydride precipitation and dissolution

To model the dissolution and precipitation of hydrides, the Hydrogen Nucleation Growth and Dissolution (HNGD) model [45], as implemented in BISON, is being incorporated into OFFBEAT. The hydrides dissolve or precipitate (by nucleation and growth) depending on the solubility (TSSD) or super-solubility (TSSP) limits. The dissolution of hydrides occurs according to the equation:

$$\frac{\partial C_{ss}}{\partial t} = -K_D (C_{ss} - TSSD) \qquad (C_{ss} < TSSD \;\&\; C_{pp} > 0) \tag{49}$$

Hydrides are formed by nucleation according to the equation:

$$\frac{\partial C_{ss}}{\partial t} = -K_N (C_{ss} - TSSP) \qquad (C_{ss} \geq TSSP) \tag{50}$$

Hydrides are formed by growth in the hysteresis region according to the equation:

$$\frac{\partial C_{ss}}{\partial t} = -K_G (C_{tot} - TSSD) p (1 - x)(-\ln(1 - x))^{1 - \frac{1}{p}} \qquad \left(TSSD < C_{ss} < TSSP \;\&\; C_{pp} > 0\right) \tag{51}$$

$$x = \frac{C_{tot}}{C_{tot} - TSSD}$$

where K_D, K_N and K_G are the kinetic coefficients for dissolution, nucleation, and growth, respectively, and p is a model parameter. These equations are being implemented in OFFBEAT for the precipitation and dissolution of hydrides.

4.4 Hydride reorientation

The fraction of radial hydrides and the reorientation of hydrides is being modelled in OFFBEAT by utilizing the model by Desquines et al. [46]. The precipitation of radial hydrides depends on the temperature, stress, and hydrogen concentration. The hoop stress limits for radial hydride precipitation as obtained in [46] will be used in OFFBEAT. According to the model, 100% of the hydrides are radial if the hoop stress reaches:

$$\sigma_\theta^{100\%} = 110 + 65\left[1 - exp(-\frac{C_{tot}}{65})\right] \mp 20 \quad [MPa] \tag{52}$$

and the threshold for radial orientation is:

$$\sigma_\theta^{0\%} = 0.02C_{tot} - 0.3862(min[T, TSSD]) + 186.9 \quad [MPa] \tag{53}$$

Then the fraction of radial hydrides can be determined as:

$$f_r = \frac{\sigma_\theta - \sigma_\theta^{0\%}}{\sigma_\theta^{100\%} - \sigma_\theta^{0\%}} \qquad (\sigma_\theta^{0\%} \leq \sigma_\theta \leq \sigma_\theta^{100\%}) \tag{54}$$

Another model for hydride reorientation proposed by Cinbiz et al. [47] can be included in OFFBEAT. The orientation depends on the biaxial stress and temperature gradient in the cladding.

4.5 Liner claddings

While the conventional claddings comprise a homogeneous zirconium alloy, the liner claddings consist of two layers, a thick substrate providing the mechanical strength of the cladding and a thin liner with chemical composition designed to influence hydrogen distribution within the cladding. These liner claddings are characterized by a different hydrogen behavior compared to non-liner claddings. The difference in the hydrogen solubility in the substrate and liner drive hydrogen towards the substrate-liner interface. The limits for dissolution and precipitation are referred as the terminal solid solubility for dissolution (TSSD) and precipitation (TSSP), respectively.

The different models for TSSP and TSSD for the substrate and the liner will be implemented in OFFBEAT. For the inner liner claddings, the substrate is Zr-2 and the coefficients for TSSD and TSSP from the work of Une et al. [48] have been adopted. For the liner, due to unavailability of solubilities for each material, pure Zirconium coefficients from Une et al. [48] will be implemented in OFFBEAT.
For the outer liner claddings, the substrate is Zr-4, and several correlations are available in literature, one among which is from Kammenzind [49]. However, the data for hydrogen solubility in the liner material has not been measured. Following the work of Gong et al. [50], the TSSD and TSSP for the liner can be expressed in terms of the TSSD and TSSP of the substrate and the chemical potential difference between the liner and the substrate. The correlations for the TSSD and TSSP for the substrate and liner in the outer and inner liner claddings are presented in Table 5.

Table 12: TSSD and TSSP correlations for the outer and inner liner claddings.

Cladding Type	Region	TSSD (wppm)	TSSP (wppm)
Outer Liner	Substrate	$6.6 \times 10^4 \exp\left(\frac{-32144}{RT}\right)$	$3.1 \times 10^4 \exp\left(\frac{-25239}{RT}\right)$
	Liner	$TSS_{D/P}^{substrate} \times \exp\left(\frac{-656}{RT}\right)$	
Inner Liner	Substrate	$1.43 \times 10^5 \exp\left(\frac{-36686}{RT}\right)$	$3.27 \times 10^4 \exp\left(\frac{-25042}{RT}\right)$
	Liner	$1.41 \times 10^5 \exp\left(\frac{-38104}{RT}\right)$	$3.39 \times 10^4 \exp\left(\frac{-27291}{RT}\right)$

4.5.1 Material models for liner claddings

As was mentioned for the cladding oxidation as well as hydrogen pickup models, the need to have the material properties of the different claddings like Zr-4 or Zr-2 is important as the correlations vary according to the cladding type. This becomes even more significant for the liner claddings, which have different materials (or different chemical compositions for the same alloy) for the substrate and liner. Currently, OFFBEAT has the material models (for claddings) only for Zr-4, which is the typical cladding material for PWRs. The BWRs use Zr-2 claddings. Then the liner claddings use different compositions of zirconium alloys. As was noted for the liner claddings, the hydrogen diffusion is strongly influenced by its solubility in the liner and the substrate. Having the correct models for these materials would ensure more accurate results using OFFBEAT. So, apart from the Zr-4 (for PWRs), the material models for Zr-2 (BWRs), pure Zirconium (outer liner), and Cr-coated claddings, looking forward towards ATFs, are needed in OFFBEAT and will be implemented depending on the availability of these material properties.

4.6 Failure Criteria for DHC and Embrittlement

Following the implementations in HYPE [51], the failure criteria for delayed hydride cracking (DHC) and embrittlement will be incorporated into OFFBEAT. For the DHC modelling, the stress intensity is calculated and compared with the stress intensity threshold for DHC onset. The stress intensity threshold can be modelled using either the models from Shi and Puls [52] or from Aliev and Kolesnik [53]. The stress intensity factor can be calculated using the equation:

$$K_I = F\sigma_\theta\sqrt{\pi a} \quad \left[MPa\sqrt{m}\right] \qquad with\ F = \sqrt{1.2/Q} \tag{55}$$

where a is the user-defined pre-existing crack size and Q = 1.5 is the shape factor.

For the radial hydride induced embrittlement, the degree of embrittlement depends on the continuity of radial hydrides. A factor called Radial Hydride Continuity Factor (RHCF) has been defined by Billone et al. [54] which can be used to determine the Ductile to Brittle Transition Temperatures (DBTT) using the correlation:

$$DBBT_{Best\ Estimate} = \left(34.05\sqrt{0.9RHCF} - 73.83\right) + 273.15\ [K] \tag{56}$$

The parameter RHCF cannot be obtained with HYPE. Instead, the tool calculates the fraction of the cladding thickness in which radial hydrides occur. This is based on a conservative assumption of the perfect continuity of radial hydrides. The implementation for the failure criteria for DHC and Embrittlement based on the described models will be carried out in OFFBEAT.

5. Conclusive remarks

The advancements made by POLIMI, EPFL, and PSI within Task 4.2 contribute to identify and develop to the development of accurate models for nuclear fuel behaviour, addressing key challenges in fuel performance and safety analysis.

POLIMI work focused on enhancing SCIANTIX with novel physics-based models for high-burnup structures, chromia-doped fuels, and athermal fission gas release. The developments provided a robust framework for understanding and predicting the behaviour of fission gases, porosity evolution, and microstructural changes in these systems. By leveraging advanced numerical techniques and neural networks, POLIMI ensured that the implemented models were computationally efficient and compatible with coupled thermo-mechanical simulations in the SCIANTIX and OFFBEAT codes.

EPFL contributed by supporting the review of physical models and developing advanced modelling including large strain for clad ballooning, implicit contact for pellet-cladding mechanical interaction and 3D methodologies for gap conductance. The implementation of a view-factor approach for radiative heat transfer further improves the accuracy of heat transfer modelling in multidimensional simulations, enhancing the predictive capabilities of the fuel performance codes.

PSI efforts were directed towards the development of models for cladding oxidation, hydrogen transport, and geometric imperfections. These contributions address critical aspects of cladding behaviour, ensuring a more comprehensive description of the fuel-cladding-gap system. The extensive review of state-of-the-art multidimensional codes provided valuable insights into model selection and integration, further strengthening the foundation of OFFBEAT for advanced simulations.

6. References

[1] C. Walker, T. Kameyama, S. Kitajima and M. Kinoshita, “Concerning the microstructure changes that occur at the surface of UO2 pellets on irradiation to high burnup,” *Nuclear Materials for Fission Reactors,* pp. 73-79, 1992.

[2] M. Cunningham, M. Freshley and D. Lanning, “Development and characteristics of the rim region in high burnup UO2 fuel pellets,” *Journal of Nuclear Materials,* pp. 19-27, 1992.

[3] G. Khvostov, V. Novikov, A. Medvedev and S. Bogatyr, “Approaches to Modeling of High Burn-up Structure and Analysis of its Effects on the Behaviour of Light Water Reactor Fuels in the START-3 Fuel Performance Code,” in *Water Reactor Fuel Performance Meeting*, Kyoto, Japan, 2005.

[4] M. S. Veshchunov and V. E. Shestak, “Model for evolution of crystal defects in UO2 under irradiation up to high burn-ups,” *Journal of Nuclear Materials,* vol. 384, no. 1, pp. 12-18, 2009.

[5] T. Wiss, V. V. Rondinella, R. J. M. Konings, D. Staicu, D. Papaioannou, S. Bremier, P. Pöml, O. Benes, J. Y. Colle, P. V. Uffelen, A. Schubert, F. Cappia, M. Marchetti, D. Pizzocri, F. Jatuff, W. Goll, T. Sonoda, A. Sasahara, S. Kitajima and M. Kinoshita, “Properties of the high burnup structure in nuclear light water reactor fuel,” *Radiochimica Acta,* vol. 105, no. 11, pp. 893-906, 2017.

[6] J. Rest, M. W. D. Cooper, J. Spino, J. A. Turnbull, P. Van Uffelen and C. T. Walker, “Fission gas release from UO2 nuclear fuel: A review,” *Journal of Nuclear Materials,* vol. 513, pp. 310-345, 2019.

[7] T. Barani, D. Pizzocri, F. Cappia, L. Luzzi, G. Pastore and P. Van Uffelen, “Modeling high burnup structure in oxide fuels for application to fuel performance codes. Part I: High burnup structure formation,” *Journal of Nuclear Materials,* vol. 539, p. 152296, 2020.

[8] T. Barani, D. Pizzocri, F. Cappia, G. Pastore, L. Luzzi and P. Van Uffelen, “Modeling high burnup structure in oxide fuels for application to fuel performance codes. Part II: Porosity evolution,” *Journal of Nuclear Materials,* vol. 563, p. 153627, 2022.

[9] F. Cappia, K. Wright, D. Frazer, K. Bawane, B. Kombaiah, W. Williams, S. Finkeldei, F. Teng, J. Giglio, M. N. Cinbiz, B. Hilton, J. Strumpell, R. Daum, K. Yueh, C. Jensen and D. Wachs, “Detailed characterization of a PWR fuel rod at high burnup in support of LOCA testing,” *Journal of Nuclear Materials,* vol. 569, p. 153881, 2022.

[10] K. Lassman, C. Walker, J. Van De Laar and F. Lindström, “Modelling the high burnup UO2 structure in LWR fuel,” *Journal of Nuclear Materials,* vol. 226, pp. 1-8, 1995.

[11] M. Lemes, A. Soba and A. Denis, “An empirical formulation to describe the evolution of the high burnup structure,” *Journal of Nuclear Materials,* vol. 496, pp. 174-181, 2014.

[12] D. Pizzocri, F. Cappia, L. Luzzi, G. Pastore, V. V. Rondinella and P. Van Uffelen, “A semi-empirical model for the formation and depletion of the high burnup structure in UO2,” *Journal of Nuclear Materials,* vol. 487, pp. 23-29, 2017.

[13] C. T. Walker, “Assessment of the radial extent and completion of recrystallisation in high burn-up UO2 nuclear fuel by EPMA,” *Journal of Nuclear Materials,* vol. 276, pp. 56-62, 1999.

[14] G. Zullo, A. Scolaro, T. Barani and D. Pizzocri, “Two-phase modelling for fission gas sweeping in restructuring nuclear oxide fuel,” *Nuclear Engineering and Design,* vol. 429, p. 113602, 2024.

[15] G. Zullo, P. D. and L. Luzzi, “The SCIANTIX code for fission gas behaviour: Status, upgrades, separate-effect validation, and future developments,” *Journal of Nuclear Materials,* vol. 587, p. 154744, 2023.

[16] G. Pastore, L. Luzzi, V. Di Marcello and P. Van Uffelen, “Physics-based modelling of fission gas swelling and release in UO2 applied to integral fuel rod analysis,” *Nuclear Engineering and Design,* vol. 256, pp. 75-86, 2013.

[17] J. A. Turnbull, R. J. White and C. Wise, “The diffusion coefficient for fission gas atoms in uranium dioxide,” *(IWGFPT–32). International Atomic Energy Agency (IAEA),* 1989.

[18] F. S. Ham, “Theory of diffusion-limited precipitation,” *Journal of Physics and Chemistry of Solids,* vol. 6, no. 4, pp. 335-351, 1958.

[19] D. R. Olander and D. Wongsawaeng, “Re-solution of fission gas - A review: Part I. Intragranular bubbles,” *Journal of Nuclear Materials,* vol. 354, no. 1-3, pp. 94-109, 2006.

[20] M. S. Veshchunov, V. D. Ozrin, V. E. Shestak, V. I. Tarasov, R. Dubourg and G. Nicaise, “Development of the mechanistic code MFPR for modelling fission-product release from irradiated UO2 fuel,” *Nuclear Engineering and Design,* vol. 236, no. 2, pp. 179-200, 2006.

[21] M. Piro, D. Sunderland, S. Livingstone, J. Sercombe, W. Revie, A. Quastel, K. Terrani and C. Judge, A Review of Pellet–Clad Interaction Behavior in Zirconium Alloy Fuel Cladding, 2017.

[22] C. Nonon, J. C. Menard, S. Lansiart, J. Noirot, S. Martin, G. M. Decroix, O. Rabouille, C. Delafoy and B. Petitprez, PCI behaviour of chromium oxide-doped fuel, Organisation for Economic Co-Operation and Development - Nuclear Energy Agency, 2025.

[23] C. Riglet-Martial, P. Martin, D. Testemale, C. Sabathier-Devals, G. Carlot, P. Matheron, X. Iltis, U. Pasquet, C. Valot, C. Delafoy and R. Largenton, “Thermodynamics of chromium in UO2 fuel: A solubility model,” *Journal of Nuclear Materials,* vol. 447, no. 1-3, pp. 63-72, 2014.

[24] C. Riglet-Martial, J. Sercombe, J. Lamontagne, J. Noirot, I. Roure, T. Blay and L. Desgranges, “Experimental evidence of oxygen thermo-migration in PWR UO2 fuels during power ramps using in-situ oxido-reduction indicators,” *Journal of Nuclear Materials,* vol. 480, pp. 32-39, 2016.

[25] E. Curti and D. A. Kulik, “Oxygen potential calculations for conventional and Cr-doped UO2 fuels based on solid solution thermodynamics,” *Journal of Nuclear Materials,* vol. 534, p. 152140, 2020.

[26] G. L. Murphy, R. Gericke, S. Gilson, E. F. Bazarkina, A. Rossberg, P. Kaden, R. Thümmler, M. Klinkenberg, M. Henkes, P. Kegler, V. Svitlyk, J. Marquardt, T. Lender, C. Hennig, K. O. Kvashnina and N. Huittinen, “Deconvoluting Cr states in Cr-doped UO2 nuclear fuels via bulk and single crystal spectroscopic studies,” *Nature Communications 2023 14:1,* vol. 14, no. 1, pp. 1-11, 2023.

[27] G. Nicodemo, G. Zullo, F. Cappia, P. Van Uffelen, A. De Lara, L. Luzzi and D. Pizzocri, “Chromia-doped UO2 fuel: An engineering model for chromium solubility and fission gas diffusivity,” *Journal of Nuclear Materials,* vol. 601, p. 155301, 2024.

[28] M. W. D. Cooper, G. Pastore, Y. Che, C. Matthews, A. Forslund, C. R. Stanek, K. Shirvan, T. Tverberg, K. A. Gamble, B. Mays and D. A. Andersson, “Fission gas diffusion and release for Cr2O3-doped UO2: From the atomic to the engineering scale,” *Journal of Nuclear Materials,* vol. 545, p. 152590, 2021.

[29] Y. S. Kim, “Fission Gas Release from U2+x in Defective Fuel Rods,” *International Topical Meeting on LWR Fuel Performance, Park City, Utah, April 10-13 2000, American Nuclear Society, cf. Nucl. Tech,* vol. 130, no. 1, pp. 9-17, 2000.

[30] R. J. White and M. O. Tucker, “A new fission-gas release model,” *Journal of Nuclear Materials,* vol. 118, no. 1, pp. 1-38, 1983.

[31] H. J. Matzke, “Gas release mechanisms in UO 2 —a critical review,” *Radiation Effects,* vol. 53, no. 3-4, pp. 219-242, 1980.

[32] G. Pastore, L. P. Swiler, J. D. Hales, S. R. Novascone, D. M. Perez, B. W. Spencer, L. Luzzi, P. V. Uffelen and R. L. Williamson, “Uncertainty and sensitivity analysis of fission gas behavior in engineering-scale fuel modeling,” *Journal of Nuclear Materials,* vol. 456, pp. 398-408, 2015.

[33] J. C. Killeen, “Fission gas release and swelling in UO2 doped with Cr2O3,” *Journal of Nuclear Materials,* vol. 88, no. 2-3, pp. 177-184, 1980.

[34] A. Claisse and P. Van Uffelen, “Towards the inclusion of open fabrication porosity in a fission gas release model,” *Journal of Nuclear Materials,* vol. 466, pp. 351-356, 2015.

[35] D. R. Olander, Fundamental Aspects of Nuclear Reactor Fuel Elements, Technical Information Center Energy Research and Development Administration, 1976.

[36] P. Van Uffelen, “Contribution to the Modelling of Fission Gas Release in Light Water Reactor Fuel,” 2002.

[37] Garzarolli, F., W. Jung, H. Shoenfeld, A. M. Garde, W. Parray and P. G. Smerd, “Review of PWR fuel rod waterside corrosion behavior, Technical Report EPRI NP-2789 Project 1250, Kraftwerk Union A.G. and Combustion Engineering Inc.,,” 1982.

[38] F. Garzarolli and M. Garzarolli, “PWR Zr alloy cladding water side corrosion, Technical Report, ANT International,” 2012.

[39] P. M. Gilmore, H. H. Klepfer and J. M. Sorensen, “EPRI PWR Fuel Cladding Corrosion (PFCC) Model Volume 1: Theory and User’s Manual, in EPRI Report, TR-105387-V1,” 1995.

[40] G. S. H. v. S. Leistikow, “Kinetik Und Morphologic der isothermen Dampf-Oxidation von Zircaloy-4 bei 700-1300°C, Kernforschungszentrum Karlsruhe, KFK 2587, March 1978”.

[41] G. Schanz, “Recommendations and supporting information on the choice of zirconium oxidation models in severe accident codes, Technical Report FZKA 6827, SAM-COLOSS-P043, Institut für Materialforschung, 2003”.

[42] J. T. Courtright and P. a. E. L., “Zircaloy-4 oxidation at 1300 to 2400°C, Technical Report NUREG/CR-4889, PNL-6166, 1987”.

[43] J. Cathcart, “Quarterly Progress Report on the Zirconium Metal-Water Oxidation Kinetics Program, in ORNL/NUREG/TM-41, 1976”.

[44] A. T. Motta, L. Capolungo, L.-Q. Chen, M. N. Cinbiz, M. R. Daymond, D. A. Koss, E. Lacroix, G. Pastore, P.-C. A. Simon, M. R. Tonks, B. D. Wirth and M. A. Zikry, Hydrogen in zirconium alloys: A review, J. Nucl. Mater., vol. 518, pp. 440-460, 2019, https://doi.org/10.1016/j.jnucmat.2019.02.042.

[45] F. Passelaigue, E. Lacroix, G. Pastore and A. Motta, “Implementation and Validation of the Hydride Nucleation-Growth-Dissolution (HNGD) model in BISON, J. Nucl. Mater., vol. 544, 152683, 2021”.

[46] J. Desquines, D. Drouan, M. Billone, M. Puls, P. March, S. Fourgeaud, C. Getrey, V. Elbaz and M. Philippe, “Influence of temperature and hydrogen content on stress-induced radial hydride precipitation in Zircaloy-4 cladding, J. Nucl. Mater., vol. 453,”.

[47] M. N. Cinbiz, A. T. Motta, D. Koss and M. Billone, “Hydride Reorientation in Zircaloy-4 under Different States of Stress as Studied with In Situ X-Ray Diffraction,” *Zirconium in the Nuclear Industry: 18th International Symposium, pp. 1252–1285, AST.*

[48] K. Une, S. Ishimoto, Y. Etoh, K. Ito, K. Ogata, T. Baba, K. Kamimura and Y. Kobayashi, “The terminal solid solubility of hydrogen in irradiated zircaloy-2 and microscopic modeling of hydride behaviour, J. Nucl. Mater., 389, pp. 127-136, 2009”.

[49] B. Kammenzind, D. Franklin, H. Peters and W. Duffin, “Hydrogen pickup and redistribution in alpha-annealed Zircaloy-4, Proceedings of the 11th International Symposium on Zirconium in the Nuclear Industry, ASTM STP1295, pp. 338-370, 1996”.

[50] W. Gong, P. Trtik, A. Colldeweih, L. Duarte, M. Grosse, E. Lehmann and J. Bertsch, “Hydrogen diffusion and precipitation in duplex zirconium nuclear fuel cladding quantified by high-resolution neutron imaging, J. Nucl. Mater., vol. 526, pp. 151757,” 2019.

[51] P. Konarski, C. Cozzo, G. Khvostov and H. Ferroukhi, “Development and testing of the hydrogen behavior tool for Falcon – HYPE, Nuclear Engineering and Technology, vol. 56(2) pp. 728-744, 2024 https://doi.org/10.1016/j.net.2023.11.012”.

[52] S. Shi and M. Puls, “ Criteria for fracture initiation at hydrides in zirconium alloys-I. Sharp crack tip, J. Nucl. Mater., 208 (1994), pp. 232-242 https://doi.org/10.1016/0022-3115(94)90332-8”.

[53] T. Aliev and M. Kolesnik, “Analytical approach to DHC description in zirconium alloys, Int. J. Fract., 228 (2021), pp. 71-84”.

[54] M. Billone, T. Burtseva and R. Einziger, “Ductile-to-brittle transition temperature for high-burnup cladding alloys exposed to simulated drying-storage conditions, J. Nucl. Mater., 433 (2013), pp. 431-448”.

[55] B. Michel et al, “OperaHPC: D9.2 - Detailed Work Plan for technical work Packages,” 2023.

[56] F. Feyel, “A multilevel finite element method (FE2) to describe the response of highly non-linear structures using generalized continua,” Comput. Methods Appl. Mech. Eng. (ISSN 0045-7825) 471 (28) (2003) 3233–3244, 2003.

[57] I. Ramière, R. Masson, B. Michel, S. Bernaud, “Un schéma de calcul multi-échelles de type Éléments Finis au carré pour la simulation de combustibles nucléaires hétérogènes,” 13e colloque national en calcul des structures. Université Paris-Saclay. Giens, Var, France, 2017.

[58] D. Baron, L. Hallstadius, K. Kulacsy, R. Largenton, J. Noirot, Fuel Performance of Light Water Reactors (Uranium Oxide and MOX - Comprehensive Nuclear Materials 2nd Edition, Elsevier Ltd - Editors: Rudy Konings, Roger E Stoller, 2020.

[59] J. Labat, R. Largenton, J.-C. Michel, “Multiscale identification and NTFA reduction of the elasto-viscoplastic polycrystalline behaviour of uranium dioxide (UO2) for wide range of loading conditions,” Journal of Nuclear Materials 582, 154471, 2023.

[60] R. Lofrano et al, “OperaHPC: MS4 - Detailed analysis of industrial models to improve,” 2024.

[61] G.J. Dvorak, Y. Benveniste, “On transformation strains and uniform fields in multiphase elastic media,” Proc. R. Soc. Lond. Ser. A, Math. Phys. Sci. 437 (1992) 291–310, 1992.

[62] G.J. Dvorak, “Transformation field analysis of inelastic composite materials,” Proc. R. Soc. Lond. Ser. A, Math. Phys. Sci. 437 (1992) 311–327, 1992.

[63] X. Zhang, C. Oskay, “Eigenstrain based reduced order homogenization for polycrystalline materials,” Comput. Methods Appl. Mech. Eng. (ISSN 0045-7825) 297 (2015) 408–436, 2015.

[64] J.L. Chaboche, S. Kruch, J.F. Maire, T. Pottier, “Towards a micromechanics based inelastic and damage modeling of composites,” Int. J. Plast. (ISSN 0749-6419) 17 (4) (2001) 411–439, 2001.

[65] R. Largenton et al, “OPERA-HPC: MS3 - Common methodology for the rheological non-linear mechanical modelling and homogenization techniques for fuels and claddings,” 2024.

[66] J.C. Michel, P. Suquet, “Nonuniform transformation field analysis,” Int. J. Solids Struct. (ISSN 0020-7683) 40 (25) (2003) 6937–6955, 2003.

[67] B. Halphen, Q. Son Nguyen, “Sur les matériaux standard généralisés,” J. Méc. 14 (1) (1975) 39–63, 1975.

[68] F. Fritzen, M. Leuschner, “Reduced basis hybrid computational homogenization based on a mixed incremental formulation,” Comput. Methods Appl. Mech. Eng. (ISSN 0045-7825) 260 (2013) 143–154, 2013.

[69] P. Ponte-Castaneda , “Exact second-order estimates for the effective mechanical properties of nonlinear composite materials,” J. Mech. Phys. Solids (ISSN 0022-5096) 44 (6) (1996) 827–862, 1996.

[70] S. Roussette, J.-C. Michel, P. Suquet, “Nonuniform transformation field analysis of elastic–viscoplastic composites,” Compos. Sci. Technol. (ISSN 0266-3538) 69 (1) (2009) 22–27, 2009.

[71] R. Largenton, J.-C. Michel, P. Suquet, “Extension of the nonuniform transformation field analysis to linear viscoelastic composites in the presence of aging and swelling,” Mech. Mater. (ISSN 0167-6636) 73 (2014) 76–100, 2014.

[72] J.C. Michel, P. Suquet, “A model-reduction approach to the micromechanical analysis of polycrystalline materials,” Comput. Mech. 57 (3) (2016) 483–508, 2016.

[73] J.-C. Michel, P. Suquet, “Effective potentials in nonlinear polycrystals and quadrature formulae,” Proc. R. Soc. A, Math. Phys. Eng. Sci. (ISSN 0020-7683) 473 (2017) 2204–2213, 2017.

[74] P. Ponte Castaneda, “Fully optimized second-order variational estimates for the macroscopic response and field statistics in viscoplastic crystalline composites,” Proc. R. Soc. A, Math. Phys. Eng. Sci. 471 (2015) 20150665, 2015.

[75] L. Sirovich, “Turbulence and the dynamics of coherent structures. Parts I--III.,” *Quarterly of Applied Mathematics,* vol. 45, no. 3, pp. 561-590, 1987.

[76] A. Quarteroni, A. Manzoni and F. Negri, Reduced basis methods for partial differential equations: an introduction, vol. 92, Springer International Publishing, 2016.

[77] M. Barrault, Y. Maday, N. C. Nguyen and A. T. Patera, “An 'empirical interpolation' method: application to efficient reduced-basis discretization of partial differential equations,” *Comptes Rendus Mathematique,* vol. 339, no. 9, pp. 667-672, 2004.

[78] S. Chaturantabut and D. C. Sorensen, “Nonlinear Model Reduction via Discrete Empirical Interpolation,” *SIAM Journal on Scientific Computing,* vol. 32, no. 5, pp. 2737-2764, 2010.

[79] C. Farhat, P. Avery, T. Chapman and J. Cortial, “Dimensional reduction of nonlinear finite element dynamic models with finite rotations and energy-based mesh sampling and weighting for computational efficiency,” *International Journal for Numerical Methods in Engineering,* vol. 98, no. 9, pp. 625-662, 2014.

[80] D. Ryckelynck, “Hyper-reduction of mechanical models involving internal variables,” *International Journal for Numerical Methods in Engineering,* vol. 77, no. 1, pp. 75-89, 2009.

[81] J. Fauque de Maistre, Hybrid hyper-reduced modeling for contact mechanics problems, Paris: Ph.D. Thesis, Université Paris Science et Lettres, 2018.

[82] J. Fauque, I. Ramière and D. Ryckelynck, “Hybrid hyper-reduced modeling for contact mechanics problems,” *International Journal for Numerical Methods in Engineering,* vol. 115, no. 1, pp. 117-139}, 2018.

[83] S. Le Berre, I. Ramière, J. Fauque and D. Ryckelynck, “Condition Number and Clustering-Based Efficiency Improvement of Reduced-Order Solvers for Contact Problems Using Lagrange Multipliers,” *Mathematics,* vol. 10, no. 9, p. 1495, 2022.

[84] F. Fritzen, B. Haasdonk, D. Ryckelynck and S. Schöps, “An Algorithmic Comparison of the Hyper-Reduction and the Discrete Empirical Interpolation Method for a Nonlinear Thermal Problem,” *Mathematical and Computational Applications,* vol. 23, no. 1, p. 8, 2018.

[85] S. Kashibe, K. Une and K. Nogita, “Formation and growth of intragranular fission gas bubbles in UO2 fuels with burnup of 6-83 GWd/t,” *Journal of Nuclear Materials,* no. 206, pp. 22-34, 1993.

[86] L. Noirot, “Margaret: A comprehensive code for the description of fission gas behavior,” *Nuclear Engineering and Deisgn,* no. 241, pp. 2099-2118, 2011.

[87] D. Pizzocri, M. D. Gennaro, T. Barani, F. Silva, G. Zullo, S. Lorenzi and A. Cammi, “A reduced order model for fission gas diffusion in columnar grains,” *Nuclear Engineering and Technology,* no. 55, pp. 3983-3995, 2023.

[88] L. Bernard, J. Jacoud and P. Vesco, “An efficient model for the analysis of fission gas release,” *Journal of Nuclear Materials,* no. 302, p. 125.134, 2002.

[89] C. Introïni, I. Ramière, J. Sercombe, B. Michel, T. Helfer and J. Fauque, “ALCYONE: the fuel performance code of the PLEIADES platform dedicated to PWR fuel rods behavior,” *Annals of Nuclear Energy,* vol. 207, p. 110711, 11 2024.

Appendix A. Review of state-of-the-art in multi-dimensional fuel behaviour analysis

A.1 Fuel behaviour modelling

Most of the fuel performance codes used for fuel behaviour analysis typically use the one-dimensional (1-D) modelling approach. More precisely, a 1.5-D approach is used to approximate the fuel rod analysis by assuming axisymmetric one-dimensional radial representation with subdivision of the rod into a stack of mechanically independent axial slices. The axial coupling is ensured by iterating the solution of the code over those slices. Most notable fuel performance codes adopting this 1.5D approach include TRANSURANUS [A1] developed at the JRC, Germany; the FRAP series including FRAPCON [A2] and FRAPTRAN [A3] developed by the US-NRC; the FEMAXI code [A4] developed by the JAEA, Japan; and the ENIGMA code [A5][A6] developed by the BNFL-CEGB in the UK.

A 2-D modelling approach enables to have the analysis for both the r-z (radial-axial) and r-θ (radial-azimuthal) planes. For the r-z analysis, an axisymmetric rod is still assumed but unlike the 1.5D approach, the axial gradients are not neglected, and the governing equations are solved both radially and axially. For the r-θ analysis, rather than the entire fuel rod length, thin slices at specific axial locations are analysed without axisymmetry but assuming plane strain or similar. This approach is useful to study local effects, such as the pellet crack and clad ridging. A notable fuel performance code making use of the such 2-D capabilities is Falcon [A7] developed at EPRI. Falcon is the reference code for fuel behaviour analysis at PSI.

A full 3-D modelling approach does not impose any a-priori assumption on the geometry of the rod. There exist a few well established 3-D fuel performance codes and also some currently developing multi-dimensional codes. Notable multi-dimensional codes include BISON [A8] developed at INL, USA; ALCYONE [A9][A10] developed by the CEA in France; DIONISIO [A12] developed at CNEA, Argentina and OFFBEAT [A13] co-developed at EPFL and PSI, Switzerland.

A non-exhaustive list of Fuel performance codes around the world with their modelling capabilities are presented in Table **13**.

Table 13: Fuel performance codes around the world.

Code	**Organization/Country**	**Modelling capability**
ALCYONE	CEA, France	1.5D, 2D, 3D
BACO	CNEA, Argentina	1.5D
BISON	INL, USA	1.5D, 2D, 3D
CAMPUS	CNL, Canada	2D(r-z)
DIONISIO	CNEA, Argentina	1D, 2D, 3D
ENIGMA	BNFL-CEGB, UK	1.5D
FALCON	EPRI, USA	2D(r-z), 2D(r-θ)
FEMAXI	JAEA, Japan	1.5D
FAST (FRAPCON + FRAPTRAN)	US-NRC, USA	1.5D
OFFBEAT	EPFL/PSI, Switzerland	1D, 2D, 3D
SCANAIR	IRSN, France	1.5D
TRANSURANUS	JRC, Germany	1.5D

A more detailed review of the fuel performance codes around the world can be found in [A14]. The multi-dimensional fuel performance codes and the different models included in them will be discussed in detail in the following section.

A.2 Multi-dimensional fuel performance codes

Although two-dimensional codes respond to most of the thermo-mechanical phenomena, there are certain asymmetries for which these models have limited capabilities. Phenomena such as the eccentricity of the pellet and cladding, the asymmetry in temperature distribution due to the position of a rod in a bundle, or the presence of a defect in the pellet, like missing pellet surface, among others, would require a full 3D analysis and a 3D fuel behaviour code can deliver results that better represent the experiments than a 2D code. Some already existing multi-dimensional fuel behaviour codes and those under development are presented in this section.

A.2.1 BISON

BISON [A8] is a modern parallel, finite element-based fuel performance code developed at Idaho National Laboratory (INL) since 2009. The code is applicable to both steady state and transient fuel behavior and has been used to analyse a variety of fuel forms in 1D, 2D, or 3D geometries. BISON is built upon INL's Multiphysics Object-Oriented Simulation Environment (MOOSE) [A15] which is a parallel, finite element-based framework to solve systems of coupled non-linear partial differential equations using the Jacobian-free Newton Krylov (JFNK) method. The object-oriented architecture employed in MOOSE facilitates adding of new material and behaviour models with minimum programming efforts. The BISON governing equations are fully coupled partial differential equations for energy, mass, and momentum conservation. The various models used in BISON are presented below categorizing them into fuel related, gap related and cladding related models.

A.2.1.1 Fuel pellet related models

The fuel thermal conductivity can be computed by the empirical modes of Fink [A16] and Lucuta [A17], for unirradiated and irradiated materials, respectively. Other models for computing fuel thermal conductivity include MATPRO [A18] and NFIR [A19].

Fuel swelling due to both solid and gaseous fission products is included using empirical relations from MATPRO [A20]. Gaseous swelling can also be determined using a physics-based model by Pastore et al [A21].

Fuel densification is computed using the ESCORE [A7] empirical model.

The model for combined secondary thermal creep and irradiation creep of UO2 is taken from the MATPRO [A20] FCREEP material model.

Two approaches are available in BISON to account for fuel cracking and relocation: a simple empirical relocation model and a smeared cracking model. The relocation model is taken from ESCORE [A7]. The smeared cracking model follows the approach in [A22], where cracking is simulated by adjusting the elastic constants at material points, in contrast to a discrete cracking model, where topographic changes are made to the finite element mesh.

The radial power profile in BISON is calculated using the same model by Soba et al. [A23], which was developed for the DIONISIO fuel performance code [A24].

A.2.1.2 Gap related model

The gap heat transfer in BISON is computed in the traditional manner with the total gap conductance as a sum of the gas conductance, the increased conductance due to solid–solid contact, and the conductance due to radiation as described in Section 1.1.4. The gas conductance is given by Ross and Stoute [A25], with the conductivity of the gas mixture computed using the mixture rule from MATPRO [A20].

The gap solid-solid contact model in BISON is based on the methodology of Heinstein and Laursen [A26], which utilizes node to face constraints to prevent nodes on one surface from penetrating the face of another surface.

FGR and gaseous swelling in BISON are computed by a physics-based model by Pastore et al [A21]. FGR can also be computed using the Forsberg–Massih model [A27].

A.2.1.3 Cladding related models

The thermal and irradiation creep models for Zircaloy cladding available in BISON are given by Limbäck and Andersson [A28].

Cladding elongation as a result of irradiation-induced growth is included in BISON using the ESCORE [A7] empirical model or the Franklin model [A29].

A.2.2 ALCYONE

ALCYONE [A9][A10][A11] is a multi-dimensional fuel code for French PWR rods co-developed by EDF, AREVA and CEA. ALCYONE has been developed in the framework of the PLEIADES environment [A30][A31][A32].

ALCYONE uses the 1.5D scheme to model the complete fuel rod discretized in axial segments, the fuel and cladding of each segment being further divided in annular rings. The 2D (r-θ) scheme models the mid-pellet plane of a pellet fragment whereas for the 3D scheme a fuel pellet is divided in 8 identical fragments, and it models the behavior of one quarter of a pellet fragment with the overlying cladding. All these different schemes use the same Finite Element (FE) code CAST3M [A33] to solve the thermo-mechanical problem and share the same physical material models at each node or integration points of the FE mesh.

ALCYONE includes a number of modules that can be used independently or called at each node of the mesh. A typical coupled calculation requires the iterative run of successive steps of neutronics, thermo-mechanical calculation, fission gas calculation, and thermo-chemistry until convergence is achieved. ALCYONE is coupled with different models that can be called during a run, for example, PRODHEL for neutronics, MARGARET for FGR and ANGE for thermo-chemistry. Schematic representation of the calculation process and models called during a simulation performed with ALCYONE V2.0 is shown in Figure 18.

The various models used in ALCYONE are presented below categorizing them into models related to fuel, gap, or cladding properties. The openly available literature on the models used in ALCYONE is quite limited and therefore further details cannot be provided.

A.2.2.1 Fuel properties

The fuel thermal conductivity is calculated using the modified Lucuta's formulation [A17]. The thermal expansion coefficient is obtained according to the recommendations of Martin [A35].

The irradiation, scattering and dislocation creep of UO2 is calculated using the methodology in Monerie & Gatt [A36].

The fuel cracking is modelled using a (r, θ, z) 3D smeared crack model which accounts for fuel pellet fragmentation during nominal loading and for the development of secondary cracks during transient loading [A37].

Fuel densification and solid swelling is modelled using MATPRO [A20]. The radial power profile is calculated using the RADAR [A38] model.

A.2.2.2 Gas gap properties

The heat transfer in the gap again follows the traditional gap conductance approach. The model used in ALCYONE to calculate gap conductance is the revised URGAP model [A39].

The contact between the pellet and cladding at gap closure is modelled based on the Coulomb's friction law [A40].

The FGR and gaseous swelling is modelled using the MARGARET code [A41].

A.2.2.3 Cladding properties

The thermal conductivity of the Zircaloy cladding is computed by the temperature dependent model in MATPRO [A20].

The irradiation-induced creep, thermal creep and plasticity is computed using anisotropic formulation based on Hill's criterion [A42].

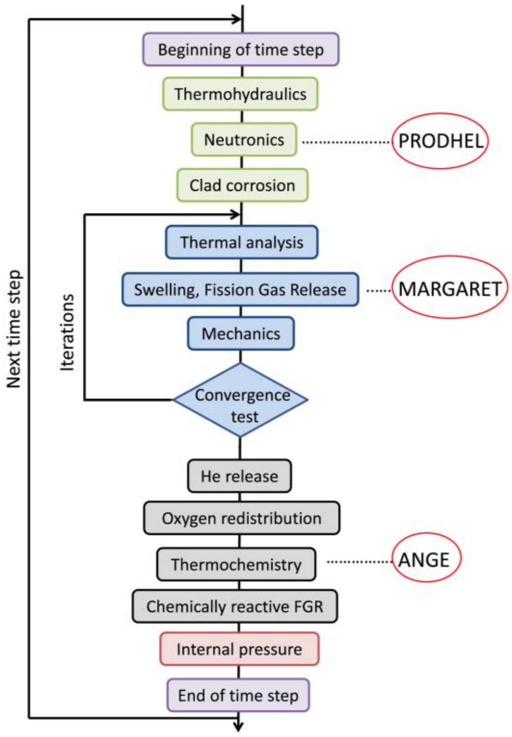

Figure 18: Schematic representation of the calculation process and models called during a simulation performed with ALCYONE V2.0 [A34]

A.2.3 DIONISIO

DIONISIO [A24][A12] is a finite element code to simulate fuel rod behaviour during irradiation under normal or accident operation of a nuclear reactor. It has more than fifty interconnected models coupled in a modular structure, to predict thermo-mechanical, thermo-chemical and thermo-hydraulic behavior of fuel rod. A newer version of the DIONISIO code, extending its capabilities to three-dimensional domains was developed as DIONISIO 3.0 [A43].

The various models used in DIONISIO are presented below categorizing them into models related to fuel, gap, or cladding.

A.2.3.1 Fuel related

The thermal conductivity of UO2 is given by the expression from Delette & Charles [A44].

The coefficient for thermal expansion is taken from Olander [A45].

The creep law for UO2 is used from MATPRO v11 [A18].

The swelling due to fission products is calculated using the expression from Olander [A45] and the Fuel densification is calculated from the expression from the BACO code [A46].

The radial power profile in DIONISIO is calculated using the model by Soba et al. [A23].

A.2.3.2 Gap related

The heat transfer in the gap again follows the traditional gap conductance approach.

For the pellet clad contact, the 3D version of DIONISIO uses an algorithm based on cohesive elements [A47], with a linear contact law that does not alter the system's resolution matrix, making it simpler to solve and easier to parallelize.

The fission gas release is dealt with a model presented in Denis and Soba [A48].

A.2.3.3 Cladding related

The thermal conductivity of the Zr cladding in DIONISIO is taken from the expression of Fink [A49].

The coefficient for thermal expansion of Zr is taken from Olander [A45].

The creep law for Zr is used from FRAPCON-2.0 [A50].

The irradiation growth of the Zr cladding is modelled using the approach used in the BACO code [A46] for PHWR fuel rod simulation.

A.2.4 Falcon

At PSI, the reference code for fuel behaviour analysis is Falcon [A7]. Falcon is a 2D fuel behaviour code developed by EPRI and has been verified and validated to a great extent over the course of its development and usage. Falcon supports 2D axisymmetric analysis (r-z) of full-length fuel rods and can also be used for further detailed analysis of 2D slices (r-θ) at selected axial locations to study radial and angular effects. Based on a robust finite element numerical structure, Falcon is capable of analysing both steady state and transient fuel behavior with a seamless transition between the two modes.

Currently, several versions of the FALCON code exist and are being used for fuel analyses by multiple users. The FALCON MOD01 code was originally released in 2004. The latest version, Falcon v1.5.0, was released in 2020 and has substantial changes and additions to both coding and behavioural models. Because of the presence of independent code modifications, different default and optional models used, and indeed even modelling methodology, the effects of these differences must be considered when making comparisons between the results obtained from different code versions.

The thermal and mechanical properties and behavioural models available in Falcon for the fuel, gap and cladding components of the fuel rod are presented in Figure 19.

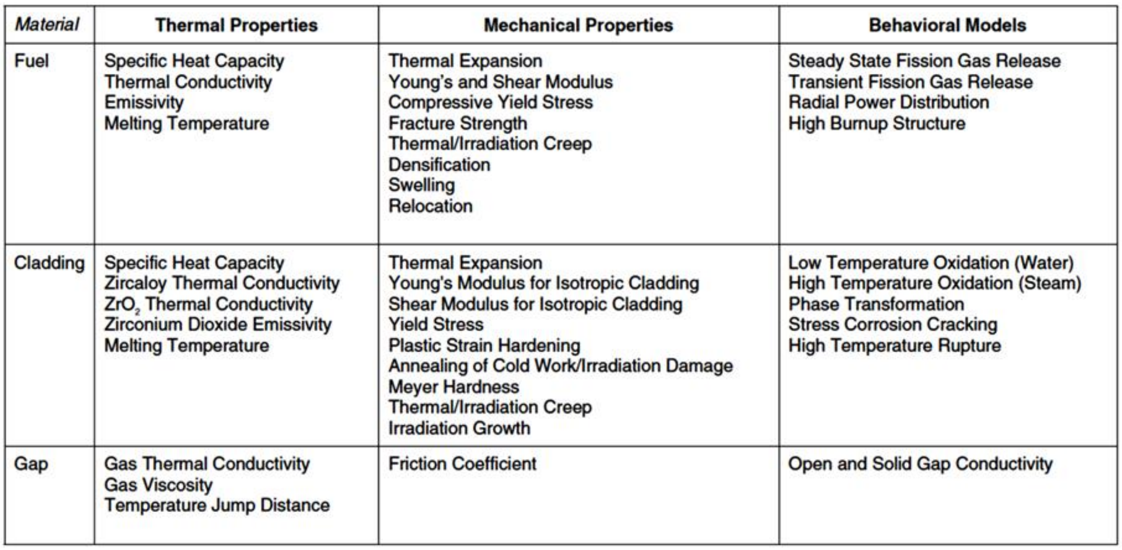

Material	**Thermal Properties**	**Mechanical Properties**	**Behavioral Models**
Fuel	Specific Heat Capacity Thermal Conductivity Emissivity Melting Temperature	Thermal Expansion Young's and Shear Modulus Compressive Yield Stress Fracture Strength Thermal/Irradiation Creep Densification Swelling Relocation	Steady State Fission Gas Release Transient Fission Gas Release Radial Power Distribution High Burnup Structure
Cladding	Specific Heat Capacity Zircaloy Thermal Conductivity ZrO_2 Thermal Conductivity Zirconium Dioxide Emissivity Melting Temperature	Thermal Expansion Young's Modulus for Isotropic Cladding Shear Modulus for Isotropic Cladding Yield Stress Plastic Strain Hardening Annealing of Cold Work/Irradiation Damage Meyer Hardness Thermal/Irradiation Creep Irradiation Growth	Low Temperature Oxidation (Water) High Temperature Oxidation (Steam) Phase Transformation Stress Corrosion Cracking High Temperature Rupture
Gap	Gas Thermal Conductivity Gas Viscosity Temperature Jump Distance	Friction Coefficient	Open and Solid Gap Conductivity

Figure 19: Thermo-mechanical properties and behavioural models Included in Falcon (From [A7]).

A.2.5 OFFBEAT

The OpenFOAM Fuel Behavior Analysis Tool - or OFFBEAT [A13] is a multi-dimensional fuel behaviour analysis tool currently being co-developed by the École Polytechnique Fédérale de Lausanne (EPFL) and Paul Scherrer Institute (PSI). As the name suggests, OFFBEAT is based on OpenFOAM, an open-source C++ numerical library. A direct consequence of the choice of OpenFOAM as development platform, is the use of the Finite Volume Method (FVM). This is something which differentiates OFFBEAT from other fuel performance codes which typically employ the Finite Element Method (FEM) if not the simpler Finite Difference Method (FDM). The application of the FVM and numerical methodology adopted in OFFBEAT can be found in the PhD thesis of Scolaro [A51].

Like any solver built with the OpenFOAM library, OFFBEAT is an inherently 3-D code: the geometries are always 3-D, and by default, the code solves the equations in a 3-D Cartesian coordinate system. However, 2-D and even 1-D simulations can be performed using an appropriate geometry and by selecting appropriate boundary conditions (Figure A.3). It can be used for the transient analysis of complex 2D and 3D phenomena as well as for the 1.5D or 2D axisymmetric study of the steady-state base irradiation.

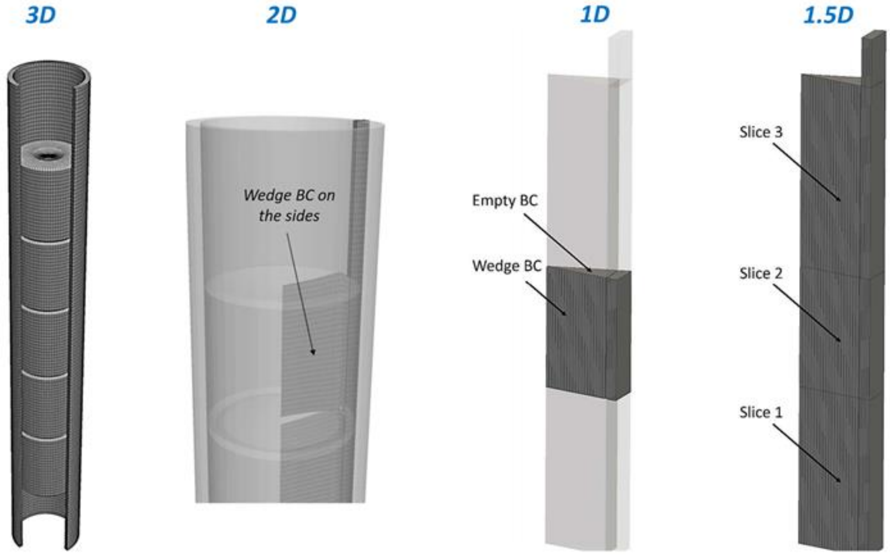

Figure 20: Multi-dimensional geometries in OFFBEAT by using appropriate boundary conditions [A51].

OFFBEAT follows a modular approach, having different functionalities in independent C++ classes, which simplifies incorporating new modules and reduces the time needed for code maintenance. The two main components of OFFBEAT are a thermal and a mechanical sub-solver to calculate the temperature distribution and the deformation of the fuel rod, respectively. This is complemented by supplementary classes including a gap/plenum model, heat source and fast flux models, fission gas release models, a class for the isotopic evolution of the oxide fuel and its burnup, a class handling the material properties, a class dedicated to the phenomena affecting the gap size such as relocation or densification, a rheology class for the constitutive mechanical behavior of the materials, among others.

Employing a segregated solution or operator-splitting (and dimensional-splitting) scheme, OFFBEAT solves each physics and each component separately and sequentially, treating the dependence on other variables with explicit terms. The segregated solution scheme in OFFBEAT is categorized into three main loops: the time-iteration loop for advancing in time, the outer fixed-point iteration loop for solving the coupled physics and closure models and inner-iteration loops for each primary sub-solver. The solution scheme with the inner, outer and time loops in OFFBEAT is shown in Figure 21.

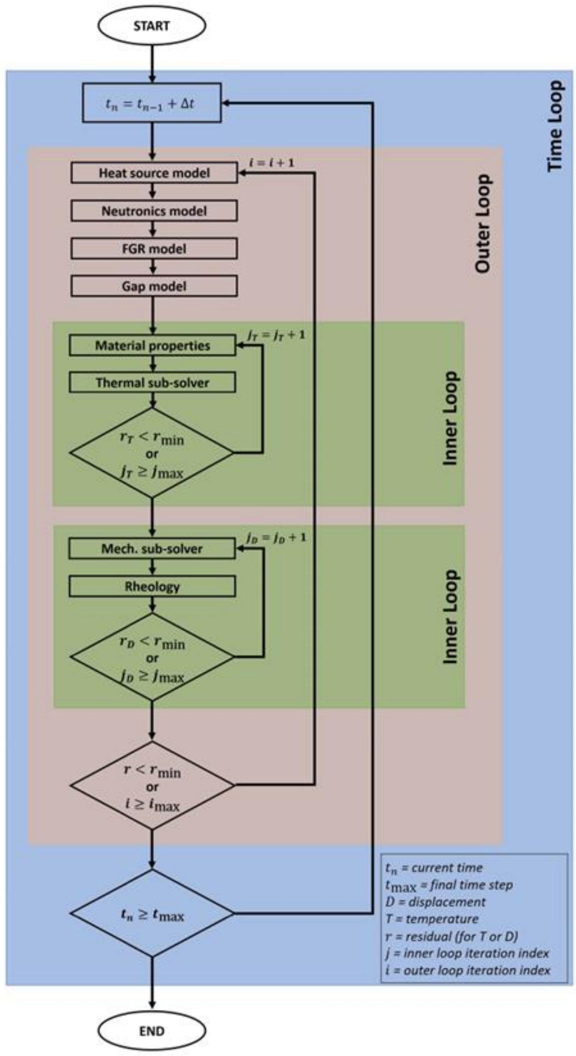

Figure 21: Solution scheme adopted in OFFBEAT (From [A51])

The models adopted in OFFBEAT for the phenomena occurring in the fuel, gap and cladding components of the fuel rod are presented below.

A.2.5.1 Fuel related phenomena

The material properties of UO2 like specific heat capacity, thermal expansion, surface emissivity, are modelled using the correlations from MATPRO v11 [A18].

The thermal conductivity of UO2 can be calculated with the MATPRO [A20] routine FTHCON. It can also be calculated using the (Nuclear Fuel Industry Research) NFIR model proposed by Marion [A19].

Fuel densification is calculated using the FUDENS routine and the solid fission product swelling using the FSWELL routine of MATPRO [A20]. The gaseous fission product swelling is calculated by the FGR model SCIANTIX [A52].

The effect of fuel cracking is treated with the isotropic cracking model derived from Barani et al. [A53]. The fuel relocation due to cracking can be treated with a simple relocation model derived from FRAPCON4.0 [A54]. The recovery after relocation is considered in the relocation model of OFFBEAT.

The isotopic concentrations of selected isotopes are tracked in OFFBEAT with a simplified neutronics model, which is derived from the TUBRNP module [A55] of TRANSURANUS. This enables the calculation of the radial power profile and the local burnup. A higher fidelity coupling strategy between the Monte Carlo code Serpent [A56] and OFFBEAT has also been developed to increase the accuracy of the calculations that lie outside the range of applicability of TURBNP. Efforts are currently underway to incorporate a simple 1D neutron diffusion solver in OFFBEAT as an additional alternative to TUBRNP.

The creep model for UO2 is derived from the FCREEP routine of MATPRO [A18], following the implementation of BISON.

A.2.5.2 Gap related phenomena

The gap heat transfer model adopts the traditional gap conductance calculation, and the model is derived from the coding of FRAPCON4.0 [A54].

OFFBEAT is equipped with two algorithms for the fuel-to-cladding contact. First approach is loosely based on the explicit penalty method proposed by Cardiff et al. [A57]. The second approach is the novel implicit methodology developed in the thesis work of Scolaro [A51].

The fission gas behavior is considered in OFFBEAT either with a simplified model derived from the modified Forsberg-Massih model described in the FRAPCON 4.0 manual or with SCIANTIX [A52], a 0-D open-source code developed at the Politecnico di Milano.

A.2.5.3 Cladding related phenomena

The thermal conductivity and the thermal expansion coefficient of Zircaloy are derived from the CTHCON and CTHEXP routines of MATPRO [A18], respectively. The specific heat capacity and the density of Zr are calculated following the approach in the IAEA Report IAEA-TECDOC-1496 [A58]. The instantaneous plasticity model implemented in OFFBEAT is based on the classic Von Mises theory of plasticity. The thermal and irradiation creep models for Zircaloy cladding available in OFFBEAT are given by Limbäck and Andersson [A28]. The Zircaloy irradiation growth is treated with a model derived from ESCORE [A7], which calculates the additional axial strain as a function of the neutron fluence. MATPRO v11 [A20] can also be chosen as an option to model irradiation growth.

A.3 OFFBEAT: Possible Extensions

OFFBEAT is a fuel behaviour code which is currently under development. New models and methodologies are envisaged to be incorporated into the code to make it more precise in dealing with phenomena impacting fuel behaviour during normal and off-normal operating conditions in a nuclear reactor. Some of the phenomena that have been identified to be incorporated into OFFBEAT are presented in this section. The detailed description of the modelling methodology for these phenomena can be found in the corresponding references.

A.3.1 Cladding oxidation

The water-side corrosion can affect both the thermal and mechanical properties of the cladding. The oxidation of Zircaloy cladding is modelled in OFFBEAT using the correlations described in the documentation of the ZryOxidation class [A60][A61] is used. The model parameter values are used to derive the time-dependent oxide layer thickness growth. Another model for normal operating temperatures, which is available in BISON and Falcon fuel behaviour codes is the EPRI SLI Model [A41]. It uses enhanced model parameters by considering factors that are a function of coolant lithium content, alloy tin and iron content, hydrogen content, and fast flux. A detailed description of these parameters can be found in Gilmore et al [A62]. The EPRI SLI Model can be added as an option to choose for normal operating temperature regime oxidation in OFFBEAT.

For the high temperature range, different correlations are used for different temperature ranges to determine the oxide scale thickness. Similar to BISON, the Leistikow correlation [A63] is used for temperatures from 673 K up to 1800 K. For temperatures between 1800 K and 1900 K, a linear interpolation between two correlations is made using the procedure from Schanz [A64]. For temperatures above 1900 K, the Prater-Courtright correlation [A65] is used.

The Cathcart-Pawel correlation [A66] is also available in BISON and Falcon fuel behaviour codes and can be added as an option to choose from for the high temperature cladding oxidation in OFFBEAT. Moreover, currently OFFBEAT does not make a distinction between Zr-2 and Zr-4 cladding types and the correlations are different for different cladding types. The option to select different types of cladding can be added to OFFBEAT and the corresponding oxidation correlations can then be used.

Very recently, Scolaro et al. [A67] at EPFL carried out the first steps toward the development of a methodology in OFFBEAT for modelling the formation of non-uniform oxide layers in Zircaloy claddings and studying their impact on the rod’s thermal and mechanical response under irradiation.

A.3.2 Hydrogen uptake and hydride formation

A portion of the hydrogen produced during water-side corrosion enters the zircaloy cladding. This phenomenon is called hydrogen pickup or uptake [A68]. This dissolved hydrogen makes the cladding material more susceptible to plastic deformation at high temperature. At high concentration, the dissolved hydrogen forms brittle hydrides, hydrogen compounds with the alloying elements. Hydride formation and therefore H-uptake pose a serious concern regarding fuel cladding performance since a) the hydride concentration has a positive feedback on corrosion rate; b) the higher specific volume of hydride compared to Zr leads to increased dimensional changes in the cladding; c) Zr-hydride is brittle and this weakening of the cladding mechanical performance is of utmost importance for LOCA, RIA, cask-drop accident and storage [A69]. The hydrogen pickup fraction has been well characterized for various zirconium alloys [A68][A70][A71] and was found to be a strong function of alloying elements and to be a complex function of the exposure time. An extensive review of hydrogen behaviour in Zircaloy claddings has been done by Motta et al. [A72].

Although development efforts are underway, at present, OFFBEAT does not include any model for hydrogen behaviour and it is of interest to consider the available models and methodologies adopted in other fuel behaviour codes. In BISON, the hydrogen pickup models are implemented for the different types of claddings. For Zircaloy-4, M5, Zirlo and Optimized Zirlo cladding types, the user specifies a fixed instantaneous hydrogen pickup fraction, so that the average total concentration of hydrogen CH (including dissolved hydrogen and hydrogen as Zr-hydride) in the cladding, which is roughly proportional to the thickness of the oxide layer, can be determined [A73]. The hydrogen pickup model, which was initially implemented along with an oxidation model, was coupled with the existing oxidation models in BISON [A74]. For Zircaloy-2 claddings, the hydrogen pickup models use either the concentration of hydrogen calculated as a function of local axial burnup [A75], or the hydrogen flux based on the linear heat rate or linear power [A76]. A new model, called Hydride Nucleation-Growth-Dissolution (HNGD) [A77] was implemented into BISON to model physical processes involved in hydrogen redistribution, and hydride precipitation and dissolution. The main innovative feature of the HNGD model is that it accounts for hydride nucleation and growth as two distinct precipitation components.

Recently a tool for hydrogen behaviour, coupled to Falcon output was developed at PSI. This tool, called HYPE (Hydrogen Postprocessor for Falcon) [A78], extracts data from a Falcon output file and uses them to calculate hydrogen uptake, transport, thermochemistry, and reorientation of hydrides. The tool models hydrogen behaviour in 1.5D, i.e., independent calculations are performed in cylindrical coordinates in each axial slice of the studied rod. The hydrogen pickup models used in HYPE depend on the reactor type. For BWR claddings, the pickup correlation is burnup-dependent and for PWR, the hydrogen uptake is expressed as a function of the oxide thickness. The correlations for BWR claddings come from [A69], which account for the higher burnups reached in Swiss BWR fuels. The PWR claddings correlation is for oxide thickness can be determined as in [A73] using the hydrogen uptake fractions proposed by US NRC [A71]. Hydride reorientation is modelled in HYPE using the model proposed by Desquines et al. [A79]. The hydride dissolution and precipitation model in HYPE has been adapted from the HNGD model [A77].

A similar approach for hydrogen uptake and hydride precipitation and dissolution can be adopted for OFFBEAT.

A.3.3 Hydrogen transport

It has been recently proposed that the driving force for hydrogen pickup is inversely proportional to the electronic conductivity of the protective oxide layer. It is necessary for the electrons to travel through the protective oxide layer to recombine with the hydrogen in the water. If the oxide electronic conductivity is not sufficiently high, hydrogen can migrate through the protective oxide layer to recombine with electrons and be absorbed into the metal. The transport mechanism of hydrogen through the oxide layer in response to this driving force is not yet determined, but it is now thought that hydrogen travels through the protective oxide as H+ on the way to entering the metal [A72].

Depending on the local conditions, hydrogen in zirconium alloys is either dissolved in solid solution or precipitated to secondary phase hydrides. Veshchunov et al. [A80] stated that hydrogen diffuses through the zirconium hydride structure if the volume fraction of hydrides is sufficiently high. The hydrogen that enters the cladding can respond relatively quickly to established driving forces which can drive a hydrogen flux to regions of the solid. The hydrogen flux is due to the combined effects of Fick's law of diffusion, the Soret effect and stress gradients [A72] as:

$$J_{hydrogen} = J_{Fick} + J_{Soret} + J_{stress} \tag{A.1}$$

The expressions for each of these fluxes can be found in [A72][A73]. The diffusion coefficient of hydrogen in zirconium, has been measured several times in the literature [A81][A82]. The hydrogen transport will have to be modelled in OFFBEAT in order to deal with the hydrogen behaviour in the fuel rod system. A schematic representation of the water-side corrosion and the hydriding process is shown in Figure 22.

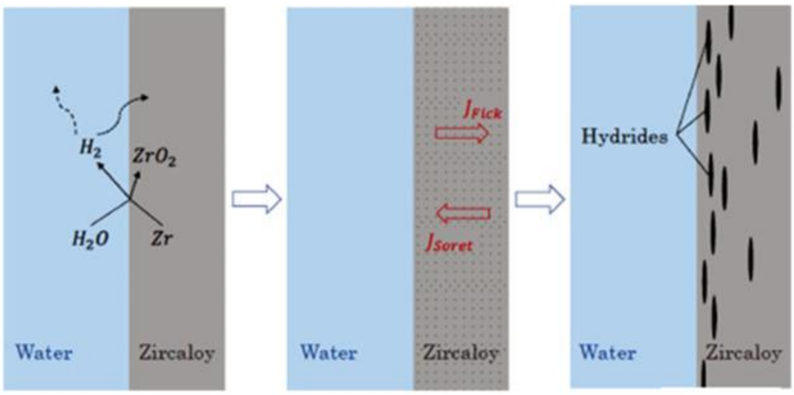

Figure 22: Schematic representation of the water-side corrosion and the hydriding process (From [A77]).

A.3.4 Liner claddings

Apart from the widely used and studied Zircaloy-4, the Swiss nuclear industry uses duplex claddings, called Liner claddings. Zircaloy-2 with an inner layer is used in BWRs and Zircaloy-4 with an outer layer in PWRs. The liner claddings are characterized by a different hydrogen behavior compared to non-liner claddings. Such claddings consist of two layers, a thick substrate providing the mechanical strength of the cladding and a thin liner. The purpose of using the inner liner in BWR claddings is to soften the pellet-cladding mechanical interaction. The outer liner used in PWR claddings is aimed at limiting waterside corrosion.

Extensive experimental work has been carried out at PSI in Switzerland for both BWR and PWR related liner claddings. Hydrogen behavior in PWR duplex cladding from Framatome, DXD4, was experimentally studied by Gong et al. [A83]. This cladding material is widely used in KKG. It consists of a Zircaloy-4 substrate and a low-tin outer liner. Gong et al. have shown that hydrogen tends to migrate towards the liner during cooling and accumulates at Substrate-Liner Interface (SLI). Fagnoni et al. [A84] studied the hydrogen behavior in two BWR inner-liner claddings LTP (Framatome) and LK3/L (Westinghouse). Contrary to the outer liner experiments, the average hydrogen concentrations for the inner liner accounted for the hydrogen located in the edges.

Since the liner claddings, both inner and outer, behave quite differently than the standard claddings, separate modelling approach is required to model the hydrogen behaviour. Modelling approach for hydrogen behaviour in liner claddings and its validation against experiments has been done by Konarski et al. at PSI. This approach has also been adopted in the HYPE model [A85]. Although OFFBEAT handles multi-material modelling quite well using a model adapted from the model of Tukovic [A86], it has never been tested for liner claddings as, currently, OFFBEAT does not have any liner-specific material properties. Thus, when developing hydrogen behaviour models, it would be important to also consider the different types of cladding, especially the liner ones, which are of interest to the Swiss nuclear industry. The capability of the multi-material modelling in OFFBEAT would then be tested for liner-claddings, incorporating the liner material properties.

A.3.5 Other extensions

Another extension to the OFFBEAT fuel performance code can be to the fuel cracking modelling. Currently, OFFBEAT models the effect of cracking employing relocation and isotropic cracking approaches derived from axisymmetric traditional codes. The analysis of pre-determined 3-D cracking pattern or the analysis of pellet fragments should be considered like in the ALCYONE code [A37]. Some other ideas to extend/improve the capabilities of OFFBEAT include the following:

- OFFBEAT currently has no dedicated thermal-hydraulics solution. A simplified homogeneous equilibrium model should be included as a minimum, but couplings to subchannel and/or CFD solutions should be considered.
- The material properties and models should be extended to accommodate different cladding materials and liner materials.
- Chemistry within reactor fuels and claddings and possible stress corrosion cracking.
- Migration of void within the fuel and the potential formation of a central void.
- Further explicit modelling of crud build-up and its thermo-mechanical effects [A67].
- Pellet-clad bonding.
- Possible trapping of gap gases. PSI's in-house Falcon version currently includes coupling to the axial gas transport code FRELAX which allows for trapping of gap gases [A87].
- The simplified 0-D gap conductance model used by virtually all fuel performance codes, including OFFBEAT, could be extended to incorporate multi-dimensional effects. Such effects might be relevant for, for example, the heat transfer in the chamfer regions of the pellet or in the case of missing pellet surfaces.
- Hydrogen transport could be extended to incorporate the effects of cladding defects. Such defects would cause stress concentrations, which would attract hydrogen and potentially lead to excessive hydride formation.
- OFFBEAT currently cannot model RIA scenarios where the melting of fuel potentially occurs. Extensions would be needed to model, for example, the Power to Melt and Manoeuvrability (P2M) experiments of the OECD/NEA FIDES Joint Experimental Programme (JEEP) [A88].
- The dry storage models incorporated in Falcon at PSI, as part of the DrySTARS Project, could of course be incorporated in OFFBEAT, although the need for 3D dry storage behaviour should be assessed.
- The phenomenon of shadow corrosion is an inherently 3D phenomena which can lead to excessive corrosion in the locations of spacer grids. A 3D multi-physics code like OFFBEAT may be a perfect candidate for studying this effect.
- While not necessarily a 3D effect, including the GRSW-A model [A89] as a complementary optional fission gas release model in OFFBEAT can be considered; in this case, however, the model could not be made open-source and would be for PSI internal use only.

A.4 References

[A1] K. Lassmann, TRANSURANUS: a fuel rod analysis code ready for use, *Journal of Nuclear Materials, vol. 188, pp. 285-302, 1992* https://doi.org/10.1016/B978-0-444-89571-4.50046-3

[A2] G. A. Berna, C. E. Beyer, K. L. Davis, and D. D. Lanning, FRAPCON-3: A computer code for the calculation of steady-state, thermal-mechanical behavior of oxide fuel rods for high burnup, *US Nuclear Regulatory Commission* (NRC) *NUREG/CR-6534-Vol. 2, 1997*

[A3] K.J. Geelhood, W.G. Luscher, C.E. Beyer, J.M. Cuta, FRAPTRAN 1.4: a computer code for the transient analysis of oxide fuel rods, *US Nuclear Regulatory Commission* (NRC) *NUREG/CR-7023-1, 2011*

[A4] Y. Udagawa, Development and release of fuel performance code FEMAXI-8, *Journal of the Atomic Energy Society of Japan vol. 62(10), pp. 555-559, 2020,* https://doi.org/10.3327/jaesjb.62.10_555

[A5] P.A. Jackson, J.A. Turnbull, R.J. White, A Description of the Enigma fuel performance code, in Proc. IAEA Technical Committee Meeting on Water Reactor Fuel Element Computer Modelling in Steady-State, Transient and Accident Conditions, Preston, UK, pp. 28-38, 1988

[A6] G. Rossiter, Development of the ENIGMA fuel performance code for whole core analysis and dry storage assessments, *Nuclear Engineering and Technology vol. 43, pp. 489-498, 2011,* https://doi.org/10.5516/NET.2011.43.6.489

[A7] Y. Rashid, R. Dunham, R. Montgomery, Fuel analysis and licensing code: FALCON MOD01, *EPRI Report 1011308, 2004*

[A8] R.L. Williamson, J.D. Hales, S.R. Novascone, M.R. Tonks, D.R. Gaston, C.J. Permann, D. Andrs, R.C. Martineau, Multi-dimensional multiphysics simulation of nuclear fuel behavior *Journal of Nuclear Materials vol. 432, pp. 149-163, 2012,* https://doi.org/10.1016/j.jnucmat.2012.01.012

[A9] B. Baurens, J. Sercombe, C. Riglet-Martial, L. Desgranges, L. Trotignon, P. Maugis, 3D thermo-chemical–mechanical simulation of power ramps with ALCYONE fuel code, *Journal of Nuclear Materials vol. 452, pp. 578-594, 2014* https://doi.org/10.1016/j.jnucmat.2014.06.021

[A10] V. Marelle et al., New developments in ALCYONE 2.0 fuel performance, *in Top Fuel: LWR Fuels with Enhanced Safety and Performance, 2016*

[A11] C. Introïni, I. Ramière, J. Sercombe, B. Michel, T. Helfer, J. Fauque, ALCYONE: The Fuel Performance Code of the PLEIADES Platform Dedicated to PWR Fuel Rods Behavior, *Annals of Nuclear Energy 207, 110711*, 2024 https://doi.org/10.1016/j.anucene.2024.110711

[A12] A. Soba, A. Denis, DIONISIO 2.0: New version of the code for simulating a whole nuclear fuel rod under extended irradiation, *Nuclear Engineering and Design vol. 292, pp. 213-221, 2015,* https://doi.org/10.1016/j.nucengdes.2015.06.008

[A13] A. Scolaro, I. Clifford, C. Fiorina, A. Pautz, The OFFBEAT multi-dimensional fuel behavior solver, Nuclear Engineering and Design vol. *358, 110416, 2020,* https://doi.org/10.1016/j.nucengdes.2019.110416

[A14] P. Van Uffelen, J. Hales, W. Li, G. Rossiter, R. Williamson, A review of fuel performance modelling, *Journal of Nuclear Materials, vol. 516, pp. 373-412, 2019,* https://doi.org/10.1016/j.jnucmat.2018.12.037

[A15] D. Gaston, C. Newman, G. Hansen, D. Lebrun-Grandié, MOOSE: A parallel computational framework for coupled systems of nonlinear equations, *Nuclear Engineering and Design vol. 239, pp. 1768-1778, 2009* https://doi.org/10.1016/j.nucengdes.2009.05.021

[A16] J.K. Fink, Thermophysical properties of uranium dioxide, *Journal of Nuclear Materials vol. 279, pp. 1-18, 2000* https://doi.org/10.1016/S0022-3115(99)00273-1

[A17] P.G. Lucuta, Hj. Matzke, I.J. Hastings, A pragmatic approach to modelling thermal conductivity of irradiated UO2 fuel: Review and recommendations, *Journal of Nuclear Materials vol. 232, pp. 166-180, 1996* https://doi.org/10.1016/S0022-3115(96)00404-7

[A18] D.L. Hagrman and G. A. Reyman, A Handbook of Materials Properties for Use in the Analysis of Light Water Reactor Fuel Rod Behavior, MATPRO Version 11, *in NUREG/CR-0497 (TREE-1280), US Nuclear Regulatory Commission (NRC), 1979*

[A19] A. Marion, Safety Evaluation by the Office of Nuclear Reactor Regulation of Electric Power Research Institute (EPRI) Topical Report TR-1002865, "Topical Report on Reactivity Initiated Accidents: Bases for RIA Fuel rod Failures and Core Coolability Criteria", *in (NEI) letter dated June 13, 2006 to H. N. Berkow (USNRC/NRR)* http://pbadupws.nrc.gov/docs/ML0616/ML061650107.pdf

[A20] D.T. Hagrman, C.M. Allison, G.A. Berna, SCDAP/RELAP5/MOD 3.1 code manual: MATPRO-A Library of Materials Properties for Light-Water-Reactor Accident Analysis, *in NUREG/CR-6150, EGG-2720, vol. 4, US Nuclear Regulatory Commission (NRC), 1995*

[A21] G. Pastore, L. Luzzi, V. Di Marcello, P. Van Uffelen, Physics-based modelling of fission gas swelling and release in UO2 applied to integral fuel rod analysis **,** *Nuclear Engineering and Design vol. 256, pp. 75-86, 2013* https://doi.org/10.1016/j.nucengdes.2012.12.002

[A22] Y.R. Rashid, Mathematical modeling and analysis of fuel rods, *Nuclear Engineering and Design vol. 29, pp. 22-32, 1974* https://doi.org/10.1016/0029-5493(74)90095-8

[A23] A. Soba, A. Denis, L. Romero, E. Villarino, F. Sardella, A high burnup model developed for the DIONISIO code, *Journal of Nuclear Materials vol. 433, pp. 160-166, 2013* https://doi.org/10.1016/j.jnucmat.2012.08.016

[A24] A. Soba, A. Denis, Simulation with DIONISIO 1.0 of thermal and mechanical pellet-cladding interaction in nuclear fuel rods, *Journal of Nuclear Materials vol. 374, pp. 32-43, 2008* https://doi.org/10.1016/j.jnucmat.2007.06.020

[A25] A.M. Ross & R.L. Stoute, Heat transfer coefficient between UO2 and Zircaloy-2 *Technical Report AECL-1552, Atomic Energy of Canada Limited, 1962*

[A26] M.W. Heinstein and T.A. Laursen, An algorithm for the matrix-free solution of quasistatic frictional contact problems, *Int. J. Numer. Meth. Engng. vol. 44, pp. 1205-1226, 1999* https://doi.org/10.1002/(SICI)1097-0207(19990330)44:9<1205::AID-NME550>3.0.CO;2-0

[A27] K. Forsberg, A.R. Massih, Diffusion theory of fission gas migration in irradiated nuclear fuel UO2, *Journal of Nuclear Materials vol. 135(2-3), pp. 140-148, 1985* https://doi.org/10.1016/0022-3115(85)90071-6

[A28] M. Limbäck & T. Andersson, A Model for Analysis of the Effect of Final Annealing on the In-and Out-of-Reactor Creep Behavior of Zircaloy Cladding, *in ASTM Special Technical Publication, 1295, pp. 448-468, 1996*

[A29] D.G. Franklin, Zircaloy-4 cladding deformation during power reactor irradiation *in ASTM Special Technical Publication, 754, pp. 235-267, 1982*

[A30] D. Plancq, J.M. Ricaud, G. Thouvenin, C. Struzik, T. Helfer, F. Bentejac, P. Thevenin, R. Massen, PLEIADES: A unified environment for multi-dimensional fuel performance modelling, *in Proceedings of the International Meeting on LWR Fuel Performance, 709-714, 2004*

[A31] B. Michel, C. Nonon, J. Sercombe, F. Michel & V. Marelle, Simulation of Pellet-Cladding Interaction with the PLEIADES Fuel Performance Software Environment

[A32] S. Bernaud, I. Ramière, G. Latu, B. Michel, PLEIADES: A Numerical Framework Dedicated to the Multiphysics and Multiscale Nuclear Fuel Behavior Simulation, *Annals of Nuclear Energy 205, 110577,* 2024 https://doi.org/10.1016/j.anucene.2024.110577

[A33] CAST3M, *Available at* http://www-cast3m.cea.fr*, accessed 2 November, 2023.*

[A34] P. Konarski, J. Sercombe, C. Riglet-Martial, L. Noirot, I. Zacharie-Aubrun, K. Hanifi, M. Frégonèse, P. Chantrenne, 3D simulation of a power ramp including fuel thermochemistry and oxygen thermodiffusion, *Journal of Nuclear Materials vol. 519, pp. 104-120, 2019* https://doi.org/10.1016/j.jnucmat.2019.03.021

[A35] D.G. Martin, The thermal expansion of solid UO2 and (U, Pu) mixed oxides — a review and recommendations, *Journal of Nuclear Materials vol. 152, pp. 94-101, 1988* https://doi.org/10.1016/0022-3115(88)90315-7

[A36] Y. Monerie, J-M. Gatt, Overall viscoplastic behavior of non-irradiated porous nuclear ceramics, *Mechanics of Materials vol. 38(7), pp. 608-619, 2006* https://doi.org/10.1016/j.mechmat.2005.11.004

[A37] B. Michel, J. Sercombe, G. Thouvenin, R. Chatelet, 3D fuel cracking modelling in pellet cladding mechanical interaction, *Engineering Fracture Mechanics vol. 75(11), pp. 3581-3598, 2008* https://doi.org/10.1016/j.engfracmech.2006.12.014

[A38] I. Palmer, K. Hesketh, P. Jackson, A model for predicting the radial power profile in a fuel pin, *in IAEA Specialists' Meeting on Water Reactor Fuel Element Performance, 1992*

[A39] K. Lassmann, F. Hohlefeld, The revised URGAP model to describe the gap conductance between fuel and cladding, *Nuclear Engineering and Design vol. 103(2), pp. 215-221, 1987* https://doi.org/10.1016/0029-5493(87)90275-5

[A40] J. Sercombe, I. Aubrun, C. Nonon, Power ramped cladding stresses and strains in 3D simulations with burnup-dependent pellet-clad friction, *Nuclear Engineering and Design vol. 242, pp. 164-181, 2012* https://doi.org/10.1016/j.nucengdes.2011.08.069

[A41] L. Noirot, MARGARET: A comprehensive code for the description of fission gas behavior, *Nuclear Engineering and Design vol. 241, pp. 2099-2118, 2011* https://doi.org/10.1016/j.nucengdes.2011.03.044

[A42] A. Soniak et al., Irradiation creep behavior of Zr-base alloys, *in ASTM Special Technical Publication, 1243, 2002*

[A43] E. Goldberg, M.E. Loza Peralta, A. Soba, DIONISIO 3.0: Comprehensive 3D nuclear fuel simulation through PCMI cohesive and PLENUM models, *Journal of Nuclear Materials vol. 523, pp. 121-134, 2019* https://doi.org/10.1016/j.jnucmat.2019.06.005

[A44] G. Delette and M. Charle, Thermal conductivity of fully dense unirradiated UO2: A new formulation from experimental results between 100°C and 2500°C, and associated fundamental properties *in Water Reactor Fuel Element Modelling at High Burnup and its Experimental Support, IAEA–TECDOC–957, IAEA p. 203, 1997*

[A45] D.R. Olander, Fundamental aspects of nuclear reactor fuel elements, *TID-26711-P1 Technical Information Center, 1976*

[A46] A.C. Marino, E.J. Savino, S. Harriague, BACO (BArra COmbustible) code version 2.20: a thermo-mechanical description of a nuclear fuel rod, *Journal of Nuclear Materials vol. 229, pp. 155-168, 1996* https://doi.org/10.1016/0022-3115(95)00246-4

[A47] R. Radovitzky, A. Seagraves, M. Tupek, L. Noels, A scalable 3D fracture and fragmentation algorithm based on a hybrid, discontinuous Galerkin, cohesive element method, *Computer Methods in Applied Mechanics and Engineering vol. 200, pp. 326-344, 2011* https://doi.org/10.1016/j.cma.2010.08.014

[A48] A. Denis, A. Soba, Simulation of pellet-cladding thermomechanical interaction and fission gas release, *Nuclear Engineering and Design vol. 223, pp. 211-229, 2003* https://doi.org/10.1016/S0029-5493(02)00390-4

[A49] J.K. Fink, L. Leibowitz, Thermal conductivity of zirconium, *Journal of Nuclear Materials vol. 226, pp. 44-50, 1995* https://doi.org/10.1016/0022-3115(95)00110-7

[A50] G. A. Berna et al., FRAPCON-2: A computer code for the calculation of steady state thermal-mechanical behavior of oxide fuel rods, *US Nuclear Regulatory Commission* (NRC) *NUREG/CR-1845, 1980*

[A51] A. Scolaro, Development of a Novel Finite Volume Methodology for Multi-Dimensional Fuel Performance Applications , *PhD Thesis. École Polytechnique Fédérale de Lausanne, 2021* https://doi.org/10.5075/EPFL-THESIS-8822

[A52] D. Pizzocri, T. Barani, L. Luzzi, SCIANTIX: A new open source multi-scale code for fission gas behaviour modelling designed for nuclear fuel performance codes, *Journal of Nuclear Materials vol. 532, 152042, 2020* https://doi.org/10.1016/j.jnucmat.2020.152042

[A53] T. Barani, D. Pizzocri, G. Pastore, L. Luzzi, J.D. Hales, Isotropic softening model for fuel cracking in BISON, *Nuclear Engineering and Design vol. 342, pp. 257-263, 2019* https://doi.org/10.1016/j.nucengdes.2018.12.005

[A54] K.J. Geelhood, W.G. Luscher, P.A. Raynaud, I.E. Porter, FRAPCON-4: A computer code for the calculation of steady state thermal-mechanical behavior of oxide fuel rods for High Burnup, *in PNNL-19418, Vol.1 Rev.2, Pacific Northwest National Laboratory, 2015*

[A55] K. Lassmann, C. O'Carroll, J. van de Laar, C.T. Walker, The radial distribution of plutonium in high burnup UO2 fuels, *Journal of Nuclear Materials vol. 208(3), pp. 223-231, 1994* https://doi.org/10.1016/0022-3115(94)90331-X

[A56] J. Leppänen, M. Pusa, T. Viitanen, V. Valtavirta, T. Kaltiaisenaho, The Serpent Monte Carlo code: Status, development and applications in 2013, *Annals of Nuclear Energy vol. 82, pp. 142-150, 2015* https://doi.org/10.1016/j.anucene.2014.08.024

[A57] P. Cardiff, A. Karač, A. Ivanković, Development of a finite volume contact solver based on the penalty method, *Computational Materials Science vol. 64, pp. 283-284, 2012* https://doi.org/10.1016/j.commatsci.2012.03.011

[A58] INTERNATIONAL ATOMIC ENERGY AGENCY, Thermophysical Properties Database of Materials for Light Water Reactors and Heavy Water Reactors, *in IAEA-TECDOC-1496, IAEA, Vienna, 2006*

[A59] ZryOxidation | BISON https://mooseframework.inl.gov/bison/source/materials/ZryOxidation.html

[A60] F. Garzarolli, W. Jung, H. Shoenfeld, A. M. Garde, G. W. Parray, and P.G. Smerd, Review of PWR fuel rod waterside corrosion behavior, *Technical Report EPRI NP-2789 Project 1250, Kraftwerk Union A.G. and Combustion Engineering Inc., 1982*

[A61] F. Garzarolli, M. Garzarolli, PWR Zr alloy cladding water side corrosion, *Technical Report, ANT Inte rnational, 2012*

[A62] P.M. Gilmore, H.H. Klepfer, J.M. Sorensen, EPRI PWR Fuel Cladding Corrosion (PFCC) Model Volume 1: Theory and User's Manual, *in EPRI Report, TR-105387-V1, 1995*

[A63] S. Leistikow, G. Schanz, H. vBerg, Kinetik Und Morphologic der isothermen Dampf-Oxidation von Zircaloy-4 bei 700-1300°C, *Kernforschungszentrum Karlsruhe, KFK 2587, March 1978*

[A64] G. Schanz, Recommendations and supporting information on the choice of zirconium oxidation models in severe accident codes, *Technical Report FZKA 6827, SAM-COLOSS-P043, Institut für Materialforschung, 2003*

[A65] J. T. Prater and E. L. Courtright, Zircaloy-4 oxidation at 1300 to 2400°C, *Technical Report NUREG/CR-4889, PNL-6166, 1987*

[A66] J.V. Cathcart, Quarterly Progress Report on the Zirconium Metal-Water Oxidation Kinetics Program, *in ORNL/NUREG/TM-41, 1976*

[A67] A. Scolaro, E. Brunetto and C. Fiorina, Modeling of Zircaloy Oxidation Through Dynamic Mesh Deformation, *in M&C 2023, Niagara Falls, Ontario, Canada, 2023*

[A68] A. Couet, A.T. Motta, R.J. Comstock, Hydrogen pickup measurements in zirconium alloys: Relation to oxidation kinetics, *Journal of Nuclear Materials vol. 451, pp. 1-13, 2014* https://doi.org/10.1016/j.jnucmat.2014.03.001

[A69] C. Cozzo, G. Khvostov, I. Clifford, H. Ferroukhi, Appraisal of the NRC H-uptake calculation for Swiss boiling water reactors, *Nuclear Engineering and Design vol. 391, 111731, 2022* https://doi.org/10.1016/j.nucengdes.2022.111731

[A70] K. Geelhood and C. Beyer, Hydrogen Pickup Models for Zircaloy-2, Zircaloy-4, M5 and ZIRLO, *in Water Reactor Fuel Performance Meeting, Chengdu, China, 2011*

[A71] P. Clifford, ACCEPTABLE FUEL CLADDING HYDROGEN UPTAKE MODELS, *NRC Memorandum, ML15133A306, 2015*

[A72] A.T. Motta et al., Hydrogen in zirconium alloys: A review, *Journal of Nuclear Materials vol. 518, pp. 440-460, 2019* https://doi.org/10.1016/j.jnucmat.2019.02.042

[A73] O. Courty, A.T. Motta, J.D. Hales, Modeling and simulation of hydrogen behavior in Zircaloy-4 fuel cladding, *Journal of Nuclear Materials vol. 452, pp. 311-320, 2014* https://doi.org/10.1016/j.jnucmat.2014.05.013

[A74] D.S. Stafford, Multidimensional simulations of hydrides during fuel rod lifecycle, *Journal of Nuclear Materials vol. 466, pp. 362-372, 2015* https://doi.org/10.1016/j.jnucmat.2015.06.037

[A75] P. Clifford, Pressurized-water reactor control rod ejection and boiling-water reactor control rod drop accidents, *Technical Report Regulatory Guide RG 1.236, US NRC, 2020*

[A76] K. L. Nissen, W. Goll, V. I. Arimescu, G. Ledergerber, and C. Hellwig, Hydrogen uptake of BWR fuel rods. Power history effects at long irradiation times, *in* Proceedings of the Water Reactor Fuel Performance Meeting (WRFPM), Tokyo, Japan*. Framatome, 9 2014*

[A77] F. Passelaigue, E. Lacroix, G. Pastore, A.T. Motta, Implementation and Validation of the Hydride Nucleation-Growth-Dissolution (HNGD) model in BISON, *Journal of Nuclear Materials vol. 544, 152683, 2021* https://doi.org/10.1016/j.jnucmat.2020.152683

[A78] P. Konarski, HYPE: Hydrogen Postprocessor for Falcon – code description and user manual, *PSI Technical Report TM-41-21-29 V.0 (SB-RND-ACT-009-19-012), 2021*

[A79] J. Desquines, D. Drouan, M. Billone, M.P. Puls, P. March, S. Fourgeaud, C. Getrey, V. Elbaz, M. Philippe, Influence of temperature and hydrogen content on stress-induced radial hydride precipitation in Zircaloy-4 cladding, *Journal of Nuclear Materials vol. 453, pp. 131-150, 2014* https://doi.org/10.1016/j.jnucmat.2014.06.049

[A80] M.S. Veshchunov, V.E. Shestak, V.D. Ozrin, A new model of hydrogen redistribution in Zr alloy claddings during waterside corrosion in a temperature gradient, *Journal of Nuclear Materials vol. 472, pp. 65-75, 2016* https://doi.org/10.1016/j.jnucmat.2016.01.032

[A81] A. Sawatzky, The diffusion and solubility of hydrogen in the alpha phase of zircaloy-2 *Journal of Nuclear Materials vol. 2, pp. 62-68, 1960* https://doi.org/10.1016/0022-3115(60)90025-8

[A82] J.J Kearns, Diffusion coefficient of hydrogen in alpha zirconium, Zircaloy-2 and Zircaloy-4, *Journal of Nuclear Materials vol. 43, pp. 330-338, 1972* https://doi.org/10.1016/0022-3115(72)90065-7

[A83] W. Gong, P. Trtik, A.W. Colldeweih, L.I. Duarte, M. Grosse, E. Lehmann, J. Bertsch, Hydrogen diffusion and precipitation in duplex zirconium nuclear fuel cladding quantified by high-resolution neutron imaging, *Journal of Nuclear Materials vol. 526, 151757, 2019* https://doi.org/10.1016/j.jnucmat.2019.151757

[A84] F. Fagnoni, P. Trtik, J.M. Wheeler, R. Zubler, J. Bertsch, L.I. Duarte, Hydrogen diffusion in zirconium cladding alloys with an inner liner as quantified by neutron radiography and nanoindentation, *Journal of Nuclear Materials vol. 584, 154574, 2023* https://doi.org/10.1016/j.jnucmat.2023.154574

[A85] P. Konarski, C. Cozzo, G. Khvostov, H. Ferroukhi, Modeling of hydrogen behavior in liner claddings *Journal of Nuclear Materials vol. 573, 154125, 2023* https://doi.org/10.1016/j.jnucmat.2022.154125

[A86] Ž. Tuković, A. Ivanković, A. Karač, Finite-volume stress analysis in multi-material linear elastic body, *Int. J. Numer. Meth. Engng vol. 93, 400-419, 2013* https://doi.org/10.1002/nme.4390

[A87] G. Khvostov, Post-test Analysis of the IFA-650.12 Halden LOCA Experiment using the FALCON Code coupled to FRELAX Model, *PSI Technical Report TM-41-13-04 V.0 (SB-RND-ACT-008-10.005), 2013*

[A88] V. D’Ambrosi et al., P2M Simulation Exercise on Past Fuel Melting Irradiation Experiments, N*uclear Technology, 2023* https://doi.org/10.1080/00295450.2023.2194270

[A89] G. Khvostov, K. Mikityuk, M.A. Zimmermann, A model for fission gas release and gaseous swelling of the uranium dioxide fuel coupled with the FALCON code, *Nuclear Engineering and Design vol. 241, pp. 2983-3007, 2011* https://doi.org/10.1016/j.nucengdes.2011.06.020